Cambrian High-temperature Reworking of the Rayner–Eastern Ghats Terrane: Constraints from the Northern Prince Charles Mountains Region, East Antarctica

Laura J. Morrissey[1],*, **Martin Hand**[1], **David E. Kelsey**[1] and **Benjamin P. Wade**[2]

[1]Department of Earth Sciences, School of Physical Sciences, University of Adelaide, Adelaide, SA 5005, Australia and [2]Adelaide Microscopy, University of Adelaide, Adelaide, SA 5005, Australia

*Corresponding author. Telephone: +61418851623. E-mail: laura.morrissey@adelaide.edu.au

ABSTRACT

Metapelitic rocks from the northern Prince Charles Mountains–East Amery Ice Shelf region of the Rayner Complex, East Antarctica, record high-temperature reworking during Cambrian times. Calculated metamorphic phase diagrams for rocks with varying chemical compositions and mineral assemblages suggest that peak temperatures were 800–870°C at pressures of 5·5–6·5 kbar. However, Cambrian-age high-*T* reworking is patchy and is recorded only in some locations, with other areas recording pristine early Mesoproterozoic–Neoproterozoic assemblages formed during the *c.* 1000–900 Ma Rayner Orogeny. The spatial distribution of reworking may indicate that the comparatively anhydrous residual rock compositions inherited from the Rayner Orogeny were relatively inert to reworking during the Cambrian. Domains that record Cambrian reworking conceivably underwent hydrous retrogression at the end of the Rayner Orogeny and were therefore comparatively reactive during reheating in the Cambrian. High-*T* reworking during the Cambrian has previously been recognized in the Prydz Bay region at the margin of the Rayner Complex, but not in the northern Prince Charles Mountains. The Eastern Ghats Province in India, which was formerly contiguous with the Rayner Complex, preserves a similarly enigmatic record of Cambrian geochronology, suggesting that the Rayner–Eastern Ghats terrane as a whole may have experienced selective reworking during the Cambrian. The geodynamic setting for the formation of this thermal regime is not well understood, but the attainment of high crustal temperatures may have been facilitated by a reduced capacity for thermal buffering, arising from limited partial melting within a previously dehydrated crustal column.

Key words: Gondwana; HTLP metamorphism; monazite geochronology; Rayner Complex; THERMOCALC

INTRODUCTION

Inferring the tectono-metamorphic history of a terrane relies on a detailed combined geochronological and metamorphic petrology approach to decipher the pressure–temperature (*P–T*) evolution. However, the interpretation of the geological history of a terrane may be complicated by polymetamorphism. The application of more precise geochronological methods, and the increasing use of *in situ* geochronology, has allowed for a better understanding of the development of reaction textures, including recognizing when rocks record the effects of multiple, temporally unrelated events (e.g. Hand *et al.*, 1992; Hensen & Zhou, 1995*b*; Goncalves *et al.*, 2004; Dutch *et al.*, 2005; Kelsey *et al.*, 2007; Korhonen *et al.*, 2012; Yakymchuk *et al.*, 2015). However, deciphering metamorphic events can be

difficult in terranes that have undergone extensive metamorphism and melt loss. These terranes have reduced potential for further melting during subsequent metamorphic events, and, as a result, subsequent events may occur at subsolidus conditions, even if they involve high temperatures (e.g. Vielzeuf *et al.*, 1990; White & Powell, 2002; Diener *et al.*, 2008; Clark *et al.*, 2011; Korhonen *et al.*, 2012). The paucity or lack of a fluid phase creates unreactive rock compositions, which are less likely to record evidence of further events, either by the formation of new mineral assemblages or by the resetting of geochronometers (e.g. White & Powell, 2002; Tenczer *et al.*, 2006; Phillips *et al.*, 2007*a*, 2009; Korhonen *et al.*, 2012). Additionally, terranes that have previously undergone partial melting are susceptible to high-*T* thermal reworking because they largely avoid the energetic requirements for melting (e.g. Vielzeuf *et al.*, 1990; Stüwe, 1995; Brown & Korhonen, 2009; Clark *et al.*, 2011; Morrissey *et al.*, 2014; Walsh *et al.*, 2015). One way of recognizing polymetamorphism in residual terranes is to investigate carefully the preserved petrographic relationships throughout a region. For example, terranes that appear to preserve substantially different *P–T* paths for spatially adjacent areas are candidates for cryptically preserved polymetamorphism.

The Rayner Complex in East Antarctica forms part of a vast terrane that includes the Eastern Ghats Province in India (Fig. 1). It underwent high-temperature metamorphism and extensive melting during the *c.* 1000–900 Ma Rayner Orogeny (e.g. Kinny *et al.*, 1997; Zhao *et al.*, 1997; Boger *et al.*, 2000; Carson *et al.*, 2000; Boger & White, 2003; Halpin *et al.*, 2007*a*; Morrissey *et al.*, 2015). This event has previously been characterized as recording anticlockwise *P–T* paths that are dominated by cooling (Fitzsimons & Harley, 1992; Thost & Hensen, 1992; Boger & White, 2003; Halpin *et al.*, 2007*a*). However, some locations preserve mineral reaction microstructures that are more commonly interpreted to reflect clockwise *P–T* paths, particularly at locations that are characterized by the formation of secondary cordierite-bearing mineral assemblages (Nichols & Berry, 1991; Stüwe & Hand, 1992; Hand *et al.*, 1994*a*; Nichols, 1995; Halpin *et al.*, 2007*b*; Corvino *et al.*, 2011). The clockwise *P–T* evolution in Kemp Land on the margin of the Rayner Complex (Fig. 1) has been interpreted to reflect differences in strain partitioning and magma flux between the older Archean Napier Complex and more juvenile Proterozoic Rayner Complex (Halpin *et al.*, 2007*b*). However, in the central Rayner Complex, the significance of these apparent clockwise *P–T* paths remains unclear.

In this study we investigate seven locations from the ostensibly early Neoproterozoic northern Prince Charles Mountains (nPCM)–East Amery Ice Shelf (EAIS) region of the Rayner Complex in East Antarctica (Table 1; Fig. 1d). Samples from these locations contain secondary cordierite-bearing assemblages that appear inconsistent with the isobaric cooling paths inferred

elsewhere in the Rayner Complex (e.g. Fitzsimons & Harley, 1992; Fitzsimons & Thost, 1992; Boger & White, 2003; Halpin *et al.*, 2007*a*). Calculated metamorphic phase diagrams are combined with *in situ* geochronology to constrain the timing of the cordierite-bearing mineral assemblages.

We find that the secondary cordierite-bearing mineral assemblages are Cambrian in age and that the textural metamorphic response of the Rayner Complex during the Cambrian is patchy. We suggest that high-*T* Cambrian mineral assemblages formed only in regions that were retrogressed at the end of the Rayner Orogeny. The bulk of the Rayner Complex does not record high-*T* Cambrian reworking owing to its relatively anhydrous and thus inert rock compositions.

GEOLOGICAL FRAMEWORK

Much of the Antarctic basement is poorly outcropping; however, the Prince Charles Mountains (PCM) in East Antarctica provide a 600 km cross-section extending inland from the Mawson Coast in MacRobertson Land (Fig. 1c). The PCM have been divided into four distinct geological terranes (e.g. Tingey, 1991; Mikhalsky *et al.*, 2001*b*, 2006*b*; Phillips *et al.*, 2006; Boger *et al.*, 2008). The southern Prince Charles Mountains (sPCM) are composed of the Ruker Complex, which has an Archean history, and the Lambert Complex, which has an Archean–Paeloproterozoic history and makes up much of the Mawson Escarpment (Fig. 1c; Mikhalsky *et al.*, 2001*b*, 2006*a*; Phillips *et al.*, 2006; Boger *et al.*, 2008; Corvino *et al.*, 2008). The Fisher Complex is located between the sPCM and the northern Prince Charles Mountains (nPCM) and is composed of 1300–1200 Ma calc-alkaline volcanic rocks that have been metamorphosed to amphibolite facies, with late granitoids emplaced at 1050–1020 Ma (Fig. 1c; Beliatsky *et al.*, 1994; Mikhalsky *et al.*, 1996, 2001*b*; Kinny *et al.*, 1997). The nPCM form part of the Proterozoic Rayner Complex and are the focus of this study. The Rayner Complex was defined to separate crust with a Proterozoic tectonic history from blocks that record an Archean history (Kamenev, 1972), and is interpreted to extend inland from the coastline of Kemp and MacRobertson Lands to the Fisher Complex and sPCM, and from Enderby Land in the west to Princess Elizabeth Land, east of the Amery Ice Shelf (Fig. 1; e.g. Tingey, 1991; Boger, 2011). The rocks in the East Amery Ice Shelf (EAIS) and Prydz Bay regions are now interpreted to have a similar history to those in the nPCM, but preserve evidence for pervasive high-grade reworking during the Cambrian (Hensen & Zhou, 1995*a*, 1995*b*; Kelsey *et al.*, 2007; Wang *et al.*, 2008; Liu *et al.*, 2009*b*, 2014; Grew *et al.*, 2012). The Rayner Complex is generally considered to have been contiguous with the Eastern Ghats Province in India (Fig. 1; Mezger & Cosca, 1999; Fitzsimons, 2000; Boger, 2011), and therefore its tectonic evolution should logically be considered in the same context.
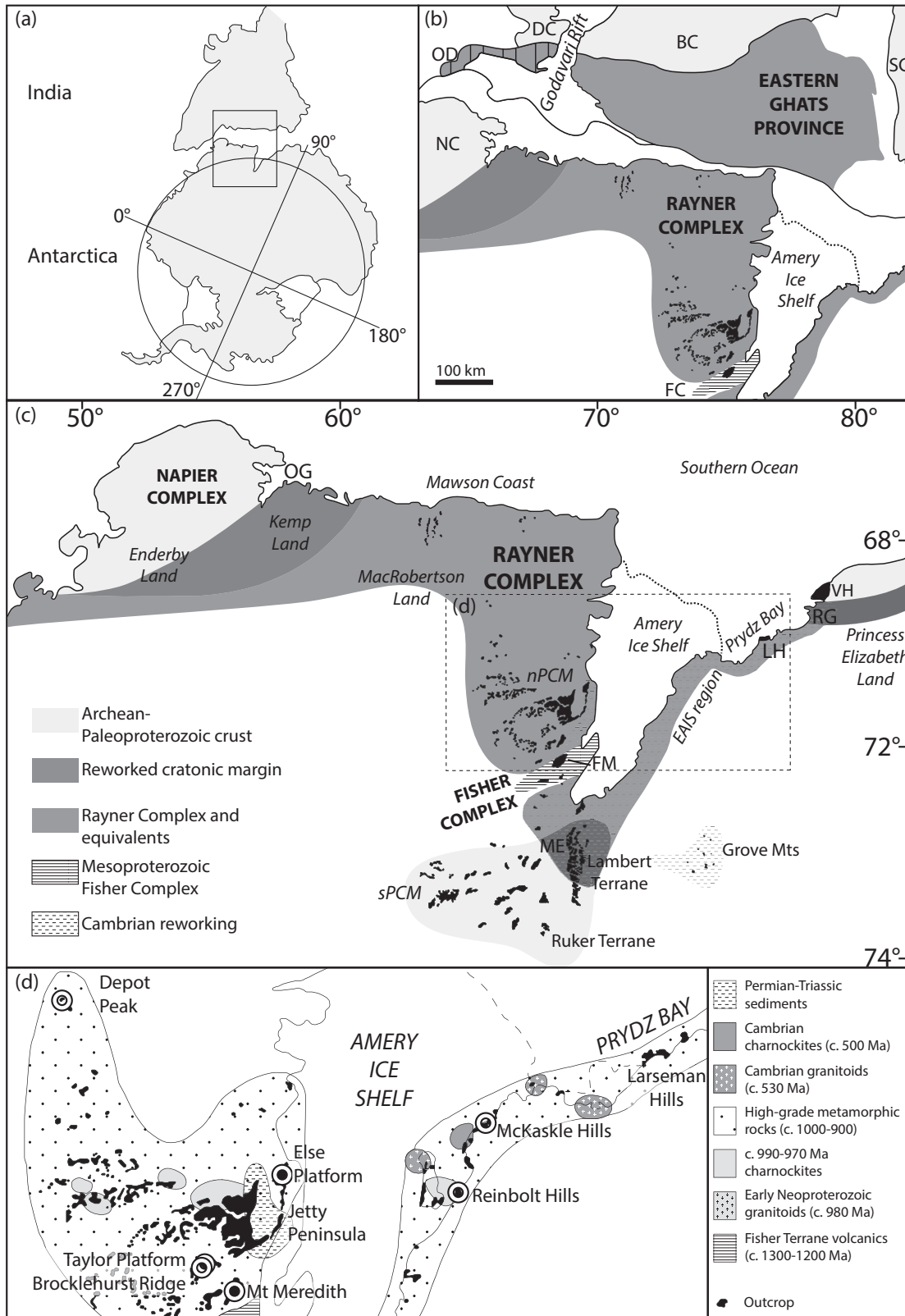
Fig. 1. (a, b) Schematic reconstruction of India and Antarctica, showing the Rayner Complex and Eastern Ghats Province in context of the present-day continents. OD, Ongole Domain; DC, Dharwar Craton; BC, Bastar Craton; SC, Singhbhum Craton; NC, Napier Complex; FC, Fisher Complex. (c) Simplified geological map showing the Rayner Complex and Prince Charles Mountains (PCM) in the context of the surrounding terranes, after Phillips *et al.* (2009). The Rayner Complex extends east from Enderby Land to Princess Elizabeth Land, and south from the Mawson and Kemp Land coasts. OG, Oygarden Group; FM, Fisher Massif; ME, Mawson Escarpment; LH, Larsemann Hills; RG, Rauer Group; VH, Vestfold Hills; EAIS, East Amery Ice Shelf. (d) Outcrop map of the northern Prince Charles Mountains showing sample locations, after Mikhalsky *et al.* (2001*b*) and Liu *et al.* (2009*b*).

Table 1: Sample locations and sample summary

Sample	Location		Easting	Northing	Description	Age
Northern Prince Charles Mountains (nPCM)						
DP-1	Depot Peak	41D	563934	2340118	Pegmatite within shear zone	Cambrian
DP-11	Depot Peak	41D	563934	2340118	Late pegmatite	Cambrian
DP-7	Depot Peak	41D	563934	2340118	Gt–sill gneiss with cd–sp–ilm coronas	Bimodal: *c.* 930 Ma and Cambrian
PCM-83	Else Platform	42D	491213	2188537	Gt–sill gneiss with cd–sp–ilm coronas	Bimodal: *c.* 930 Ma and Cambrian
77090	Taylor Platform	42D	433206	2120313	Gt–cd gneiss	Dominantly Cambrian
77102B	Brocklehurst Ridge	42D	431390	2118426	Gt–cd–sill–bi gneiss	Dominantly Cambrian
77079	Mt Meredith	42D	455042	2099832	Gt–bi–qz granofels	Cambrian
East Amery Ice Shelf (EAIS)						
72046A	Reinbolt Hills	43D	406808	2178312	Gt–sill gneiss with cd–sp–ilm coronas	Bimodal: *c.* 930 Ma and Cambrian
77223	McKaskle Hills	43D	423647	2232948	Gt gneiss with cd–qz and pl–qz coronas	Dominantly Cambrian

The Rayner Complex was deformed and metamorphosed during the Rayner Orogeny (Table 2; Kinny *et al.*, 1997; Boger *et al.*, 2000; Kelly *et al.*, 2002; Kelly & Harley, 2004; Halpin *et al.*, 2007*a*, 2007*b*, 2013; Morrissey *et al.*, 2015). The effects of the Rayner Orogeny are widespread and involved reworking of the cratonic margin of the Napier Complex (Halpin *et al.*, 2007*b*), as well as the Rayner Complex in the northern nPCM, Mawson Coast and EAIS regions (Fig. 1; Boger *et al.*, 2000; Halpin *et al.*, 2007*a*; Grew *et al.*, 2012; Liu *et al.*, 2014; Morrissey *et al.*, 2015). This event was accompanied by voluminous charnockitic and granitic magmatism between 990 and 900 Ma that dominates much of the outcropping Rayner Complex (Tingey, 1991; Manton *et al.*, 1992; Munksgaard *et al.*, 1992; Kinny *et al.*, 1997; Zhao *et al.*, 1997; Carson *et al.*, 2000). However, an earlier, higher-*P* phase of metamorphism at *c.* 1020 Ma has also been recognized in the nPCM (Morrissey *et al.*, 2015), and was accompanied by magmatism in the southern EAIS and Fisher Complex (Kinny *et al.*, 1997; Liu *et al.*, 2009*b*, 2014). Detailed geochronology studies of the Mawson Charnockite along the Mawson Coast indicate that episodic magmatism occurred from *c.* 1150 to 950 Ma, suggesting that the thermal regime associated with the Rayner Orogeny may have commenced as early as *c.* 1150 Ma and proceeded either continuously or as a punctuated thermal system for *c.* 250 Myr (Halpin *et al.*, 2012).

Contrasting *P–T* paths have been proposed for the Rayner Complex during the Rayner Orogeny (Table 2). Metamorphism at 990–970 Ma recorded in rocks along the Mawson Coast appears to be high thermal gradient in character, with an anticlockwise *P–T* evolution reaching peak temperatures of 850–900°C at 5·5–6 kbar, followed by crustal thickening to pressures of 6–7 kbar, synchronous with repeated pluton emplacement (Halpin *et al.*, 2007*a*). Conversely, further west in Kemp Land (Fig. 1), younger *c.* 930 Ma metamorphism occurred at similar temperatures of 850–990°C, but at higher pressures of 9–10 kbar, and involved a clockwise *P–T* evolution (Kelly & Harley, 2004; Halpin *et al.*, 2007*b*), interpreted to reflect reworking of a stronger cratonic margin. In the nPCM, the Rayner Orogeny has been interpreted to have involved an anticlockwise *P–T* evolution with peak conditions related to the emplacement of granitic and charnockitic magmas and reaching 800–850°C and 6–7 kbar, followed by isobaric cooling (Fitzsimons & Harley, 1992; Fitzsimons & Thost, 1992; Nichols, 1995; Stephenson & Cook, 1997; Boger & White, 2003; Morrissey *et al.*, 2015). However, it has also been suggested that some locations in the nPCM and EAIS region experienced clockwise *P–T* histories. A sample from Mt Lanyon, located in the southern nPCM, was interpreted to record decompression from a rutile-bearing assemblage to a cordierite-bearing assemblage (Nichols, 1995). However, recent *in situ* geochronology suggests that this apparent clockwise *P–T* path may be the result of the superimposition of an earlier, higher-*P* event at *c.* 1020 Ma and a younger, lower-*P* event at *c.* 930 Ma (Morrissey *et al.*, 2015). Similarly, samples from Depot Peak, Else Platform and the Reinbolt Hills show garnet–sillimanite assemblages that have been partially replaced by cordierite–spinel symplectites, interpreted to reflect decompression (Nichols & Berry, 1991; Stüwe & Hand, 1992; Hand *et al.*, 1994*b*; Scrimgeour & Hand, 1997). However, none of these studies were combined with geochronology, and therefore the possibility that the apparent decompressional *P–T* paths also reflect two unrelated events cannot be excluded (e.g. Hand *et al.*, 1994*a*). Metamorphism associated with shortening at 960–905 Ma is also recorded in the northern Mawson Escarpment (Fig. 1c), and reached peak conditions of 6·5–7·1 kbar and 790–810°C (Phillips *et al.*, 2009; Corvino *et al.*, 2011). Thus, the Rayner Orogeny involved high-grade metamorphism with temperatures in excess of 850°C. It resulted in voluminous melting and magmatism, creating a dehydrated, residual granulite-facies terrane.

Table 2: Summary of the metamorphic conditions in the nPCM–EAIS region

Location	Age	Peak conditions	P–T path	References
Mawson Coast, MacRobertson Land	Rayner Event; 990–970 Ma	850–900°C; 5·5–6 kbar	Anticlockwise–isobaric cooling	Halpin *et al.*, 2007*a*
Mawson Coast, Kemp Land	Rayner Event; *c.* 930 Ma	850–990°C; 9–10 kbar	Decompression	Halpin *et al.*, 2007*b*
nPCM, Radok Lake	Rayner Event; 940–910 Ma	880°C; 6·0–6·5 kbar	Anticlockwise–isobaric cooling	Boger & White, 2003; Morrissey *et al.*, 2015
nPCM, Else Platform	Rayner Event; 2 events?	800°C; 6·5–7 kbar	Cooling, then decompression and reheating to 700°C	Hand *et al.*, 1994*a, b*
nPCM, Depot Peak	Rayner Event; 2 events?	700°C; 5·6 kbar	Minor decompression and cooling	Stüwe & Hand, 1992
Mawson Escarpment	Rayner Event; 2 events?	790–810°C; 6·5–7·1 kbar	Possible decompression?	Phillips *et al.*, 2009; Corvino *et al.*, 2011
EAIS, McKaskle Hills	Cambrian; *c.* 530 Ma	880–950°C; 9–9·5 kbar	Decompression and cooling	Liu *et al.*, 2007*b*
Prydz Bay, Rauer Group	Cambrian	950–975°C; 10–10·6 kbar	Decompression	Kelsey *et al.*, 2003*c*
Prydz Bay, Brattstrand Bluffs	Cambrian	860°C; 6 kbar	Decompression	Fitzsimons, 1996
Prydz Bay, Larsemann Hills	Cambrian	800°C, 7 kbar	Decompression	Carson *et al.*, 1997
Grove Mountains	Cambrian	770–840°C; 11·8–14·0 kbar	Isothermal decompression	Liu *et al.*, 2009*a*

Cambrian reworking in the Rayner Complex

The architecture of the East Antarctic shield is now considered to have been the result of juxtaposition of different crustal blocks during Cambrian orogenesis, associated with the formation of Gondwana (e.g. Fitzsimons, 2000; Meert, 2003; Boger, 2011). Parts of the Rayner Complex were reworked during the Cambrian (Table 2; Hensen & Zhou, 1995*a*; Fitzsimons, 1996; Carson *et al.*, 1997; Fitzsimons *et al.*, 1997; Boger *et al.*, 2002; Kelsey *et al.*, 2003*a*, 2007, 2008*b*; Zhao *et al.*, 2003; Wang *et al.*, 2008; Liu *et al.*, 2009*a*, 2009*b*). The effects of this event are most evident in the Prydz Bay region (Fig. 1c). In the Rauer Group, rocks reached UHT conditions of 950–975°C and 10–10·6 kbar, followed by decompression (Fig. 1c; Table 2; Harley, 1998; Kelsey *et al.*, 2003*c*, 2007; Tong & Wilson, 2006). Peak conditions of 800–860°C and 6–7 kbar, followed by decompression, are recorded in the Brattstrand Bluffs and Larsemann Hills (Table 2; Fitzsimons & Harley, 1991, 1992; Carson *et al.*, 1995, 1997; Fitzsimons, 1996). The event was accompanied by extensive anatexis (Carson *et al.*, 1996; Fitzsimons *et al.*, 1997; Zhao *et al.*, 2003) and deformation (Dirks & Hand, 1995; Dirks & Wilson, 1995; Wilson *et al.*, 2007).

In the EAIS (Fig. 1c), peak metamorphism is interpreted to have occurred at *c.* 535 Ma (Liu *et al.*, 2009*b*). Conventional thermobarometry for mafic granulites in the McKaskle Hills (Fig. 1d) indicates peak conditions of 880–950°C at 9–9·5 kbar, followed by decompression and cooling to conditions of 700–750°C and 6·6–7·2 kbar (Liu *et al.*, 2007*b*). Intrusion of the Jennings Charnockite also occurred at *c.* 500 Ma (Liu *et al.*, 2009*b*). However, evidence for Cambrian reworking in the EAIS is variable and seems to be restricted to discrete locations. Zircon geochronology for the Reinbolt Hills (Fig. 1d) appears to indicate metamorphism at *c.* 930 Ma, with very little evidence of a Cambrian overprint (Liu *et al.*, 2009*b*). However, U–Th–Pb monazite geochronology from a sillimanite-bearing pegmatite from the Reinbolt Hills gives a mean age of 534 ± 17 Ma, interpreted to represent new growth of monazite at granulite-facies conditions, or anatexis of metasedimentary protoliths (Ziemann *et al.*, 2005).

Further south, the Grove Mountains (Fig. 1c) record an extensive and pervasive Cambrian history (Liu *et al.*, 2007*a*, 2009*a*). Peak pressures for erratic boulders of mafic granulite have been constrained to 11·8–14·0 kbar and 770–840°C at *c.* 545 Ma, before near-isothermal decompression to ~6 kbar at *c.* 530 Ma (Liu *et al.*, 2009*a*). Charnockitic and granitic magmatism occurred at 550–500 Ma (Mikhalsky *et al.*, 2001*a*; Zhao *et al.*, 2003; Liu *et al.*, 2006). It is unclear whether the Grove Mountains form part of the Rayner Complex or are a separate terrane (Mikhalsky *et al.*, 2001*a*; Liu *et al.*, 2009*a*), but the high-pressure metamorphism has been interpreted as evidence for a collisional setting during the formation of Gondwana (Liu *et al.*, 2009*a*).

In the sPCM, both the Ruker and Lambert Complexes (Fig. 1c) preserve evidence of Cambrian reworking at *c.* 530–490 Ma (Boger *et al.*, 2001; Boger & Wilson, 2005; Corvino *et al.*, 2008, 2011; Phillips *et al.*, 2009). In the southern Lambert Complex, Cambrian deformation is pervasive and metamorphism involved a clockwise *P–T* path from peak conditions of 650–700°C and 6–7 kbar, followed by 3 kbar of isothermal decompression (Boger & Wilson, 2005). In the northern Lambert Complex, granitic and pegmatite intrusive rocks are recorded at *c.* 510–490 Ma, and replacement of sillimanite by a lower-*P* cordierite-bearing assemblage has also been interpreted to relate to Cambrian reworking (Corvino *et al.*, 2008, 2011; Phillips *et al.*, 2009). However, unlike the southern Lambert Complex, deformation is restricted to discrete shear zones, and some samples contain Cambrian monazite but no evidence of Cambrian zircon (Corvino *et al.*, 2008, 2011; Phillips *et al.*, 2009). In the Ruker Complex, Cambrian deformation occurred along high-strain zones and involved metamorphic conditions of 565–640°C and 4–5·2 kbar (Phillips *et al.*, 2007*a*).

In the nPCM, Cambrian reworking has been thought to be of minor importance. Isotopic systems such as Rb–Sr were reset at *c.* 500 Ma (Tingey, 1991; Manton *et al.*, 1992), and garnet Sm–Nd geochronology gives a range of ages from 825 to 555 Ma, suggesting thermal reworking post-900 Ma (Zhou & Hensen, 1995; Hensen *et al.*, 1997). However, in many cases zircon geochronology from intrusive rocks is dominated by older ages (*c.* 1000–900 Ma), with most samples showing evidence of only minor resetting and no *c.* 500 Ma zircon growth (Manton *et al.*, 1992; Kinny *et al.*, 1997). Emplacement of biotite granite and pegmatite occurred at *c.* 550–500 Ma on Jetty Peninsula, Mt Kirkby and Else Platform (Manton *et al.*, 1992; Carson *et al.*, 2000; Boger *et al.*, 2002), and at Else Platform *c.* 500 Ma felsic dykes have been migmatized (Hand *et al.*, 1994*b*; Scrimgeour & Hand, 1997). Together, these indicate some amount of melting and high-temperature reworking during the Cambrian (Manton *et al.*, 1992; Hand *et al.*, 1994*b*; Scrimgeour & Hand, 1997). However, overall, Cambrian-age reworking in the nPCM has been interpreted to be restricted to discrete NE-trending mylonitic zones that commonly occur on the margins of *c.* 550–520 Ma pegmatites (Carson *et al.*, 2000; Boger *et al.*, 2002). These mylonites have not been directly dated, but have been interpreted to post-date *c.* 550–520 Ma pegmatites and predate Rb–Sr biotite ages of *c.* 475 Ma (Boger *et al.*, 2002). They record contractional kinematics, with SE over NW thrust movement (Boger *et al.*, 2002), and have been interpreted to have formed at *P–T* conditions of 524 ± 20°C and 7·6 ± 4 kbar (Boger *et al.*, 2002). They are thought to be similar to undated mylonites in the Reinbolt Hills in the EAIS and from the Mawson Coast (Clarke, 1988; Nichols, 1995).

PETROGRAPHY AND SAMPLE DESCRIPTION

The samples used in this study are a combination of legacy samples collected over several field seasons in the late 1980s and early 1990s. Numbered samples are

Table 3: Petrography of pelitic samples

Sample	M$_1$ assemblage *c.* 930 Ma	M$_2$ assemblage *c.* 530 Ma
Northern Prince Charles Mountains (nPCM)		
DP-7	gt + sill + bi + ksp + sp$_1$ + ilm$_1$ + qz$_1$	cd + sp$_2$ + ilm$_2$ + pl + qz$_2$ (+ gt + sill + ksp)
PCM-83	gt + sill + bi + ksp + sp$_1$ + ilm$_1$ + qz	cd + sp$_2$ + ilm$_2$ (+ gt + sill)
77090	—	gt + sill + cd + bi + ilm + qz
77102B	—	gt + sill + cd + bi + ksp + ilm + pl + qz
77079	—	gt + bi + pl + ilm + qz
East Amery Ice Shelf (EAIS)		
72046A	gt + sill + bi + sp$_1$ + ilm$_1$ + qz	cd + sp$_2$ + ilm$_2$ + ksp + pl (+ gt + sill)
77223	gt + sill + bi$_1$ + ksp$_1$ + ilm$_1$ + ru + pl$_1$ + qz$_1$	cd + bi$_2$ + ksp$_2$ + ilm$_2$ + pl$_2$ + qz$_2$ (+ gt)
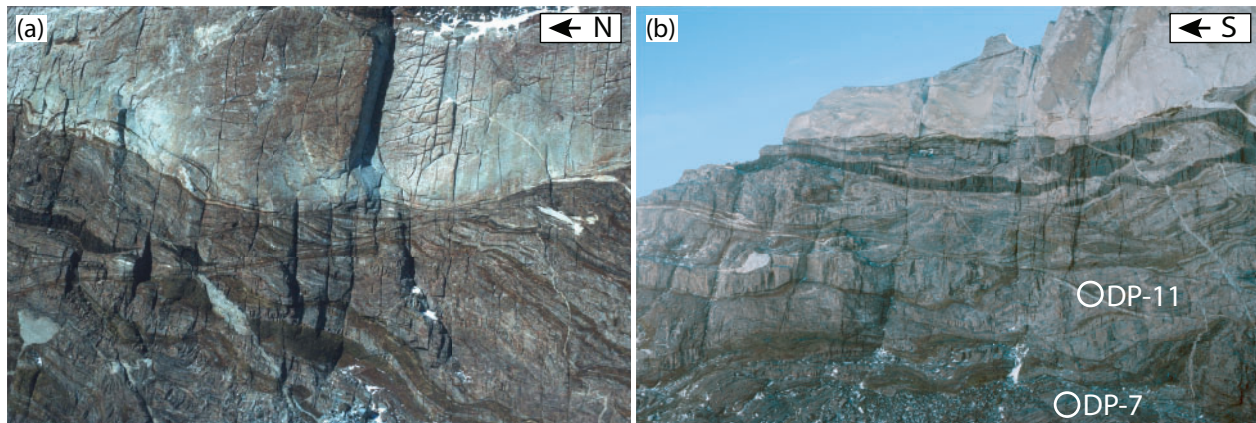
Fig. 2. Outcrop photographs of the Depot Peak sample locality. The sampling locations for DP-11 and DP-7 are shown in (b). The sampling location for DP-1 is not shown in these images.

from the rock library at the University of Tasmania; the samples beginning with letters are from collections at the University of Adelaide. The samples chosen for this study are from locations throughout the nPCM–EAIS region (Fig. 1d). The often large gaps between outcrops in the nPCM mean that it is difficult to draw structural links between samples (e.g. Fitzsimons & Thost, 1992). Most samples in this study preserve evidence for growth of post-peak cordierite or are biotite-rich metapelites; these contrast metamorphically with the assemblages that preserve evidence for Early Neoproterozoic isobaric cooling observed elsewhere in the nPCM (e.g. Fitzsimons & Harley, 1992; Fitzsimons & Thost, 1992; Nichols, 1995; Boger & White, 2003). A pegmatite from within a granulite-facies shear zone at Depot Peak (Figs 1d and 2) was selected to provide some constraints on the timing of high-temperature deformation. The petrography of the pelitic samples is summarized in Table 3.

Northern Prince Charles Mountains

DP-1: Depot Peak

DP-1 is a 20 cm wide pegmatite vein located within a shear zone. These shear zones were described by Stüwe & Hand (1992). They are 1–5 m wide, shallowly north-dipping and post-date the two pervasive ductile deformation phases. They contain a strong north-plunging lineation. The shear zone movement changes from normal to reverse along dip, but the majority of kinematic indicators suggest normal movement (Stüwe & Hand, 1992). Sample DP-1 is dominantly composed of coarse-grained K-feldspar and quartz (5–10 mm). Plagioclase (up to 1 mm) occurs in areas containing finer-grained quartz and unoriented biotite. Anhedral garnet (up to 1 mm) occurs in the comparatively biotite-rich areas. The margin of the pegmatite contains coarse-grained cordierite, biotite and garnet.

DP-11: Depot Peak

DP-11 is a cross-cutting pegmatite that post-dates all deformation at Depot Peak (Fig. 2b). The mineral assemblage in DP-11 is K-feldspar, quartz, biotite, plagioclase and garnet. K-feldspar is perthitic and in some cases is up to 15 mm in diameter. Garnet is euhedral, varies in size from 3 to 15 mm in diameter and contains inclusions of quartz; it occurs throughout the sample. Biotite is scarce and occurs as up to 2 mm anhedral grains. Opaque minerals, apatite, monazite and zircon occur as accessory minerals.

DP-7: Depot Peak

Sample DP-7 contains garnet, sillimanite, K-feldspar, cordierite, spinel and ilmenite, with minor plagioclase, quartz and biotite. Garnet porphyroblasts (up to 15 mm in diameter) make up ~25% of the sample. These
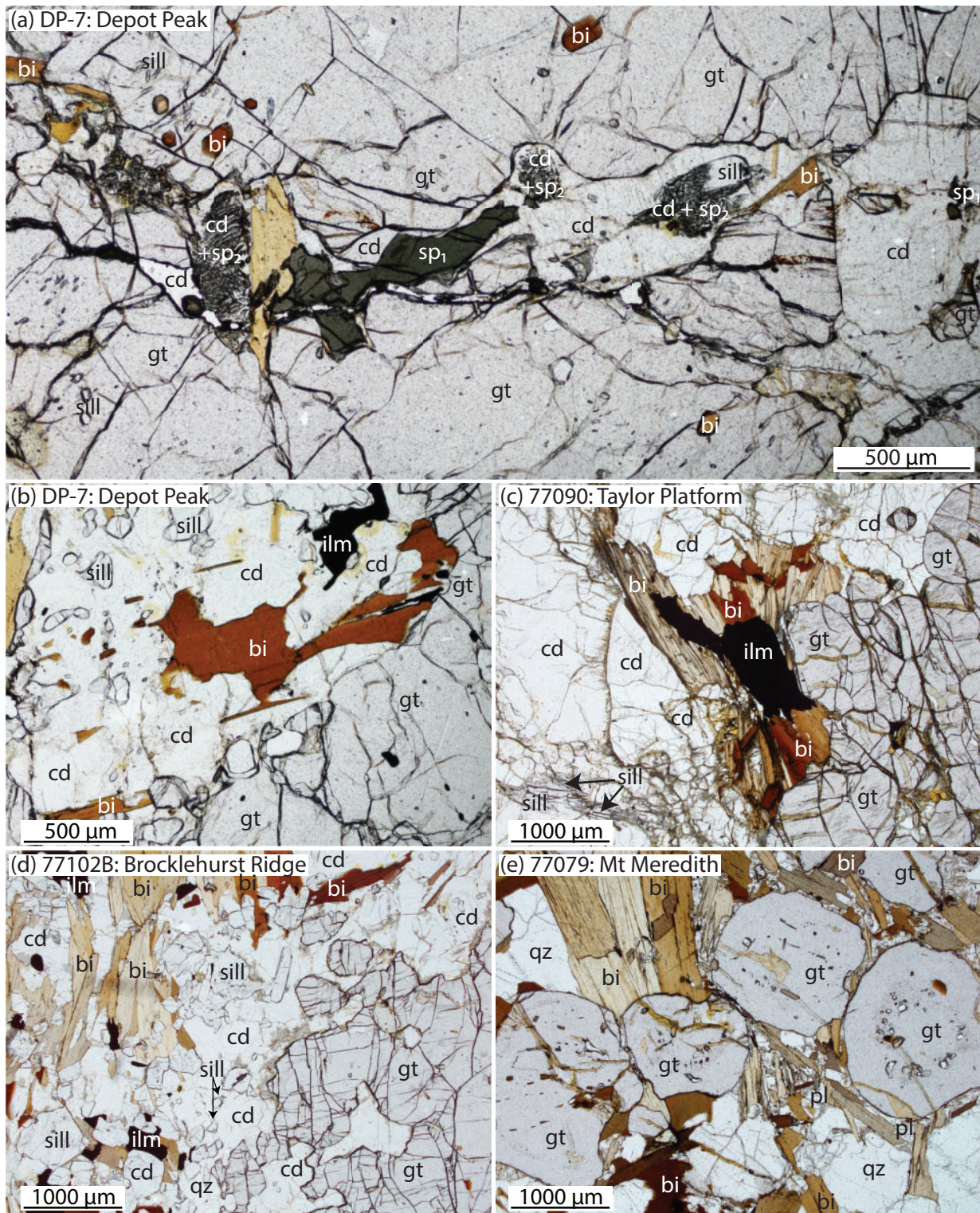
Fig. 3. Photomicrographs of the studied samples. (a) Sample DP-7. Coarse-grained M_1 spinel is separated from M_1 garnet and sillimanite, whereas M_2 cordierite–spinel symplectites replace sillimanite. (b) Sample DP-7. Biotite inclusions within cordierite are optically continuous over length scales of $> 1000\,\mu m$, suggesting cordierite replaced biotite. (c) Sample 77090. (d) Sample 77102B. (e) Sample 77079.

contain abundant inclusions of fine-grained sillimanite, as well as coarser sillimanite, biotite, ilmenite and occasionally K-feldspar (Figs 3a, b and 4). The K-feldspar inclusions in garnet contain rare inclusions of quartz (Fig. 4g). The matrix contains alternating domains that are rich in sillimanite and domains that are rich in K-feldspar. In sillimanite-rich domains, sillimanite (up to 2 mm in length) defines the foliation. Ilmenite and rare
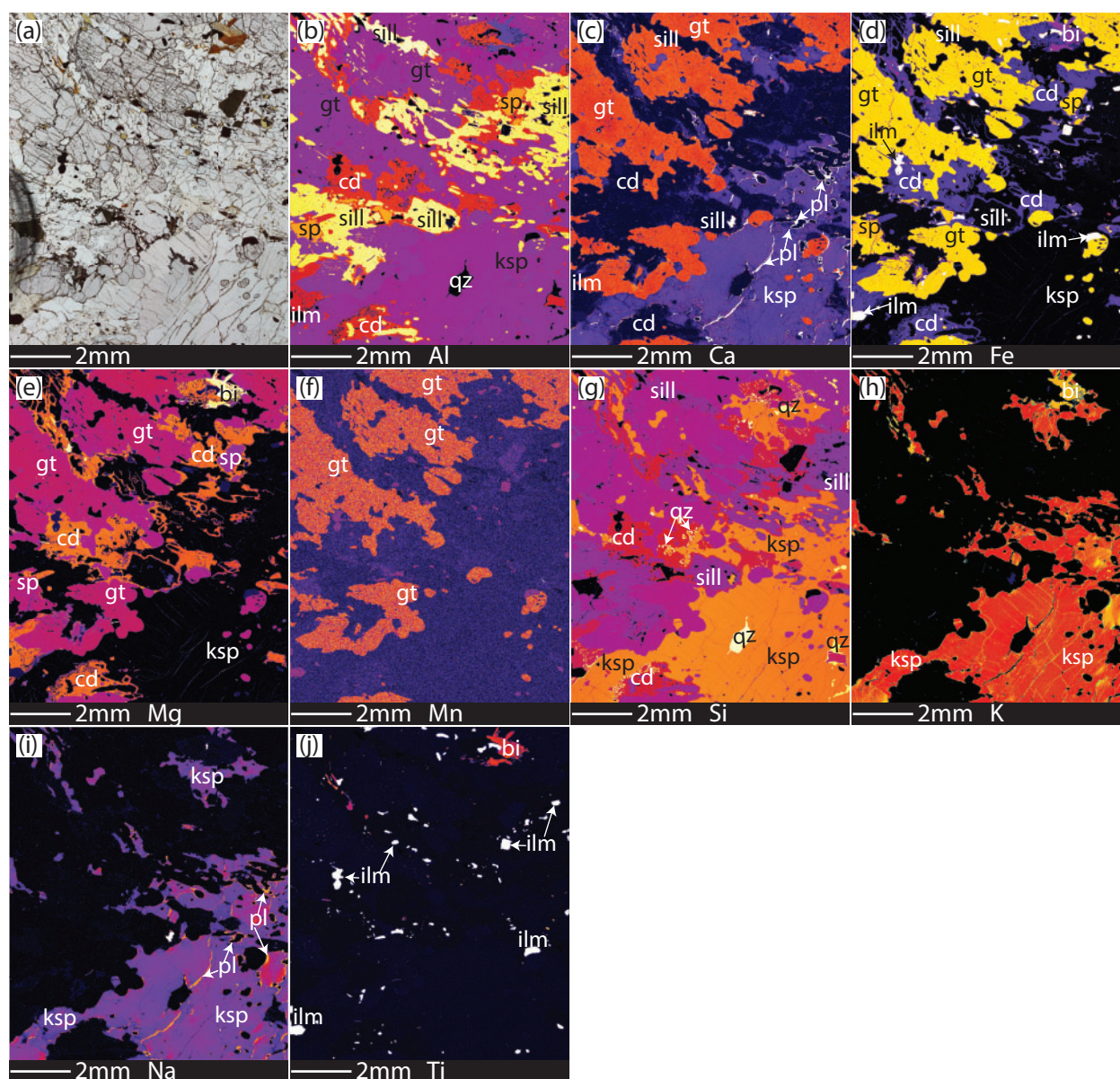
Fig. 4. Compositional maps of DP-7 (Depot Peak) used to calculate the domain composition for phase equilibria modelling. The compositional maps also highlight important mineralogical relationships. (a) Photomicrograph of map area. (b) Al map: cordierite coronas separating coarse-grained garnet and sillimanite; cordierite coronas on coarse-grained spinel. (c) Ca map: plagioclase coronas (white) on sillimanite and as veins separating K-feldspar grains. (d) Fe map: ilmenite occurs as inclusions within garnet and sillimanite and also within cordierite coronas. (e) Mg map: biotite (white) occurs as uncommon, anhedral grains in the matrix. (f) Mn map. (g) Si map: quartz (white) occurs as inclusions in K-feldspar and also as intergrowths with cordierite at the margin of K-feldspar grains. (h) K map. (i) Na map. (j) Ti map.

spinel occur in these domains. K-feldspar-rich domains comprise coarse (5 mm) K-feldspar grains that contain inclusions of ilmenite, garnet and quartz. Biotite is uncommon in sample DP-7, and forms small tabular flakes included in garnet and cordierite and rare, anhedral grains in the matrix (Figs 3a, b and 4). Where flakes of biotite are included in cordierite they are commonly in optical continuity over length scales in excess of 1.5 mm, suggesting that the small flakes are relics of a larger grain (Fig. 3b). Quartz is rare and mainly occurs as inclusions in K-feldspar or as intergrowths separating K-feldspar from cordierite (Fig. 4g). Cordierite

occurs as coronas on ilmenite and sillimanite and also separates spinel from the other phases (Figs 3a and 4). Spinel occurs as grains up to 500 μm, as well as fine-grained, symplectitic intergrowths with cordierite (Fig. 3a). Plagioclase is rare and occurs only as very thin coronas on sillimanite and between K-feldspar grains (Fig. 4c and i).

PCM-83: Else Platform

Sample PCM-83 displays similar mineral assemblages and relationships to DP-7. Coarse-grained garnet

(∼3 mm) and sillimanite (2–5 mm) are separated by coronas of cordierite and spinel (Fig. 5a). Ilmenite occurs as inclusions in garnet but also as a matrix phase, where it occurs as anhedral, coarse grains (up to 1·5 mm; Fig. 5j). Spinel occurs as spinel–cordierite symplectites but also as coarser grains (∼100 μm in diameter; Fig. 5). It can occur in contact with ilmenite but does not occur in contact with garnet or sillimanite (Fig. 5). The majority of the matrix is made up of cordierite. Quartz (up to 1 mm) and K-feldspar (∼500 μm) occur in contact with garnet but do not occur as part of the cordierite–spinel symplectites.

77090: Taylor Platform
Sample 77090 contains garnet, biotite, cordierite, sillimanite, ilmenite and quartz. The rock is unfoliated and is dominantly composed of garnet and cordierite. Garnet grains are euhedral, ∼1 mm in size and commonly form larger aggregates that are up to 10 mm in size (Fig 3c). Garnet grains are commonly inclusion free. Cordierite is abundant and is the main mineral in the matrix (Fig. 3c). It contains fine-grained inclusions of sillimanite that do not have a preferred orientation. It also contains inclusions of euhedral–subhedral biotite (up to 400 μm) and small grains of quartz. In some cases, large cordierite grains also contain small, euhedral garnet grains. Where cordierite occurs in sillimanite-rich domains, it is very coarse grained (up to 20 mm). The margins of some cordierite grains are decorated with fine-grained fibrolite, and where cordierite occurs near garnet or within fractures in garnet it has been pinitized. Sillimanite occurs as inclusions in cordierite and also as coarser grains (500–1000 μm) in the matrix (Fig. 3c). Biotite occurs as fine-grained, euhedral inclusions within cordierite and garnet and also as a matrix phase, where it forms coarser (up to 1 mm) anhedral grains commonly at the boundaries of cordierite or within fractures within garnet (Fig. 3c). Ilmenite usually occurs in contact with biotite, and biotite may be coronitic on ilmenite grains (Fig. 3c). Ilmenite also occurs along grain boundaries of garnet and cordierite.

77102B: Brocklehurst Ridge
Sample 77102B contains garnet, biotite, cordierite, K-feldspar, sillimanite, ilmenite, quartz and minor plagioclase. It has a gneissic foliation defined by biotite, sillimanite and quartzo-feldspathic segregations. Garnet grains are up to 1 mm, anhedral and contain rare fine-grained biotite and quartz. Garnet occurs throughout the sample, except in the quartzo-feldspathic segregations. Sillimanite is up to 1·5 mm in length, defines a foliation and occurs preferentially in areas of the sample that are high in biotite. The sample contains three morphologies of biotite: the first is inclusions in garnet, the second comprises grains up to 1·5 mm that define the foliation (Fig. 3d) and the third generation comprises anhedral grains (up to 2 mm) with no clear preferred orientation. Cordierite is

abundant and occurs throughout the sample; however, it is coarser grained (up to 1·5 mm) in areas that are rich in biotite. It contains inclusions of fine-grained sillimanite, biotite and quartz (Fig. 3d). Plagioclase is rare and is found only in the quartzo-feldspathic domains of the sample. Quartz and K-feldspar occur throughout, but are coarser grained in the quartzo-feldspathic segregations (up to 2 mm). They also occur throughout the sample as finer grains. Ilmenite forms anhedral grains that are commonly in contact with biotite and less commonly in contact with sillimanite.

77079: Mt Meredith
Sample 77079 is a biotite–garnet granofels. It contains garnet, biotite, quartz and minor plagioclase and ilmenite. The sample does not have a foliation. Biotite occurs as euhedral grains (up to 4 mm in length; Fig. 3e) and contains inclusions of zircon, monazite and rare quartz. Garnet grains are euhedral, 2–5 mm in diameter and contain inclusions of fine-grained biotite (up to 200 μm), rare quartz and ilmenite (Fig. 3e). Quartz occurs as coarse, anhedral grains (up to 5 mm, commonly 1–3 mm). Plagioclase occurs as fine, anhedral grains (up to 200 μm), intergrown around coarse biotite crystals near garnet (Fig. 3e). Ilmenite occurs along some biotite grain boundaries or along cleavage planes and also as fine-grained (<100 μm) inclusions within garnet.

East Amery Ice Shelf
72046A: Reinbolt Hills
Sample 72046A displays a similar mineral assemblage and spatial relationship to samples DP-7 and PCM-83 in the nPCM. The sample contains K-feldspar-rich domains as well as domains dominantly composed of coarse-grained garnet and sillimanite. In these domains, garnet and sillimanite form ∼80% of the assemblage. Garnet contains inclusions of fine-grained sillimanite, but coarse garnet and sillimanite are separated by double coronas of cordierite and cordierite–spinel symplectite (Fig. 6). Garnet also contains inclusions of euhedral biotite, ilmenite and rare quartz (Fig. 6e). Plagioclase is rare and occurs as anhedral grains, often in contact with K-feldspar (Fig. 6i). Biotite occurs as euhedral inclusions within garnet (up to 500 μm) and also as anhedral grains in the matrix in contact with K-feldspar, although this is uncommon (Fig. 6e and h). It does not have a preferred orientation. Coarser grained quartz (∼500 μm) occurs as inclusions within K-feldspar in the K-feldspar-rich domains, and as finer grains in contact with K-feldspar in the garnet–sillimanite-rich domains (Fig. 6g). Spinel occurs as coarser grains in direct contact with ilmenite and as fine-grained symplectites intergrown with cordierite (Fig. 6a and d).

77223: McKaskle Hills
Sample 77223 contains garnet, biotite, plagioclase, K-feldspar, cordierite, quartz, ilmenite and rutile in domains of differing mineralogy. Some domains are
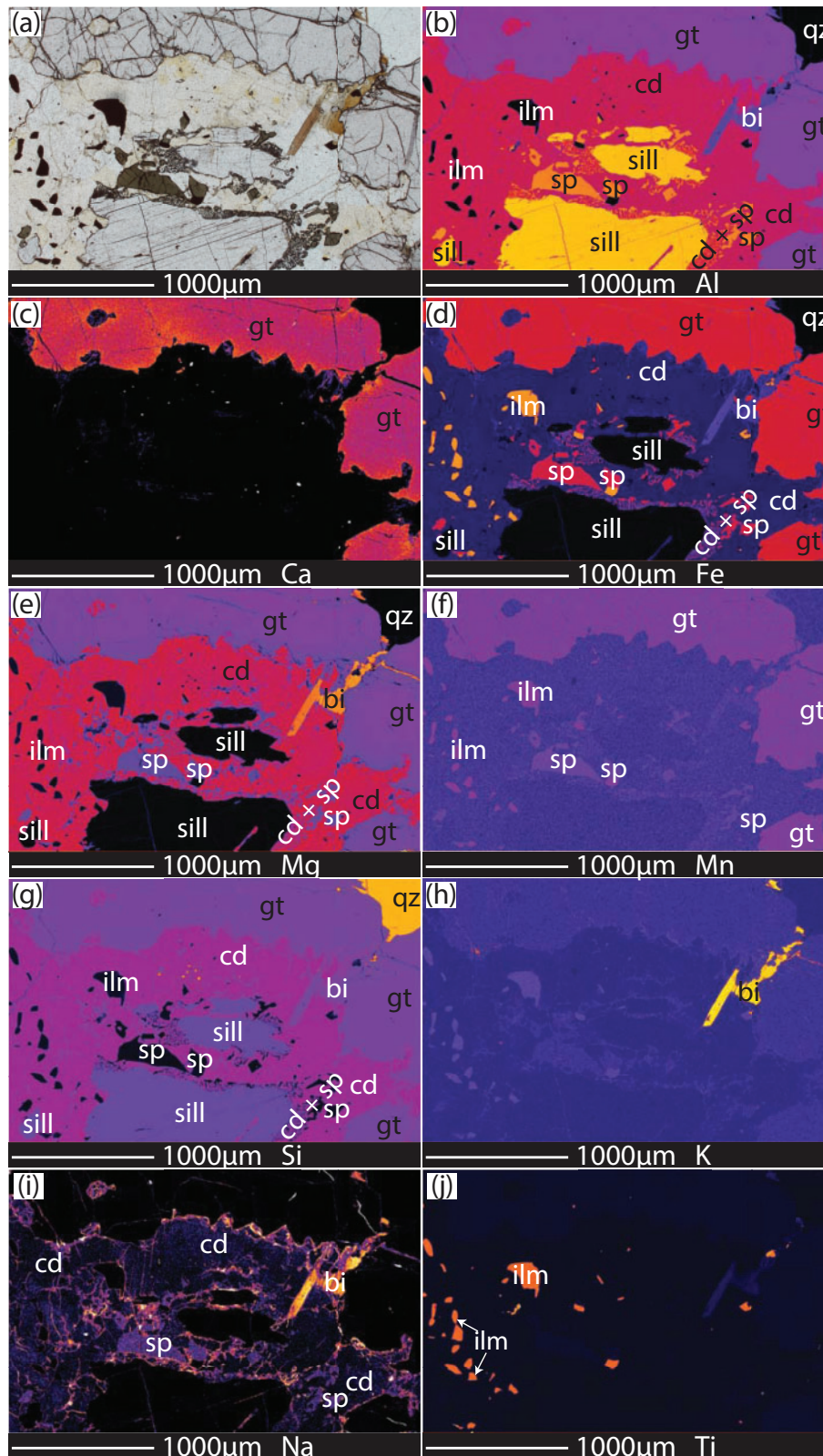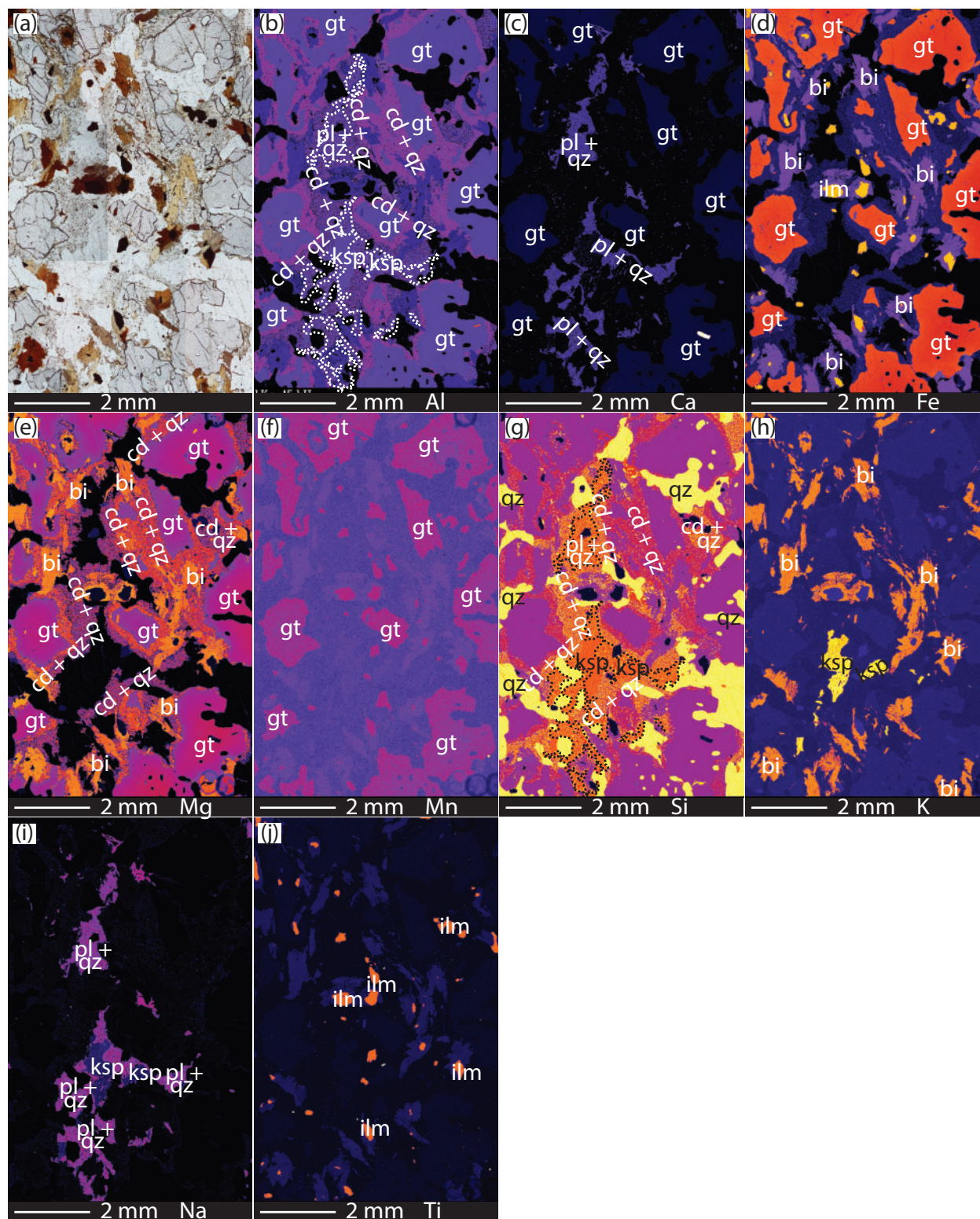
Fig. 5. Compositional maps of PCM-83 (Else Platform), used to calculate the domain composition for phase equilibria modelling. The compositional maps also highlight important mineralogical relationships. (a) Photomicrograph of map area. (b) Al map: cordierite–spinel symplectites and cordierite moats separate sillimanite and garnet. (c) Ca map: garnet shows minor enrichment in calcium at the rims. (d) Fe map: ilmenite occurs within the cordierite moat and in contact with spinel. (e) Mg map. (f) Mn map. (g) Si map. (h) K map. (i) Na map: cordierite, spinel and biotite contain minor amounts of Na. (j) Ti map.
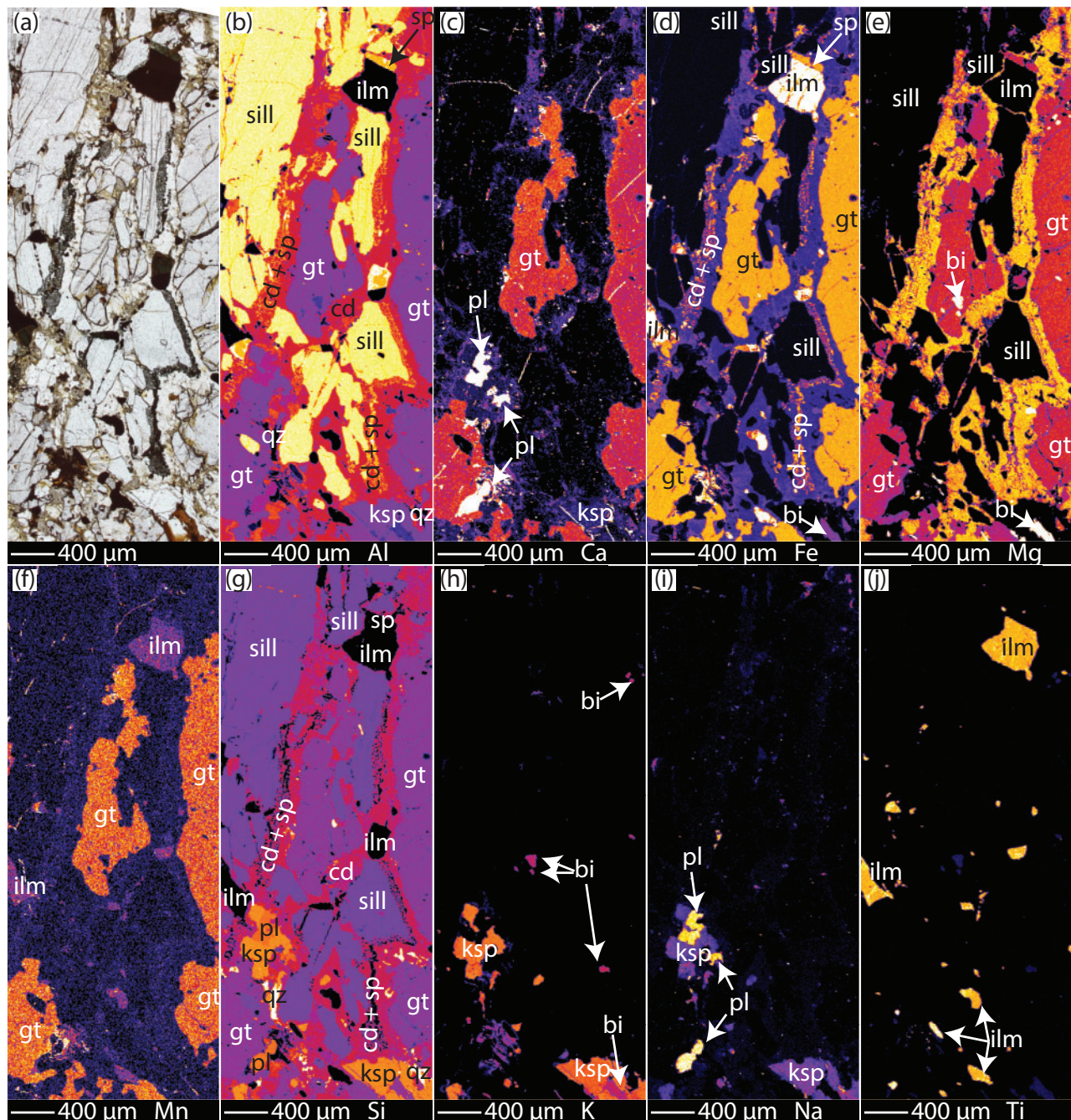
Fig. 6. Compositional maps of 72046A (Reinbolt Hills), used to calculate the domain composition for phase equilibria modelling. The compositional maps also highlight important mineralogical relationships. (a) Photomicrograph of map area. (b) Al map: sillimanite and garnet separated by cordierite and cordierite–spinel reaction textures. (c) Ca map: anhedral plagioclase (white) occurs in contact with garnet or K-feldspar. Garnet shows minor enrichment at the rims. (d) Fe map: ilmenite is separated from sillimanite by a corona of cordierite but can occur in contact with spinel. (e) Mg map: biotite occurs as small grains included in garnet. (f) Mn map. (g) Si map: quartz (white) occurs as anhedral grains, usually in contact with K-feldspar. (h) K map: there is a general paucity of biotite, which occurs as inclusions in garnet and K-feldspar. (i) Na map. (j) Ti map.

mainly composed of quartz, plagioclase and minor K-feldspar. These domains contain euhedral rutile crystals, but very little biotite. Other domains are richer in ferromagnesian minerals. In these domains, garnet porphyroblasts are commonly surrounded by cordierite–quartz symplectites, which can be up to 700 μm wide (Fig. 7b and e). These are commonly in

contact with finer-grained symplectites of quartz and cordierite in a second corona structure (Fig. 7b and e). K-feldspar is commonly separated from other minerals by plagioclase–quartz symplectites, and rarely by cordierite–quartz symplectites (Fig. 7c and i). Cordierite occurs as part of a quartz–cordierite symplectite and not as coarse grains. Biotite is abundant in

Fig. 7. Compositional maps of 77223 (McKaskle Hills), used to calculate the domain composition for phase equilibria modelling. The compositional maps also highlight important mineralogical relationships. (a) Photomicrograph of map area. (b) Al map: double cordierite–quartz symplectites surround garnet, with cordierite-rich symplectites adjacent to garnet and more quartz-rich symplectites as a second layer. Plagioclase–quartz symplectites occur with K-feldspar and are outlined in white dashed lines. (c) Ca map: highlighting the plagioclase–quartz symplectites. (d) Fe map. (e) Mg map. (f) Mn map. (g) Si map. (h) K map: biotite occurs as coarse grains on ilmenite grains as well as intergrown with quartz. (i) Na map. (j) Ti map.

the garnet–cordierite–quartz domains. In some cases, the edges of biotite grains are intergrown with quartz or biotite is included in cordierite–quartz symplectites (Fig. 7h). Ilmenite (up to 500 μm) often occurs included in or in contact with biotite (Fig. 7j). It occurs commonly in the ferromagnesian domains, but is less common in the domains containing quartz and plagioclase. Rutile occurs in the quartz–plagioclase-rich domains and as inclusions in garnet. It may occur in contact with ilmenite, where the two minerals appear to form a single euhedral grain. Rare sillimanite inclusions occur in garnet but sillimanite does not occur in the matrix.

METHODS

Monazite U–Pb LA-ICP-MS geochronology

U–Pb isotope data were obtained by laser ablation–inductively coupled plasma–mass spectrometry (LA-ICP-MS) on *in situ* monazite grains in thin section. Prior to LA-ICP-MS analysis the monazite grains were imaged using a back-scattered electron detector on a Phillips XL30 SEM to determine their microstructural locations and any compositional variations. For samples containing mineral reaction microstructures, monazite grains were qualitatively mapped using a Cameca SXFive electron microprobe, to determine variations in rare earth element (REE) concentrations.

LA-ICP-MS analyses were performed at the University of Adelaide, following the method of Payne *et al.* (2008). U–Pb isotope analyses were acquired using a New Wave 213 nm Nd–YAG laser coupled with an Agilent 7500cs ICP-MS system. Ablation of monazites was performed in a He-ablation atmosphere at a frequency of 4 Hz. A spot size of 12 μm was used for all samples. The total acquisition time of each analysis was 100 s. This included 40 s of background measurement, 10 s of the laser firing with the shutter closed to allow for beam stabilization, and 50 s of sample ablation. Isotopes measured were ^{204}Pb, ^{206}Pb, ^{207}Pb and ^{238}U for dwell times of 10, 15, 30 and 15 ms, respectively.

Monazite data were reduced using Glitter software (Griffin *et al.*, 2004). Elemental fractionation and mass bias was corrected using the monazite standard MAdel [thermal ionization mass spectrometry (TIMS) normalization data: ^{207}Pb/^{206}Pb $= 491 \cdot 0 \pm 2 \cdot 7$ Ma, ^{206}Pb/^{238}U $= 518 \cdot 37 \pm 0 \cdot 99$ Ma and ^{207}Pb/^{235}U $= 513 \cdot 13 \pm 0 \cdot 19$ Ma: updated from Payne *et al.* (2008) with additional TIMS analyses]. Throughout the course of this study, MAdel yielded weighted mean ages of ^{207}Pb/^{206}Pb $= 491 \pm 4$ Ma, ^{206}Pb/^{238}U $= 519 \pm 1$ Ma and ^{207}Pb/^{235}U $= 513 \pm 1$ Ma ($n = 218$). Data accuracy was monitored using monazite standard 94-222/Bruna-NW (*c.* 450 Ma: Payne *et al.*, 2008). As a secondary standard, 94-222 yielded weighted mean ages of ^{207}Pb/^{206}Pb $= 463 \pm 7$ Ma, ^{206}Pb/^{238}U $= 450 \pm 2$ Ma and ^{207}Pb/^{235}U $= 452 \pm 2$ Ma ($n = 83$).

Mineral chemistry

X-ray compositional maps and chemical analyses of minerals were obtained using a Cameca SXFive electron microprobe at the University of Adelaide. The SXFive is equipped with five wavelength-dispersive X-ray detectors, with four utilizing large diffracting crystals. Beam conditions of 15 kV and 20 nA with a focused spot were used for all point analyses, and settings of 15 kV and 150 nA were used for compositional mapping. Calibration was performed on certified synthetic and natural mineral standards from Astimex Ltd and P&H Associates. Data calibration and reduction was carried out in Probe for EPMA, distributed by Probe Software Inc.

Phase equilibria modelling

Samples DP-7, PCM-83, 72046A and 77223 preserve localized mineral reaction microstructures. Therefore, chemical compositions for phase equilibria modelling were determined by combining measured mineral chemistry with estimates of the mineral modal abundances (Table 4) derived from qualitative element maps of a region interpreted to be relevant to the formation of the mineral reaction textures (Figs 4–7). Modal abundances were determined by thresholding chemical maps in the software ImageJ. Although a whole-rock geochemical analysis may also provide a valid chemical composition for the purposes of phase equilibria modelling, we adopt a conservative view that targets domains in the rock that record the growth of new minerals, and the bulk chemistry is herein referred to as a 'domain composition' (see Kelsey & Hand, 2015) to distinguish it from whole-rock geochemistry. We accept that this two-dimensional compositional determination is necessarily limited, but nonetheless have assumed for the purposes of modelling that this is a realistic composition.

The Fe^{3+} content of minerals was calculated from microprobe analyses using the assumed stoichiometric method of Droop (1987). As mineral chemistry is used in the derivation of domain composition, Fe_2O_3 is constrained by the abundance of the Fe^{3+}-bearing minerals. The amount of Fe_2O_3 may affect the stability of the oxides such as magnetite$_{(ss)}$, ilmenite$_{(ss)}$ and rutile as well as some silicate minerals, but small variations in Fe_2O_3 are not considered to affect the topology of the pseudosections significantly (e.g. Diener & Powell, 2010; Johnson & White, 2011; Boger *et al.*, 2012; Morrissey *et al.*, 2015).

H_2O was constrained by the abundance of H_2O-bearing minerals (biotite and cordierite) and a conservative estimate of the H_2O content of biotite and cordierite in granulites (e.g. Deer *et al.*, 1992; Bose *et al.*, 2005; Cesare *et al.*, 2008; Rigby & Droop, 2011). The samples preserve low-H_2O mineral assemblages with almost no matrix biotite, consistent with dehydration owing to melt loss (Fyfe, 1973; Powell & Downes, 1990; White & Powell, 2002).

Table 4: Mineral composition and modal proportions used for bulk composition calculations

	Sample DP-7									Sample PCM-83						
Mode %:	gt 29	sill 17	bi 1	cd 15	ilm 2	sp 1	qz 1	pl 1	ksp 33	gt 24	sill 16	bi 2	cd 48	ilm 2	sp 4	qz 4
SiO_2	38·15	36·88	37·65	48·27	0·01	0·02	98·54	67·86	63·43	36·96	36·65	37·13	48·65	0	0·01	99·90
TiO_2	0·02	0·02	4·30	0·01	50·55	0·04	0·06	0·02	0·04	0·02	0·03	4·89	0	52·95	0·04	0·05
Al_2O_3	21·69	62·37	13·54	31·89	0·00	58·18	0·05	20·62	18·18	21·28	62·54	16·41	32·98	0·00	57·99	0·04
Fe_2O_3	1·17	0·38	—	—	5·05	1·78	—	—	—	2·48	1·14	—	—	0	4·26	0
FeO	29·15	0·00	10·78	6·42	42·67	30·80	0·02	0·02	0	31·12	0	9·84	6·08	46·68	27·61	0·05
MgO	8·37	0	17·72	10·09	1·49	6·65	0·03	0	0	5·92	0·02	16·34	10·06	0·08	6·33	0·02
CaO	0·92	0	0	0·02	0	0·01	0·01	5·04	0·69	1·23	0	0·01	0	0	0	0·02
Na_2O	0	0	0·18	0·03	0·01	0·06	0	6·92	3·32	0·02	0·02	0·14	0·03	0	0·12	0
K_2O	0·01	0	9·77	0	0	0	0	0·04	10·81	0	0	8·70	0	0·02	0·01	0
H_2O	0	0	3·50	1·50	0	0	0	0	0	0	0	3·50	1·50	0	0	0
Total	99·47	99·65	97·44	98·23	99·79	97·55	98·71	100·52	96·47	99·02	100·40	96·96	99·30	99·73	96·37	100·08

	Sample 72046A									Sample 77223						
Mode %:	gt 25	sill 35	bi 1	cd 27	ilm 3	sp 3	qz 1	pl 2	ksp 3	gt 28	bi 11	cd 20	ilm 3	q 27	pl 8	ksp 3
SiO_2	38·42	36·65	38·15	49·43	0·06	0·02	99·90	61·56	64·88	38·00	35·12	48·77	0·00	98·28	57·96	64·20
TiO_2	0·01	0·03	5·81	0·03	51·33	0·04	0·05	0·00	0·02	0·00	3·67	0·00	54·24	0·06	0·01	0·00
Al_2O_3	21·70	62·54	14·76	33·38	0	58·64	0·04	24·49	19·00	21·44	14·88	33·57	0·03	0·02	25·95	18·84
Fe_2O_3	0·39	1·14	—	—	3·51	3·96	—	—	—	1·65	0·57	—	0·57	—	—	—
FeO	29·29	0	9·87	4·96	42·90	27·47	0·05	0·18	0·02	28·88	13·92	5·02	42·76	0·17	0·02	0·00
MgO	7·86	0·02	17·44	11·24	1·38	7·78	0·02	0	0·02	7·98	13·60	10·96	1·24	0·02	0·01	0·00
CaO	1·42	0	0	0·02	0·02	0·01	0·02	5·85	0·15	1·52	0·02	0·00	0·01	0·03	7·37	0·03
Na_2O	0	0·02	0·26	0·05	0·05	0·09	0	8·17	1·94	0·00	0·07	0·01	0·00	0·03	7·78	1·33
K_2O	0·01	0	9·61	0·00	0·01	0	0	0·15	13·62	0·00	8·84	0·00	0·02	0·00	0·12	14·05
H_2O	0	0	3·50	1·50	0	0	0	0	0	0·00	3·50	1·50	0·00	0·00	0·00	0·00
Total	99·09	100·40	99·39	100·61	99·25	98·01	100·08	100·40	99·66	99·47	94·19	99·83	98·87	98·61	99·21	98·46

We cannot unequivocally prove that melt was present in the samples. However, biotite is interpreted to be relict, and in samples such as PCM-83 no newly formed K-feldspar occurs within the reaction microstructures. This suggests that melt may have been generated and was subsequently removed from the sample. This interpretation is consistent with the presence of structurally late Cambrian-age pegmatite veins in some locations (this study; Hand *et al.*, 1994*a*) that contain garnet and cordierite, suggesting they were derived from the melting of metasediments. To reflect the likely composition prior to final melt loss in samples DP-7, PCM-83, 72046A and 77223, a small amount of melt (7 mol %; equivalent to the melt percolation threshold; e.g. Rosenberg & Handy, 2005) was integrated into the composition using the method of Anderson *et al.* (2013). This method involves calculating a $T–M_{melt}$ section from the currently preserved, residual domain composition (at $M = 0$) to the composition of an average leucogranite (at $M = 1$). Based on the residual composition, the pressure for the $T–M_{melt}$ section for each sample was set at 6 kbar after a first pass estimate of metamorphic conditions for the cordierite–spinel-bearing assemblages. The integration of 7 mol % melt reflects the probability that melt was still present in minor amounts at the metamorphic peak, and was subsequently crystallized or lost (e.g. Brown & Korhonen, 2009; White & Powell, 2011; Korhonen *et al.*, 2013*a*). It also allows for an assessment of the sensitivity of the mineral assemblages to the effect of melt and H_2O content (e.g. Anderson *et al.*, 2013; Morrissey *et al.*, 2013).

Samples with dominantly Cambrian monazite populations

Samples 77090, 77102B and 77079 do not contain localized mineral reaction microstructures. Therefore, the whole-rock chemical composition was considered to be representative of the equilibration volume at the time of metamorphism. Whole-rock chemical compositions were analysed at Franklin and Marshall College, Pennsylvania. The composition was determined by crushing a representative amount of the rock and homogenizing the sample using a tungsten carbide mill. Major elements were analysed by fusing a 0·4 g portion of the powdered sample with lithium tetraborate for analysis by X-ray fluorescence (XRF). Trace elements were analysed by mixing 7 g of crushed rock powder with Copolywax powder and measurement by XRF. For these samples, Fe_2O_3 was estimated at 5% of the total Fe, based on the observed mineral assemblage, the modal abundance of Fe^{3+}-bearing minerals and an appraisal of the ferric iron content of those minerals as determined for measured mineral compositions using the method of Droop (1987). H_2O was also estimated based on the observed mineral assemblage in the rock, the modal abundances of H_2O-bearing minerals and a conservative estimate of the H_2O content of biotite and cordierite in granulites.

Mineral equilibria for the samples were calculated using THERMOCALC v3.33, using the internally consistent dataset of Powell & Holland (1988; dataset tcds55 November 2003 update), for the geologically realistic system NCKFMASHTO (Na_2O–CaO–K_2O–FeO–MgO–Al_2O_3–SiO_2–H_2O–TiO_2–Fe_2O_3). The following activity–composition (*a*–*x*) relationships were used: silicate melt, garnet and biotite (White *et al.*, 2007); cordierite (Holland & Powell, 1998); spinel, orthopyroxene and magnetite (White *et al.*, 2002); ilmenite and hematite (White *et al.*, 2000); muscovite (Coggon & Holland, 2002); and plagioclase and K-feldspar (Holland & Powell, 2003). Rutile, the aluminosilicates and H_2O are pure end-member phases. The whole-rock or domain composition for each sample used in the calculation of the mineral equilibria pseudosections is given above each pseudosection (see below).

GEOCHRONOLOGY RESULTS
Monazite U–Pb geochronology
U–Pb data for all monazite analyses, as well as information on grain size and textural location, are presented in Supplementary Data Appendix S1 (supplementary data are available for downloading at http://www.petrology.oxfordjournals.org). All samples are plotted on Tera–Wasserburg plots to assist with visualization of the effects of common lead in some samples. The weighted average age is the $^{206}Pb/^{238}U$ age. Dashed ellipses denote analyses that have been excluded as outliers using linearized probability plots, but are shown for completeness. For some samples, ages are calculated using isochrons anchored to a model common Pb composition (single stage; Stacey & Kramers, 1975) at the approximate age of formation.

Northern Prince Charles Mountains
DP-1: Depot Peak
In sample DP-1, monazite is preferentially located near the biotite-rich areas of the pegmatite. Monazite grains are coarse grained (commonly 100–200 μm in diameter, with some grains 20–50 μm), and some grains display patchy zoning (Fig. 8a). Thirty-three analyses were collected from 10 grains. One analysis was excluded from further calculations using a linearized probability plot. The remaining 32 analyses yield a $^{206}Pb/^{238}U$ weighted average age of 487 ± 3 Ma (MSWD = 1·30). This is identical to the age calculated from an isochron anchored to the single-stage Pb age of 487 ± 3 Ma (Fig. 9a; MSWD = 1·20).

DP-11: Depot Peak
In sample DP-11, monazite is distributed throughout the sample but is coarsest and most abundant in contact with garnet or apatite. Grains are anhedral, unzoned and predominantly vary in size from 20 to 50 μm in diameter, with some grains elongate and up to 200 μm in length (Fig. 8b). Twenty-two analyses were collected from 10 grains. Two discordant analyses were excluded from the calculation of the weighted average age (Fig. 9b). The remaining 20 analyses yield a $^{206}Pb/^{238}U$ weighted average age of 499 ± 3 Ma (MSWD = 1·01). This is identical to the age calculated from an isochron anchored to the single-stage Pb age of 499 ± 3 Ma (MSWD = 1·05).

DP-7: Depot Peak
In sample DP-7, monazite is abundant and occurs as inclusions within garnet, within cordierite–spinel–ilmenite reaction textures and along grain boundaries in the matrix. Monazite grains are 50–100 μm in diameter and some grains display patchy zoning (Fig. 8f). Forty-two analyses were collected from 16 grains. Monazite grains hosted within coarse-grained, M_1 minerals are denoted as filled grey ellipses in Fig. 9c. The analyses define an older, discordant population and a younger, more clustered population (Fig. 9c). Many grains, including those hosted in garnet, yielded multiple ages in different domains. However, the monazite grains hosted in garnet that yielded younger ages are located on microfractures and are therefore not isolated from the matrix. There is a link between monazite zoning and age. Areas with high Th and low Y tended to yield younger ages (Fig. 8f). A Tera–Wasserburg plot yields a lower intercept of 505 ± 22 Ma and an upper intercept of 928 ± 28 Ma (Fig. 9c; MSWD = 0·88; *n* = 42). The $^{206}Pb/^{238}U$ weighted average age for the 13 analyses making up the younger population (outlined in the dashed box) is 532 ± 5 Ma (MSWD = 1·18). This is identical to the age calculated from an isochron anchored to the single-stage Pb age of 532 ± 4 Ma (MSWD = 0·97).

PCM-83: Else Platform
In sample PCM-83, monazite is distributed throughout the sample, including within coarse-grained garnet and sillimanite, within cordierite and adjacent to ilmenite in the reaction microstructures. Monazite grains are 20–70 μm in diameter, with some grains showing well-defined, patchy zoning patterns (Fig. 8g). Thirty-five analyses were collected from 17 grains. Monazite grains hosted within coarse-grained, M_1 minerals are denoted as filled grey ellipses in Fig. 9d. A Tera–Wasserburg plot of all analyses yields a poorly defined discordia with an upper intercept age of 872 ± 31 Ma and a lower intercept age of 551 ± 24 Ma (Fig. 9d; MSWD = 0·96). The seven analyses making up the younger population (outlined in the dashed box) yield a $^{206}Pb/^{238}U$ weighted average age of 519 ± 5 Ma (MSWD = 1·13). The younger ages come from grains located within cordierite or adjacent to ilmenite in the reaction textures, whereas all grains located within coarse-grained, M_1 minerals yield older ages. However, some older grains, or grains preserving older domains, are also located in the cordierite–spinel reaction textures, and grains that yield younger ages may also yield older ages in other domains (Fig. 8g). Unlike DP-7, younger ages appear to come from zones that are lower in Th and higher in Y (Fig. 8g).

77090: Taylor Platform
In sample 77090, the majority of monazite grains occur throughout the matrix. One grain occurs within garnet,
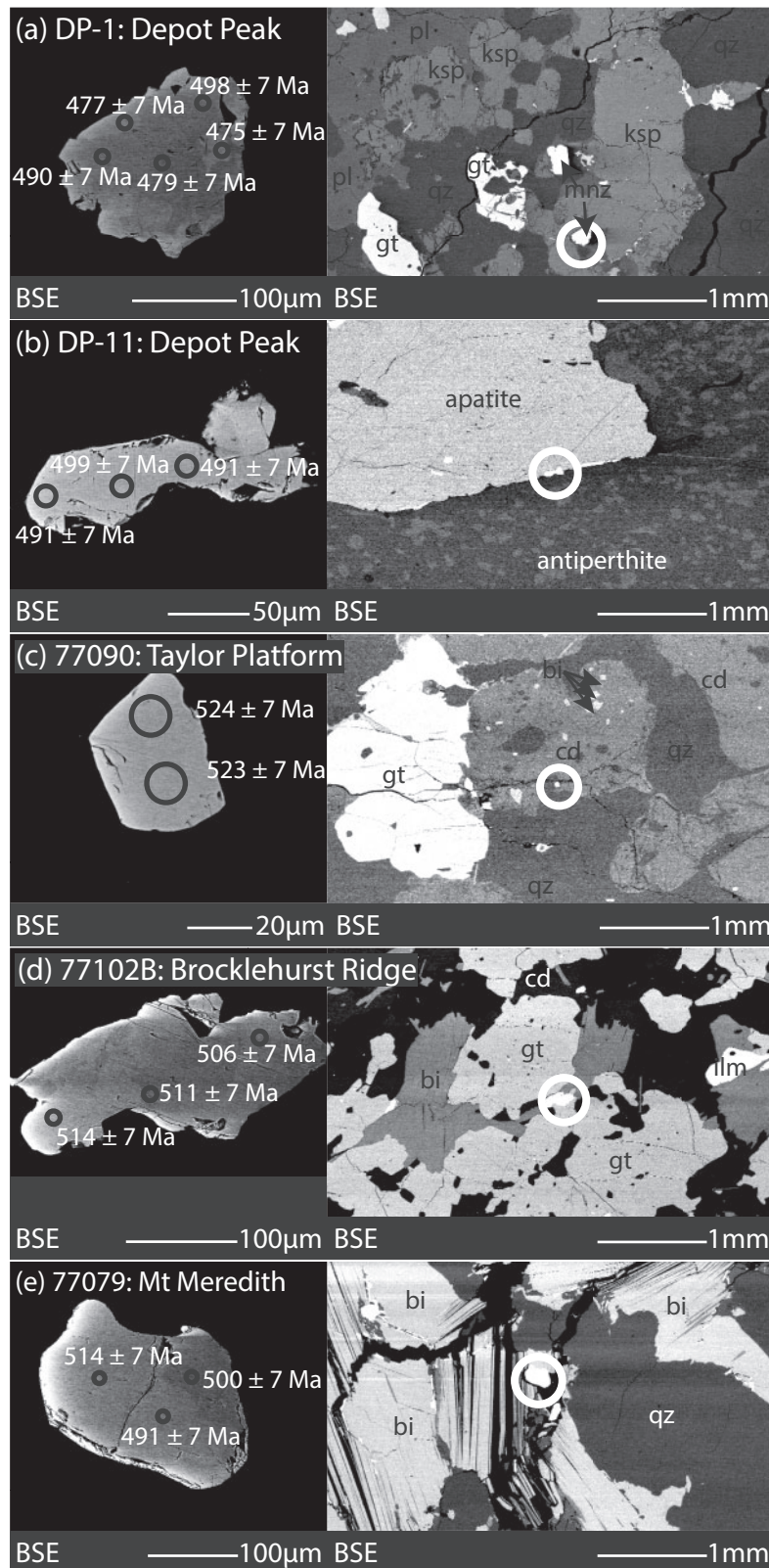
Fig. 8. Backscattered electron (BSE) images of representative monazite grains from each sample, and their textural location. The ages shown are the $^{206}Pb/^{238}U$ ages. For samples with localized mineral reaction textures, compositional maps of representative monazite grains that yield Cambrian ages are also shown. In the compositional maps, red denotes areas of higher concentration. (a) Sample DP-1; (b) sample DP-11; (c) sample 77090; (d) sample 77102B; (e) sample 77079; (f) sample DP-7; (g) sample PCM-83; (h) sample 72046A; (i) sample 77223.
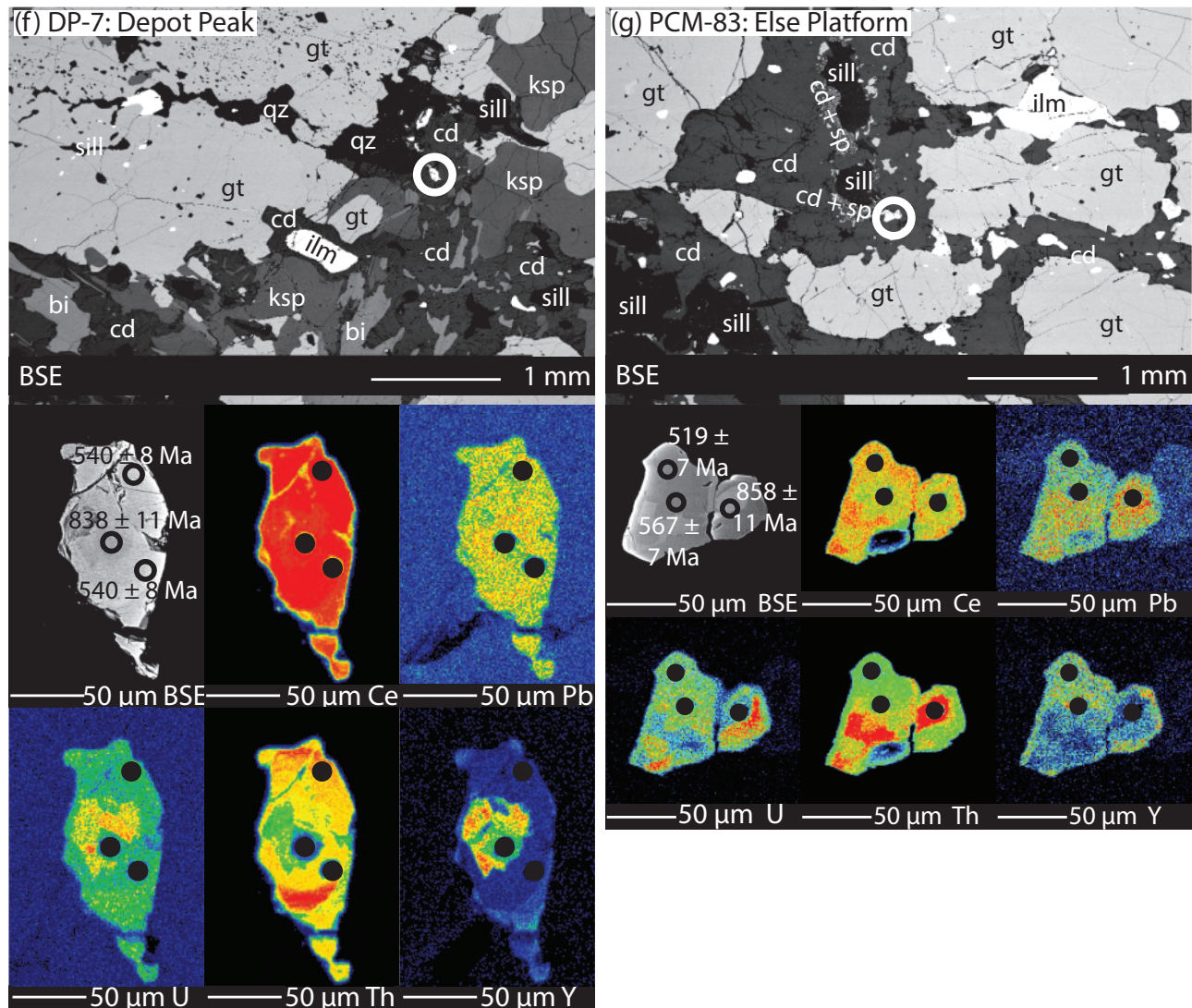
Fig. 8. Continued

although it is located along a microfracture. Monazite grains are 20–50 μm in diameter and the majority of grains are unzoned (Fig. 8c). Thirty-two analyses were collected from 17 grains. The grain hosted within garnet yields an age of *c.* 513 Ma. However, as the majority of the grains are unzoned and located within the matrix it is difficult to draw links between age and textural location, or morphology. A younger population was inferred using a linearized probability plot (outlined in the dashed box; Fig. 9e). This population has a weighted average age of 517 ± 4 Ma (MSWD = 1·40; *n* = 20).

77102B: Brocklehurst Ridge
In sample 77012B, monazite occurs within the matrix as well as within garnet grains. Analysed grains vary in size from 20 to 200 μm in diameter, with the majority of grains displaying patchy zoning (Fig. 8d). Thirty analyses were collected from 15 grains. The analyses fall

within two populations. The younger population yields a $^{206}Pb/^{238}U$ weighted average age of 516 ± 4 Ma (Fig. 9f; MSWD = 1·30; *n* = 21). The age of this population calculated from an isochron anchored to the single-stage Pb age is 515 ± 3 Ma (MSWD = 1·30). The older population is discordant but gives an age of *c.* 900 Ma. Monazite grains hosted within garnet yield both older and younger ages (Supplementary Data Appendix S1), and patchy zoning makes it difficult to identify core–rim relationships. However, the older ages are commonly from monazite grains > 200 μm in diameter.

77079: Mt Meredith
In sample 77079, the majority of monazite grains occur within biotite or adjacent to biotite grain boundaries, but some are located within quartz. No monazite was observed in garnet. Monazite grains have variable sizes, from 20 to 200 μm in diameter (Fig. 8e). Some grains
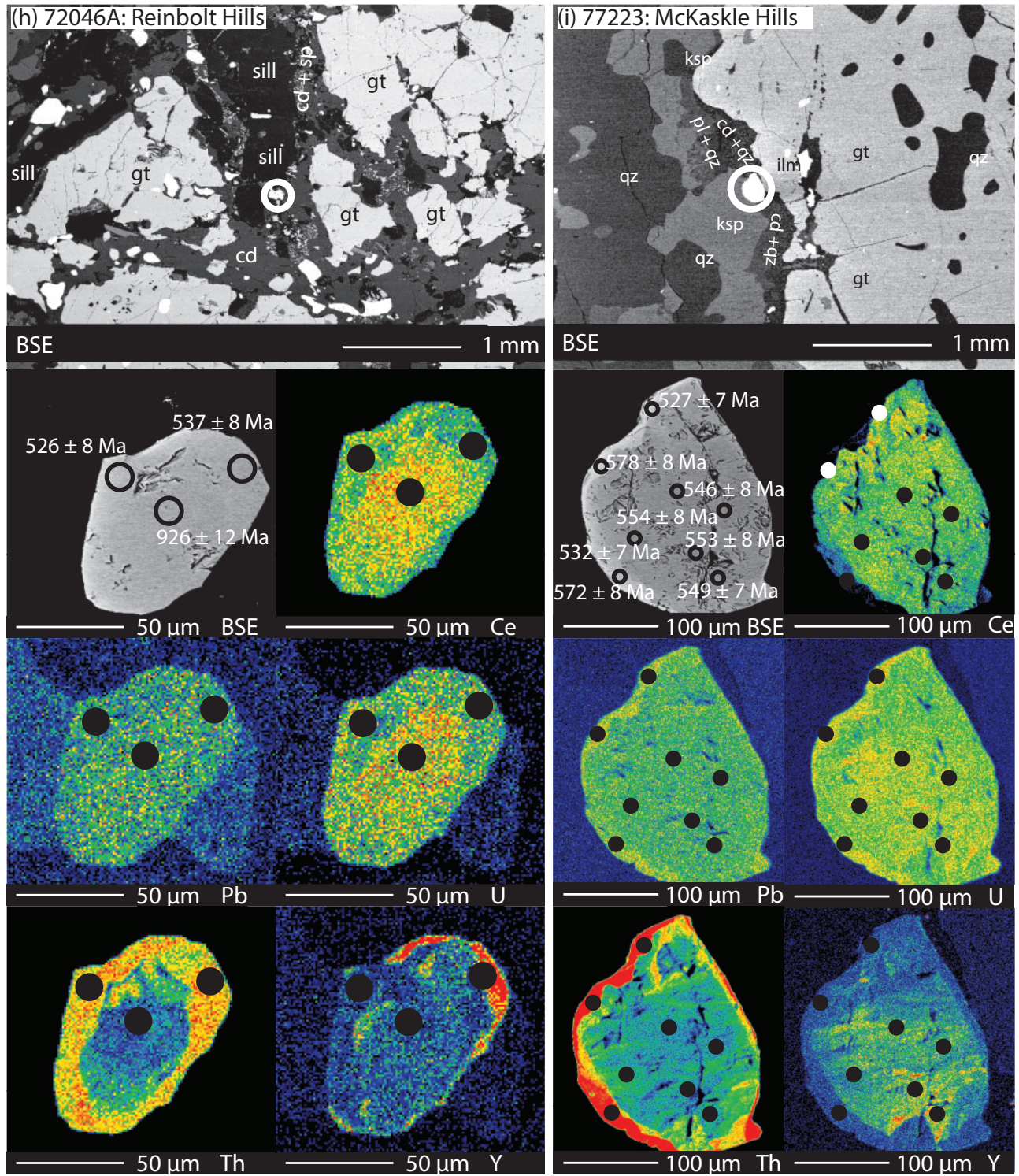
Fig. 8. Continued

display weak zoning but the majority are unzoned (Fig. 8e). Thirty analyses were collected from 14 grains. One discordant analysis was excluded from the calculations. A Tera–Wasserburg plot of the remaining 29 analyses yields a lower intercept of 504 ± 11 Ma and a poorly defined upper intercept of 928 ± 99 Ma (Fig. 9g;

MSWD = 0·28). This upper intercept is defined by one old, near-concordant analysis with a $^{206}Pb/^{238}U$ age of 908 ± 12 Ma. This analysis is from a grain located within quartz. The remaining 28 analyses define a younger population with a $^{206}Pb/^{238}U$ weighted average age of 504 ± 3 Ma (MSWD = 1·4).
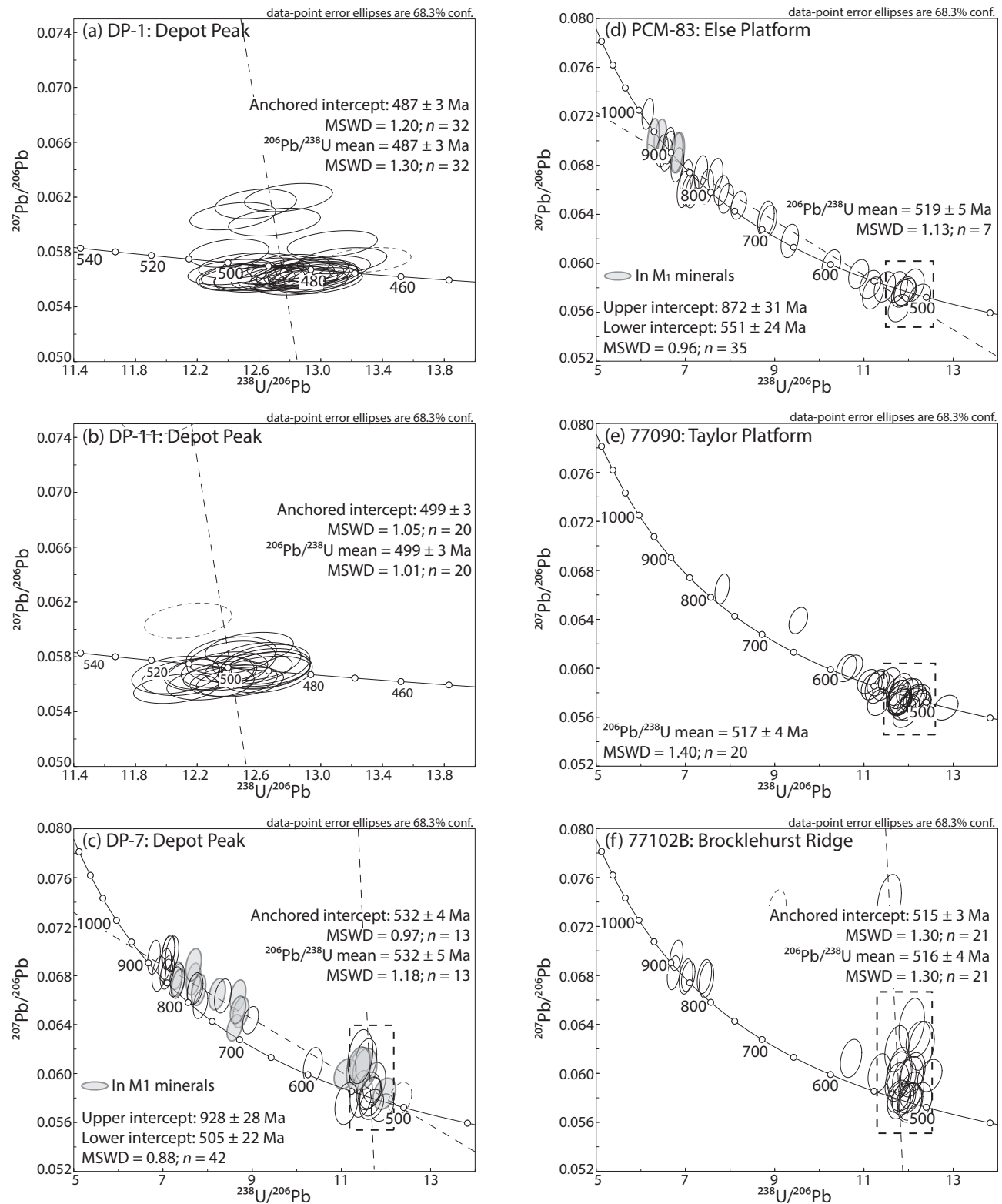
Fig. 9. Tera–Wasserburg concordia plots for each of the samples in the study. Analyses denoted by dashed, grey ellipses are excluded from the calculation of weighted averages and intercept ages. The dashed boxes show the populations used for the calculation of weighted average ages. (a) Sample DP-1; (b) sample DP-11; (c) sample DP-7; (d) sample PCM-83; (e) sample 77090; (f) sample 77102B; (g) sample 77079; (h) sample 72046A; (i) sample 77223.
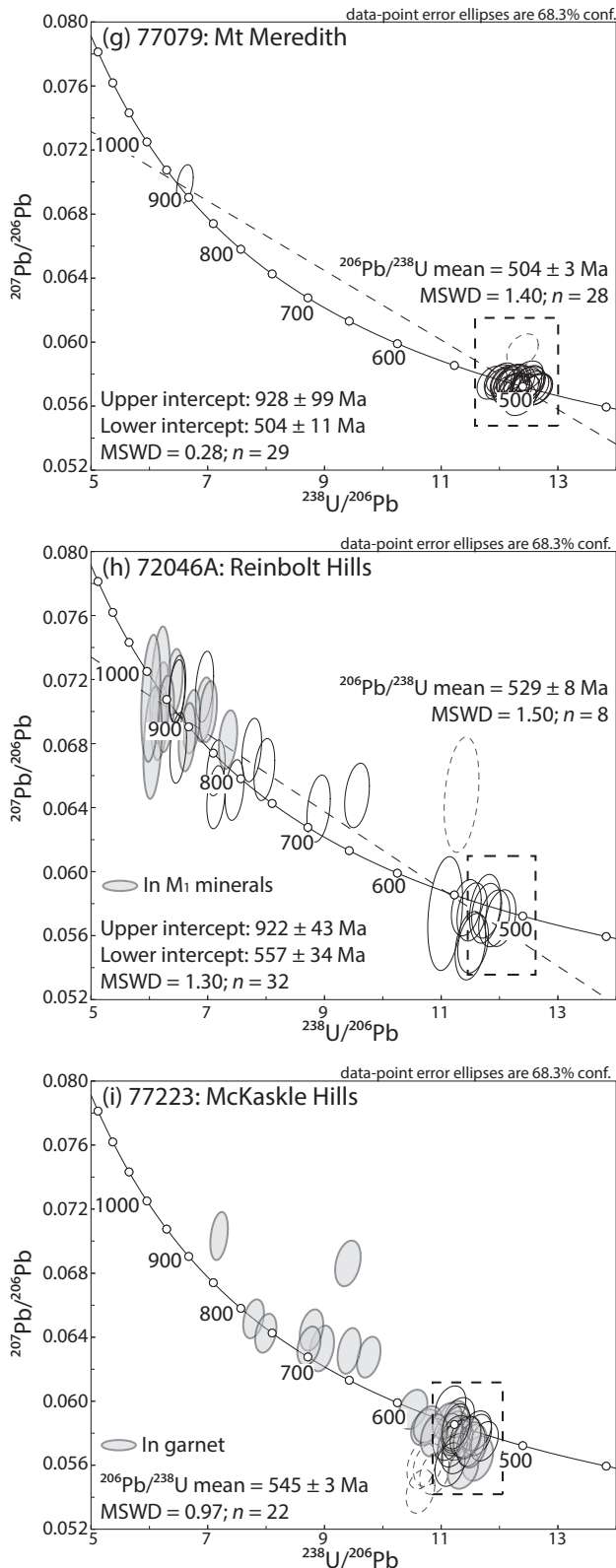
Fig. 9. Continued

East Amery Ice Shelf

72046A: Reinbolt Hills

In sample 72046A, monazite is located within the cordierite–spinel–ilmenite symplectites, along grain boundaries and armoured within porphyroblasts of garnet, sillimanite and K-feldspar. Grains vary from 20 to 100 μm in diameter. The majority of grains are unzoned, although in rare cases they display REE zoning (Fig. 8h). Thirty-three analyses were collected from 18 grains. Monazite grains hosted within coarse-grained M_1 minerals are denoted as filled grey ellipses in Fig. 9h. Analyses define two populations with an array of discordant analyses between them. A Tera–Wasserburg plot of all analyses yields an upper intercept of 922 ± 43 Ma and a lower intercept of 557 ± 34 Ma (Fig. 9h; MSWD = 1·30; $n = 32$). The eight analyses making up the younger population (outlined in the dashed box) yield a $^{206}Pb/^{238}U$ weighted average age of 529 ± 8 Ma (MSWD = 1·50). Grains located within M_1 minerals such as garnet, sillimanite, coarse-grained ilmenite or K-feldspar yield older ages, whereas the cordierite–spinel symplectites commonly yield partially reset or younger ages (Fig. 9h). As the majority of grains were unzoned in REE, it is difficult to link the younger ages to specific compositional variations. However, in rare grains that do show zoning, the younger or reset ages appear to come from zones that are higher in Th (Fig. 8h).

77223: McKaskle Hills

In sample 77223, monazite occurs within the matrix as well as included within garnet. Monazite grains vary in size from small grains (20 μm in diameter) to large grains up to 200 μm in diameter. Some grains show patchy zoning, others have rims that appear brighter in back-scattered electron (BSE) images (Fig. 8i). Forty analyses were collected from 15 grains. Monazite grains hosted within garnet are denoted as filled grey ellipses (Fig. 9i). The analyses fall into two populations (Fig. 9i). Older analyses are discordant and do not define a population, but fall along a poorly defined discordia with an upper intercept of *c.* 900 Ma. Older analyses are from grains included within garnet porphyroblasts, although grains hosted within garnet also yield younger ages (Fig. 9i). The younger population (defined using a linearized probability plot) yields a $^{206}Pb/^{238}U$ weighted average age of 545 ± 3 Ma (MSWD = 0·97; $n = 22$).

MINERAL CHEMISTRY

Representative electron microprobe analyses of all minerals are given in Table 5. The range of compositions of selected minerals is given in Table 6.

Garnet

Garnet grains in samples DP-7, 72046A, PCM-83 and 77223 have X_{alm} values of 0·61–0·67 and X_{py} values of 0·29–0·35. Garnet grains in samples 77079, 77102B and 77079 are more almandine rich, with X_{alm} values of

Table 5: Representative electron microprobe analyses for each mineral

	DP-7: Depot Peak										PCM-83: Else Platform								
	gt rim	gt core	bi	cd	ksp	pl	qz	sill	ilm	sp	gt rim	gt core	bi	cd	ksp	qz	ilm	sp	sill
SiO_2	37·68	38·12	38·22	48·85	64·28	58·82	98·54	36·15	0·15	0·00	37·05	38·34	38·32	48·89	66·48	99·90	0·00	0·01	36·87
TiO_2	0·04	0·05	4·58	0·00	0·04	0·02	0·06	0·02	51·71	0·04	0·02	0·02	3·74	0·00	0·00	0·05	53·05	0·04	0·03
Al_2O_3	21·44	21·46	14·64	32·78	17·28	26·32	0·05	61·14	0·08	58·78	21·33	21·21	16·00	33·05	18·37	0·04	0·00	58·16	62·92
Cr_2O_3	0·02	0·03	0·04	0·00	0·03	0·01	0·00	0·45	0·06	0·49	0·10	0·06	0·20	0·00	0·00	0·01	0·08	0·00	0·09
FeO	31·33	30·53	10·27	6·80	0·15	0·09	0·02	0·21	44·29	30·43	33·43	30·37	11·24	5·51	0·00	0·05	46·76	31·53	0·50
MnO	0·44	0·39	0·02	0·04	0·01	0·01	0·01	0·02	0·14	0·04	0·88	0·75	0·04	0·02	0·00	0·04	0·19	0·05	0·00
MgO	7·49	8·04	17·50	9·78	0·00	0·00	0·03	0·00	1·57	6·56	5·93	7·48	17·42	10·47	0·00	0·02	0·08	6·35	0·02
ZnO	0·01	0·03	0·08	0·07	0·05	0	0·00	0·00	0·01	2·43	0·00	0·00	0·04	0·04	0·00	0·00	0·00	3·02	0·00
CaO	0·99	0·93	0·00	0·00	0·27	7·86	0·01	0·00	0·00	0·01	1·23	1·02	0·00	0·02	0·00	0·02	0·00	0·00	0·00
Na_2O	0·01	0·00	0·18	0·04	2·26	7·25	0·00	0·00	0·03	0·02	0·02	0·02	0·30	0·04	1·69	0·00	0·00	0·12	0·02
K_2O	0·01	0·00	10·39	0·00	14·03	0·10	0·00	0·00	0·00	0·00	0·00	0·00	8·86	0·02	13·69	0·00	0·02	0·01	0·00
Total	99·45	99·57	95·95	98·36	98·40	100·48	98·72	97·99	98·03	98·81	99·99	99·27	96·17	98·06	100·23	100·13	100·18	99·29	100·46
No. oxygens	12	12	11	18	8	8	2	5	3	4	12	12	11	18	8	2	3	4	5
Si	2·96	2·98	2·75	4·99	3·01	2·62	1·00	1·00	0·00	0·00	2·93	3·02	2·75	4·98	3·03	1·00	0·00	0·00	0·99
Ti	0·00	0·00	0·25	0·00	0·00	0·00	0·00	0·00	0·95	0·00	0·00	0·00	0·20	0·00	0·00	0·00	1·01	0·00	0·00
Al	1·99	1·98	1·24	3·95	0·95	1·38	0·00	1·99	0·00	1·95	1·99	1·97	1·35	3·97	0·99	0·00	0·00	1·91	1·99
Cr	0·00	0·00	0·00	0·00	0·00	0·00	0·00	0·01	0·00	0·01	0·01	0·00	0·01	0·00	0·00	0·00	0·00	0·00	0·00
Fe^{3+}	0·08	0·05	—	—	0·01	—	—	0·01	0·10	0·03	0·15	0·00	—	—	—	—	0·00	0·09	0·02
Fe^{2+}	1·97	1·95	0·62	0·58	0·00	0·00	0·00	0·00	0·89	0·69	2·06	2·00	0·67	0·47	0·00	0·00	0·99	0·65	0·00
Mn^{2+}	0·03	0·03	0·00	0·00	0·00	0·00	0·00	0·00	0·00	0·00	0·06	0·05	0·00	0·00	0·00	0·00	0·00	0·00	0·00
Mg	0·88	0·94	1·87	1·49	0·00	0·00	0·00	0·00	0·06	0·27	0·70	0·88	1·86	1·59	0·00	0·00	0·00	0·26	0·00
Zn	0·00	0·00	0·00	0·01	0·01	0·00	0·00	0·00	0·00	0·05	0·00	0·00	0·00	0·00	0·00	0·00	0·00	0·06	0·00
Ca	0·08	0·08	0·00	0·00	0·01	0·38	0·00	0·00	0·00	0·00	0·10	0·09	0·04	0·00	0·00	0·00	0·00	0·00	0·00
Na	0·00	0·00	0·03	0·01	0·21	0·63	0·00	0·00	0·00	0·00	0·00	0·00	0·04	0·01	0·15	0·00	0·00	0·01	0·00
K	0·00	0·00	0·95	0·00	0·84	0·01	0·00	0·00	0·00	0·00	0·00	0·00	0·81	0·00	0·79	0·00	0·00	0·00	0·00
Total cations (S)	8·00	8·00	7·71	11·03	5·03	5·01	1·00	3·00	2·00	3·00	8·00	8·00	7·71	11·02	4·95	1·00	2·00	2·99	3·01

(Continued)

Table 5: Continued

	77090: Taylor Platform						77102B: Brocklehurst Ridge									77079: Mt Meredith				
	gt	bi	cd	qz	sill	ilm	gt rim	gt core	bi	cd	ksp	pl	qz	sill	ilm	gt rim	gt core	bi	pl	qz
SiO_2	36.95	33.72	46.57	98.95	35.82	0.03	37.36	37.27	34.88	47.63	64.55	63.22	99.82	36.18	0.06	36.01	35.15	34.12	60.16	98.55
TiO_2	0.01	3.37	0.02	0.02	0.01	52.90	0.00	0.01	3.25	0.02	0.03	0.00	0.01	0.00	52.71	0.00	0.00	2.80	0.01	0.00
Al_2O_3	21.14	17.50	30.88	0.02	60.77	0.25	21.42	21.27	18.68	31.97	18.89	23.04	0.02	62.22	0.01	20.65	20.36	19.01	23.23	0.01
Cr_2O_3	0.06	0.28	0.03	0.04	0.04	0.09	0.07	0.03	0.09	0.01	0.00	0.05	0.00	0.03	0.09	0.01	0.02	0.00	0.05	0.00
FeO	35.54	20.23	9.56	0.01	0.23	45.14	37.13	36.69	20.82	9.18	0.08	0.03	0.28	0.26	46.72	37.48	37.03	23.47	0.07	0.01
MnO	1.53	0.00	0.13	0.00	0.01	0.38	0.53	0.42	0.03	0.02	0.00	0.00	0.00	0.00	0.08	2.05	1.51	0.06	0.01	0.00
MgO	3.28	7.61	7.15	0.00	0.01	0.12	2.73	3.58	7.91	7.56	0.01	0.00	0.00	0.00	0.15	1.83	2.81	5.94	0.00	0.00
ZnO	0.14	0.10	0.00	0.05	0.04	0.15	0.00	0.02	0.06	0.05	0.00	0.01	0.00	0.00	0.00	0.06	0.02	0.09	0.02	0.00
CaO	0.96	0.00	0.01	0.00	0.00	0.01	0.75	0.90	0.00	0.00	0.01	3.83	0.00	0.00	0.00	0.93	1.05	0.02	5.63	0.00
Na_2O	0.02	0.17	0.14	0.02	0.00	0.02	0.00	0.00	0.12	0.15	2.04	9.38	0.00	0.01	0.00	0.02	0.02	0.37	8.29	0.00
K_2O	0.01	9.31	0.00	0.01	0.01	0.00	0.00	0.00	9.11	0.01	12.87	0.08	0.00	0.00	0.00	0.01	0.00	9.06	0.06	0.00
Total	99.64	92.29	94.51	99.11	96.94	99.08	99.98	100.19	94.95	96.60	98.47	99.65	100.13	98.70	99.82	99.04	97.99	94.94	97.53	98.57
No. oxygens	12	11	18	2	5	3	12	12	11	18	8	8	2	5	3	12	12	11	8	2
Si	2.99	2.68	5.03	1.00	1.00	0.00	3.02	2.99	2.68	5.01	2.99	2.80	1.00	0.99	0.00	2.98	2.95	2.67	2.73	1.00
Ti	0.00	0.20	0.00	0.00	0.00	1.01	0.00	0.00	0.19	0.00	0.00	0.00	0.00	0.00	1.00	0.00	0.00	0.17	0.00	0.00
Al	2.01	1.64	3.93	0.00	1.99	0.01	2.04	2.01	1.69	3.97	1.03	1.20	0.00	2.00	0.00	2.01	2.01	1.75	1.25	0.00
Cr	0.00	0.02	0.00	0.00	0.00	0.00	0.00	0.00	0.01	0.00	0.00	0.00	0.00	0.00	0.00	0.00	0.00	0.00	0.00	0.00
Fe^{3+}	0.02	—	—	—	0.01	0.00	0.00	0.01	—	—	—	—	—	0.02	0.00	0.04	0.07	—	—	—
Fe^{2+}	2.39	1.35	0.86	0.00	0.00	0.96	2.51	2.46	1.34	0.81	0.00	0.00	0.00	0.00	0.99	2.52	2.53	1.53	0.00	0.00
Mn^{2+}	0.11	0.00	0.01	0.00	0.00	0.01	0.04	0.03	0.00	0.00	0.00	0.00	0.00	0.00	0.00	0.14	0.11	0.00	0.00	0.00
Mg	0.40	0.90	1.15	0.00	0.00	0.00	0.33	0.43	0.91	1.19	0.00	0.00	0.00	0.00	0.01	0.23	0.35	0.69	0.00	0.00
Zn	0.01	0.01	0.00	0.00	0.00	0.00	0.00	0.00	0.00	0.00	0.00	0.00	0.00	0.00	0.00	0.00	0.00	0.01	0.00	0.00
Ca	0.08	0.00	0.00	0.00	0.00	0.00	0.07	0.08	0.02	0.00	0.00	0.18	0.00	0.00	0.00	0.08	0.09	0.00	0.27	0.00
Na	0.00	0.03	0.03	0.00	0.00	0.00	0.00	0.00	0.02	0.03	0.18	0.81	0.00	0.00	0.00	0.00	0.00	0.06	0.73	0.00
K	0.00	0.94	0.00	0.00	0.00	0.00	0.00	0.00	0.89	0.00	0.76	0.00	0.00	0.00	0.00	0.00	0.00	0.90	0.00	0.00
Total cations (S)	8.00	7.77	11.02	1.00	3.00	2.00	8.00	8.00	7.73	11.02	4.97	5.00	1.00	3.00	2.00	8.00	8.00	7.78	4.98	1.00

(Continued)

Table 5: Continued

	72046A: Reinbolt Hills										77223: McKaskle Hills								
	gt rim	gt core	bi	cd	ksp	pl	qz	sill	ilm	sp	gt rim	gt core	bi	cd	ksp	pl	ru	qz	ilm
SiO_2	38.41	38.58	38.15	48.92	64.77	61.56	99.90	36.87	0.06	0.02	36.88	2.97	35.12	48.77	64.20	57.96	0.00	98.28	0.00
TiO_2	0.00	0.02	5.81	0.00	0.05	0.00	0.05	0.03	50.90	0.04	0.08	0.00	4.67	0.00	0.06	0.01	100.87	0.06	54.24
Al_2O_3	21.82	21.84	14.76	32.55	18.77	24.49	0.04	62.92	0.00	58.69	20.99	1.97	14.88	33.57	18.84	25.95	0.06	0.02	0.03
Cr_2O_3	0.10	0.01	0.06	0.00	0.01	0.03	0.01	0.09	0.10	0.31	0.05	0.00	0.05	0.00	0.00	0.00	0.13	0.05	0.05
FeO	30.41	28.95	9.87	5.93	0.00	0.18	0.05	0.50	45.67	31.06	30.33	1.94	13.92	5.02	0.13	0.02	0.05	0.17	42.76
MnO	0.81	0.73	0.01	0.09	0.00	0.06	0.04	0.00	0.19	0.09	0.84	0.04	0.02	0.01	0.00	0.00	0.02	0.07	0.19
MgO	8.25	8.97	17.44	9.99	0.00	0.00	0.02	0.02	1.36	7.79	7.19	0.94	13.60	10.96	0.00	0.01	0.01	0.02	1.24
ZnO	0.06	0.07	0.08	0.19	0.03	0.00	0.00	0.00	0.20	1.38	0.12	0.00	0.08	0.00	0.03	0.01	0.00	0.05	0.12
CaO	0.94	0.90	0.00	0.00	0.18	5.85	0.02	0.00	0.02	0.01	1.24	0.13	0.02	0.00	0.03	7.37	0.00	0.03	0.01
Na_2O	0.00	0.00	0.26	0.14	2.51	8.17	0.00	0.02	0.05	0.09	0.00	0.00	0.07	0.01	1.33	7.78	0.00	0.00	0.00
K_2O	0.04	0.00	9.61	0.06	12.84	0.15	0.00	0.00	0.01	0.00	0.00	0.00	8.84	0.00	14.05	0.12	0.00	0.00	0.02
Total	100.86	100.07	96.04	97.88	99.17	100.49	100.13	100.46	98.56	99.48	97.72	8.00	91.27	98.34	98.65	99.23	101.15	98.78	98.66
No. oxygens	12	12	11	18	8	8	2	5	3	4	12	12	11	18	8	8	2	2	3
Si	2.99	2.98	2.76	5.01	2.98	2.72	1.00	0.99	0.00	0.00	2.95	2.97	2.72	4.95	3.00	2.61	0.00	1.00	0.00
Ti	0.00	0.00	0.32	0.00	0.00	0.00	0.00	0.00	0.97	0.00	0.00	0.00	0.27	0.00	0.00	0.00	0.99	0.00	1.02
Al	1.99	1.99	1.26	3.93	1.02	1.28	0.00	1.99	0.00	1.91	1.98	1.97	1.36	4.01	1.04	1.38	0.00	0.00	0.00
Cr	0.01	0.00	0.00	0.00	0.00	0.00	0.00	0.00	0.00	0.01	0.00	0.00	0.00	0.00	0.00	0.00	0.00	0.00	0.00
Fe^{3+}	0.02	0.05	—	—	—	—	—	—	0.07	0.08	0.10	0.06	0.03	—	—	—	—	—	0.01
Fe^{2+}	1.91	1.82	0.60	0.51	0.00	0.01	0.00	0.02	0.90	0.64	1.93	1.88	0.90	0.43	0.00	0.00	0.00	0.00	0.89
Mn^{2+}	0.05	0.05	0.00	0.01	0.00	0.00	0.00	0.00	0.00	0.00	0.06	0.04	0.00	0.00	0.00	0.00	0.00	0.00	0.00
Mg	0.91	1.03	1.88	1.53	0.00	0.00	0.00	0.00	0.05	0.32	0.86	0.94	1.57	1.66	0.00	0.00	0.00	0.00	0.05
Zn	0.00	0.00	0.00	0.01	0.00	0.00	0.00	0.00	0.00	0.03	0.01	0.00	0.00	0.00	0.00	0.00	0.00	0.00	0.00
Ca	0.12	0.07	0.00	0.00	0.01	0.28	0.00	0.00	0.00	0.00	0.11	0.00	0.00	0.00	0.01	0.36	0.00	0.00	0.00
Na	0.00	0.00	0.04	0.03	0.22	0.70	0.00	0.00	0.00	0.00	0.00	0.00	0.01	0.00	0.00	0.68	0.00	0.00	0.00
K	0.00	0.00	0.89	0.01	0.75	0.01	0.00	0.00	0.00	0.00	0.00	0.00	0.87	0.00	0.84	0.01	0.00	0.00	0.00
Total cations (S)	8.00	8.00	7.75	11.04	4.99	4.99	1.00	3.01	1.99	3.00	8.00	7.99	7.75	11.04	5.00	5.04	0.99	1.00	1.98

Table 6: Range of values for mineral chemistry of selected minerals

	DP-7	PCM-83	77090	77102B	77079	72046A	77223
Garnet core							
X_{alm}	0·65–0·67	0·64–0·65	0·80–0·82	0·82–0·83	0·82–0·83	0·62–0·63	0·61–0·65
X_{py}	0·29–0·32	0·30–0·32	0·14	0·10–0·11	0·10–0·11	0·33–0·34	0·34–0·35
X_{grs}	0·025–0·028	0·029–0·030	0·023–0·030	0·027–0·030	0·026–0·030	0·023–0·026	0·022–0·030
X_{sps}	0·008–0·010	0·015	0·033–0·039	0·034–0·036	0·034–0·036	0·013–0·020	0·011–0·018
X_{Fe}	0·67–0·70	0·67–0·68	0·80–0·82				
Garnet rim							
X_{alm}	Unzoned	0·66–0·71	Unzoned	0·85–0·86	0·85	0·64–0·65	0·68–0·69
X_{py}	Unzoned	0·26–0·29	0·11	0·07–0·08	0·07	0·29–0·31	0·26–0·28
X_{grs}	Unzoned	0·035–0·037	Unzoned	Unzoned	Unzoned	0·032–0·040	Unzoned
X_{sps}	Unzoned	0·017–0·019	Unzoned	0·045–0·047	0·046–0·047	Unzoned	0·017–0·022
Biotite							
Ti c.p.f.u.	0·24–0·27	0·09–0·23	0·14–0·20	0·18–0·22	0·14–0·20	0·27–0·33	0·22–0·31
X_{Fe}	0·25	0·22–0·28	0·57–0·62	0·58–0·62	0·68–0·70	0·20–0·30	0·34–0·38
Cordierite							
X_{Fe}	0·20–0·28	0·23–0·26	0·41–0·44	0·40–0·42	—	0·20–0·25	0·17–0·23
K-feldspar							
X_{Or}	0·67–0·82	0·78–0·84	—	0·81–0·90	—	0·76–0·82	0·89
Plagioclase							
X_{Ab}	0·47–0·58	—	—	0·82	0·72–0·74	0·69–0·77	0·59–0·74
Spinel							
Cr c.p.f.u.	0·01	0–0·03	—	—	—	0–0·01	—
Zn c.p.f.u.	0·05	0·06–0·08	—	—	—	0·03	—
Ilmenite							
Ti c.p.f.u.	0·99–1·00	0·99–1·02	1·01–1·04	1·00–0·01		0·97–0·98	1·01–1·02
Mn c.p.f.u.	0·002–0·003	0·002–0·007	0·008–0·012	0·002–0·004		0·004–0·006	0·004–0·006

$X_{alm} = Fe/(Fe + Mg + Ca + Mn)$; $X_{py} = Mg/(Fe + Mg + Ca + Mn)$; $X_{grs} = Ca/(Fe + Mg + Ca + Mn)$; $X_{sps} = Mn/(Fe + Mg + Ca + Mn)$; $X_{Fe} = Fe/(Fe + Mg)$; $X_{or} = K/(K + Na + Ca)$; $X_{ab} = Na/(Na+Ca)$. c.p.f.u., cations per formula unit.

0·80–0·83 and X_{py} values of 0·10–0·14. All samples have X_{grs} values between 0·02 and 0·03 and X_{sps} values between 0·01 and 0·04. Garnet grains in sample DP-7 and 77090 are unzoned in X_{alm}; the other samples show an increase in X_{alm} from core to rim. Sample DP-7 is unzoned in X_{py}; the other samples show a decrease in X_{py} from core to rim. Samples 72046A and PCM-83 display X_{grs} zoning, with an increase from core to rim; the other samples are unzoned in X_{grs}. Samples PCM-83, 77102B, 77079 and 77223 show minor increases in X_{sps} from core to rim, whereas the other samples are unzoned in X_{sps}.

Biotite
The TiO_2 content of biotite in all samples varies from 0·09 to 0·33 cations p.f.u., with most analyses falling between 0·15 and 0·27 cations p.f.u. Biotite in samples DP-7, PCM-83 and 72046A has X_{Fe} of 0·20–0·30; samples 77090 and 77102B have X_{Fe} of 0·57–0·62; sample 77079 has X_{Fe} of 0·68–0·70; and sample 77223 has X_{Fe} of 0·34–0·38.

Spinel
Spinel in samples DP-7, 72046A and PCM-83 contains 0·03–0·08 Zn cations p.f.u. and 0–0·03 Cr cations p.f.u.

Cordierite
Samples DP-7, PCM-83, 72046A and 77223 have similar X_{Fe} of 0·17–0·28, whereas samples 77090 and 77102B have higher X_{Fe} of 0·40–0·44.

Ilmenite
Ilmenite in all samples has Ti values between 0·97 and 1·04 cations p.f.u. and Mn values between 0·002 and 0·012 cations p.f.u.

Feldspars
Samples DP-7, 77102B, 77079, 72046A and 77223 contain plagioclase. Sample DP-7 has a lower X_{Ab} range of 0·47–0·58, whereas samples 77079, 72046A and 77223 have X_{Ab} values falling between 0·59 and 0·77. Sample 77102B has high X_{Ab} of 0·82. Samples DP-7, PCM-83 and 72046A have X_{or} values of 0·67–0·84 whereas samples 77102B and 77223 have higher X_{or} values of 0·81–0·90.

PSEUDOSECTIONS
T–M and *P–T* pseudosections
P–T pseudosections were calculated for metapelitic samples from each of the locations used for geochronology. The fields containing the assemblages of interest for each sample are outlined in bold (Fig. 10). In at least some samples, the mineral reactions probably developed during two high-grade events (Fig. 9). Therefore, mineral assemblages are described in terms of M_1 and M_2 relationships (Table 3).

The samples containing mineral reaction microstructures (DP-7, PCM-83, 72046A and 77223) contain low amounts of H_2O and have an elevated solidus, consistent with melt loss. Therefore, $T–M_{melt}$ sections were calculated for each of the samples to investigate the effect of melt on the system (Supplementary Data Appendix S2).
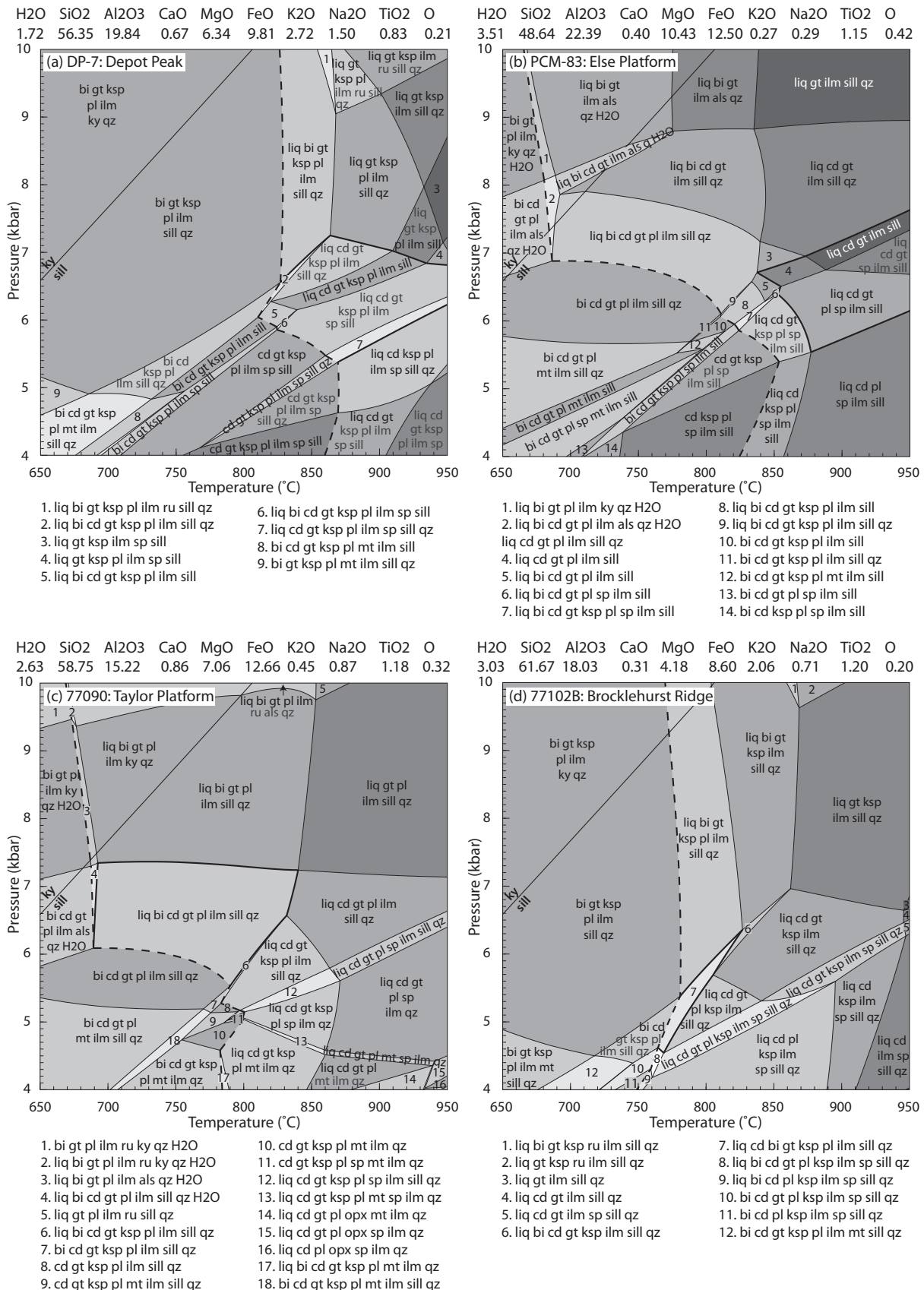
Fig. 10. Calculated *P–T* pseudosections using THERMOCALC. The bulk-rock composition is given above each pseudosection. The bold dashed line in each pseudosection is the solidus and fields outlined in bold are the fields of interest. (a) Sample DP-7; (b) sample PCM-83; (c) sample 77090; (d) sample 77102B; (e) sample 77079; (f) sample 72046A; (g) sample 77223; (h) interpreted peak fields for all samples overlain.

H2O	SiO2	Al2O3	CaO	MgO	FeO	K2O	Na2O	TiO2	O
7.25	50.48	10.01	2.10	5.94	19.58	2.72	0.31	1.31	0.30

(e) 77079: Mt Meredith
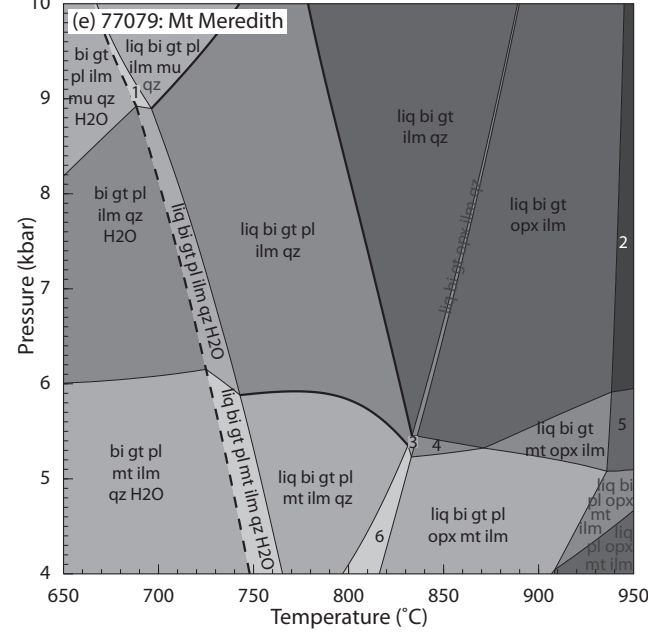
1. liq bi gt pl ilm mu qz H2O
2. liq gt opx ilm
3. liq bi gt pl opx ilm qz
4. liq bi gt opx mt ilm qz
5. liq gt mt opx ilm
6. liq bi gt pl opx mt ilm qz

H2O	SiO2	Al2O3	CaO	MgO	FeO	K2O	Na2O	TiO2	O
2.31	48.48	27.00	0.59	8.15	10.48	0.54	0.51	1.59	0.33

(f) 72046A: Reinbolt Hills
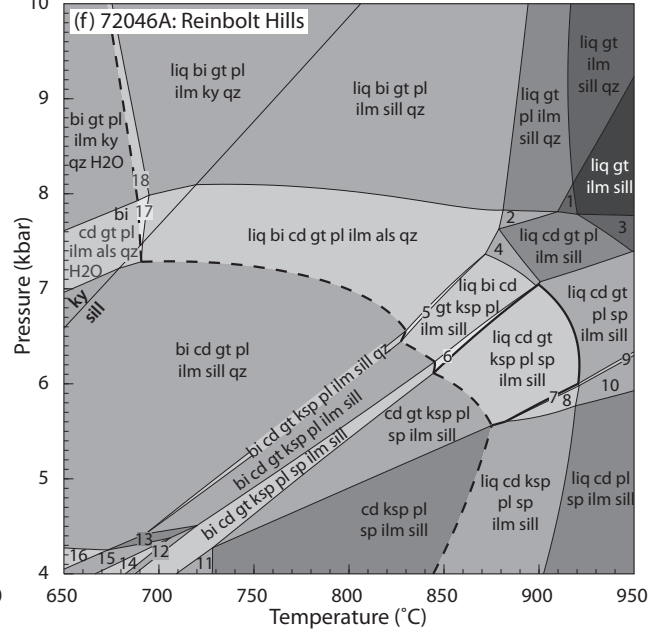
1. liq gt pl ilm sill
2. liq cd gt pl ilm sill qz
3. liq cd gt ilm sill
4. liq bi cd gt pl ilm sill
5. liq bi cd gt ksp pl ilm sill qz
6. liq bi cd gt ksp pl sp ilm sill
7. liq cd gt ksp pl sp ilm sill qz
8. liq cd ksp pl sp ilm sill qz
9. liq cd gt pl sp ilm sill qz
10. liq cd pl sp ilm sill qz
11. bi cd ksp pl sp ilm sill
12. bi cd gt pl sp ilm sill
13. bi cd gt pl ilm sill
14. bi cd gt pl mt sp ilm sill
15. bi cd gt pl mt ilm sill
16. bi cd gt pl ilm sill
17. liq bi cd gt pl ilm als qz H2O
18. liq bi gt pl ilm ky qz H2O

H2O	SiO2	Al2O3	CaO	MgO	FeO	K2O	Na2O	TiO2	O
3.16	61.02	10.85	1.18	9.06	10.92	1.08	0.92	1.61	0.21

(g) 77223: McKaskle Hills
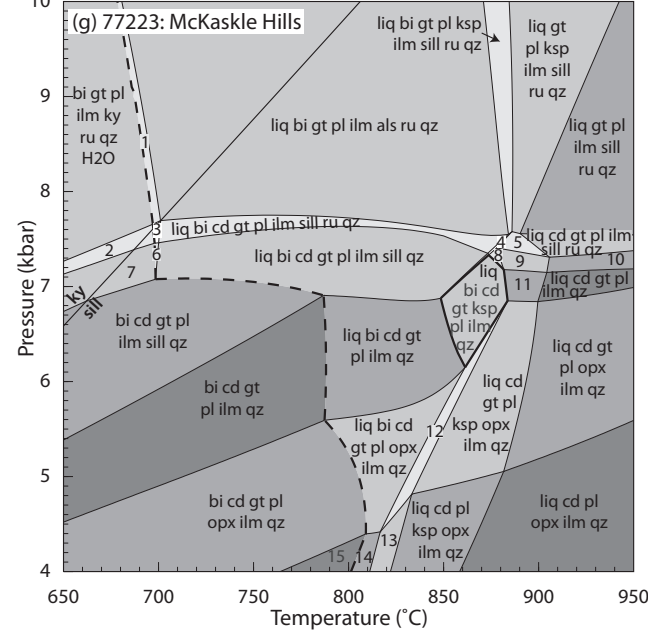
1. liq bi gt pl ilm ky ru qz H2O
2. bi cd gt pl ilm sill ru qz H2O
3. liq bi cd gt pl ilm sill ru qz H2O
4. liq bi cd gt pl ksp ilm sill ru qz
5. liq cd gt pl ksp ilm sill ru qz
6. liq bi cd gt pl ilm sill qz H2O
7. bi cd gt pl ilm sill qz H2O
8. liq bi cd gt pl ksp ilm ru qz
9. liq cd gt pl ksp ilm ru qz
10. liq cd gt pl ilm ru qz
11. liq cd gt pl ksp ilm qz
12. liq bi cd gt pl ksp opx ilm qz
13. liq bi cd pl ksp opx ilm qz
14. liq bi cd pl opx ilm qz
15. bi gt pl opx ilm qz

(h) Pseudosections overlain

ky
sill
100 °C/kbar
77090
77079
77223
72046A
PCM-83
DP-1
125 °C/kbar
71102(?)
150 °C/kbar

— nPCM
— EAIS
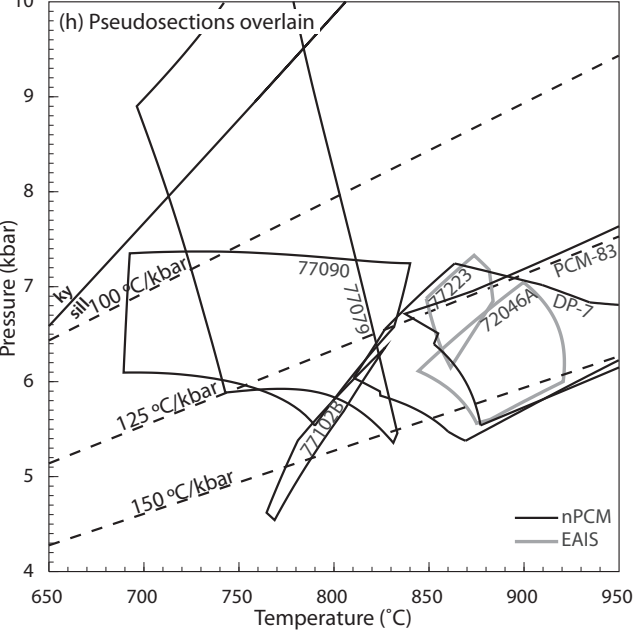
Fig. 10. Continued

The T–M_{melt} sections vary from the anhydrous compos-
ition of each sample at $M_{melt} = 0$ to $M_{melt} = 0.5$ (50 mol %
added melt). These samples have similar mineral rela-
tionships so the T–M_{melt} sections show similar phase re-
lationships. The effect of adding increasing amounts of
melt to the system is to contract the spinel-bearing fields
to higher temperatures in the spinel-bearing samples
and to lower the temperature of the solidus in all four
samples until it becomes water saturated at 660–680°C
(Supplementary Data Appendix S2). The P–T pseudosec-
tions for these samples (described below) were calcu-
lated with 7 mol % melt reintegrated into the
composition, shown in the T–M_{melt} sections as a bold
vertical line. This corresponds to the likely maximum
amount of melt in the system at any point, after which
melt extraction occurs (e.g. Rosenberg & Handy, 2005;
Brown, 2010; Yakymchuk et al., 2013).

INTERPRETATION OF MINERAL REACTION
MICROSTRUCTURES

Samples DP-7, PCM-83 and 72046A preserve localized
mineral reaction microstructures that are characterized
by the partial replacement of garnet–sillimanite-bearing
assemblages by cordierite–spinel-bearing assemblages
(Table 3). Similarly, sample 77223 preserves a garnet-
bearing assemblage that is partially replaced by
cordierite–quartz and plagioclase–quartz symplectites
(Table 3). Reaction microstructures such as these could
be interpreted in several ways. One interpretation is
that the microstructures reflect an arrested attempt of
the rock to produce a new equilibrium assemblage,
with the partially replaced minerals comprising disequi-
librium relics (Kelsey & Hand, 2015). An alternative in-
terpretation is that the newly formed minerals were in
effective equilibrium with the relict minerals, producing
a composite mineral assemblage in which the modal
proportion of the reactants was simply reduced (Kelsey
& Hand, 2015). We favour the latter interpretation for
the following reason. The phase equilibria modelling
for samples DP-7, PCM-83, 72046A and 77223 (Fig. 10)
shows that replacement of one mineral assemblage by
another generally occurs via a series of assemblages
that record the progressive decrease in the modal pro-
portion of reactants and the increase in proportion of
new minerals. However, implicit in this process is that
at each stage, an equilibrium assemblage will exist that
comprises a mix of the residual (M₁) assemblage and
the newly formed (M₂) minerals. Furthermore, if the re-
action microstructures in samples DP-7, PCM-83,
72046A and 77223 represent an arrested attempt to
completely replace the M₁ assemblage by the assem-
blage solely within the symplectites, there should be a
calculated phase assemblage field that comprises only
the minerals of the symplectites. This is not the case for
any of the samples, suggesting that the symplectite as-
semblages must form part of an assemblage that also
includes one or more of the M₁ reactant minerals.

Northern Prince Charles Mountains
DP-7: Depot Peak
Sample DP-7 is likely to have contained an M₁ garnet +
sillimanite + biotite + K-feldspar + spinel + ilmenite + quartz
assemblage, probably with silicate melt. This was over-
printed by a structurally late cordierite–spinel–ilmenite-
bearing assemblage. The presence of optically
continuous biotite inclusions in the cordierite suggests
that biotite was present as an M₁ mineral, but has been
replaced and the remaining biotite is relict. The former
presence of biotite is also suggested by the growth of il-
menite, which requires a source of Ti. Quartz and
plagioclase both form fine-grained intergrowths and
are interpreted to be part of the M₂ assemblage. We in-
terpret the abundance of garnet and sillimanite in the
sample, and the lack of compositional zoning in the gar-
net, to mean that garnet and sillimanite form part of the
M₁ as well as the M₂ assemblages. In outcrop, the pres-
ence of thin veins of structurally late, Cambrian-age gar-
net–cordierite-bearing pegmatite also implies that melt
was present. We therefore interpret the M₂ mineral as-
semblage in sample DP-7 to be garnet + sillimanite +
K-feldspar + cordierite + spinel + ilmenite + plagioclase +
quartz + silicate melt.

   The coexistence of spinel and melt means that the
minimum temperature is 825°C (Fig. 10a). However, spi-
nel in this sample contains small amounts of Zn and Cr
(Table 6), which are not included in the a–x models for
spinel but are known to increase spinel stability to lower
temperatures and higher pressures (e.g. Nichols et al.,
1992; Tajćmanová et al., 2009). Instead, the absence of
biotite and presence of quartz can be used to constrain
temperatures to between 820 and 910°C and the pres-
ence of cordierite and garnet to constrain pressures to
be between 5.4 and 7.2 kbar (Fig. 10a).

PCM-83: Else Platform
Sample PCM-83 is interpreted to have contained an
M₁ garnet + sillimanite + biotite + K-feldspar + spinel +
ilmenite + quartz assemblage, probably with silicate
melt. This has been overprinted by a structurally late M₂
assemblage that involved the formation of cordierite,
spinel and ilmenite at the expense of biotite, garnet and
sillimanite. There now is a paucity of biotite in the sam-
ple. However, its former presence is suggested by small
relict grains and the abundance of ilmenite in the cor-
dierite–spinel-bearing symplectites, which requires the
breakdown of a Ti-bearing mineral. The paucity of bio-
tite suggests that it may have been the limiting reactant.
The presence of silicate melt is inferred based on the
presence of Cambrian-age felsic dykes and pegmatites
(Manton et al., 1992; Hand et al., 1994b). Additionally,
the lack of newly formed K-feldspar in the M₂ assem-
blage, despite the implied breakdown of biotite, sug-
gests that melt was likely to have been produced and
subsequently lost. Plagioclase is modelled to occur
throughout a wide region of P–T space but does not
occur in this sample. Electron microprobe analyses and

X-ray mapping show that sodium is present in cordierite, spinel and biotite (Tables 4 and 5; Fig. 6h), but it is not incorporated in the current *a–x* models for these phases. The minor amounts of sodium in the domain composition result in the over-prediction of plagioclase stability in the sample. Therefore, the absence of plagioclase is not used as a pressure constraint for this sample (Fig. 10b).

The presence of coexisting spinel and silicate melt and the absence of K-feldspar in the reaction domains suggest that temperatures are above 850°C (Fig. 10b). This assemblage does not provide an upper temperature constraint. However, as above, spinel in this sample contains small amounts of Zn and Cr, which may expand the spinel stability field to lower temperatures and higher pressures. Therefore, the fields that best represent the stable mineral assemblage are defined by the absence of biotite and K-feldspar and the presence of garnet; these occur above 820°C and between 5·4 and 7·3 kbar (Fig. 10b).

77090: Taylor Platform
The assemblage in sample 77090 is interpreted to have consisted of garnet + sillimanite + cordierite + biotite + ilmenite + quartz + silicate melt. Plagioclase does not occur in this sample, but is present in modally small amounts in the pseudosection. This may be due to the large volume of cordierite in this sample, which contains minor amounts of sodium (as above; Table 5). The presence of cordierite suggests pressures of less than 7·3 kbar (Fig. 10c). The solidus provides a lower temperature constraint of 690°C at pressures above 6 kbar (Fig. 10c). Biotite is interpreted to form part of the assemblage, but the paucity of biotite suggests that temperatures were near the biotite-out boundary at 830–840°C (Fig. 10c).

77102B: Brocklehurst Ridge
The assemblage in sample 77102B is interpreted to have consisted of garnet + sillimanite + cordierite + biotite + K-feldspar + ilmenite + quartz + silicate melt. Plagioclase is rare, but does occur in the quartzofeldspathic regions of the rock, and is therefore also interpreted to form part of the peak assemblage. The coexisting presence of cordierite and biotite constrains peak conditions to a narrow field at 765–825°C and 4·6–6·3 kbar (Fig. 10d).

77079: Mt Meredith
The assemblage in sample 77079 is interpreted to have consisted of garnet + biotite + plagioclase + ilmenite + quartz + silicate melt. This assemblage is stable over a wide range of conditions (Fig. 10e). However, the absence of magnetite provides a lower pressure constraint of 5·4 kbar, whereas the presence of plagioclase provides an upper temperature constraint of 835°C. The wet solidus provides a lower temperature constraint of 700°C. Therefore, the assemblage is stable over a temperature range of 700–835°C and pressures of 5·4–10 kbar (Fig. 10e).

East Amery Ice Shelf
72046A: Reinbolt Hills
Sample 72046A was likely to have contained an M_1 garnet + sillimanite + biotite + spinel + ilmenite + quartz assemblage, probably with silicate melt. The M_2 assemblage is structurally late and contains cordierite–spinel–ilmenite–plagioclase–K-feldspar-bearing domains that developed within the garnet–sillimanite-dominated part of the rock. The abundance of garnet and sillimanite in the sample is interpreted to reflect that they form part of the M_2 assemblage, but in reduced abundance relative to the M_1 assemblage. Therefore, we interpret the M_2 assemblage to comprise garnet + sillimanite + cordierite + spinel + ilmenite + K-feldspar + plagioclase. The additional presence of silicate melt in the M_2 assemblage is inferred based on the presence of Cambrian-age aluminous pegmatite in the Reinbolt Hills (Ziemann *et al.*, 2005). For the modelled domain composition, the M_2 assemblage in sample 72046A is stable at 845–920°C and 5·5–7 kbar (Fig. 10f).

77223: McKaskle Hills
The M_1 assemblage for the McKaskle Hills is interpreted to be garnet + sillimanite + biotite + K-feldspar + ilmenite + rutile + plagioclase + quartz + silicate melt. The presence of sillimanite, rutile and biotite within garnet suggests that these minerals were part of an earlier stable assemblage. Rutile commonly occurs in the plagioclase–quartz-rich parts of the sample, suggesting that they also formed part of the assemblage. Rutile is stable above pressures of 7·2 kbar and temperatures of 810°C (Fig. 10g). However, as the domain composition is appropriate for modelling only the M_2 assemblage, the conditions of the M_1, probably higher-pressure rutile-bearing assemblage cannot be adequately determined.

The M_2 assemblage is interpreted to involve garnet + cordierite + biotite + K-feldspar + ilmenite + plagioclase + quartz + silicate melt. Cordierite–quartz symplectites occur as double coronas on garnet grains, and quartz–plagioclase coronas commonly occur associated with K-feldspar. The symplectites occur in areas that are rich in biotite (Fig. 4f). Rutile is uncommon in these areas; instead, biotite and ilmenite are the Ti-bearing minerals. Garnet grains preserve very minor X_{sps} zoning, suggesting that despite the apparent replacement of garnet by the symplectites, a large part of the garnet grain was part of the equilibration volume. The M_2 assemblage occurs between 6·1 and 7·3 kbar and at temperatures of 850–880°C.

DISCUSSION
Geochronology
All metapelitic samples preserve geochronological evidence for two episodes of metamorphism; an older

population of monazite reflecting growth during the *c.* 1000–900 Ma Rayner Orogeny and another recording Cambrian-age reworking. The expression of the over-print as recorded by monazite growth is variable be-tween samples. Samples from Depot Peak, Else Platform and the Reinbolt Hills (samples DP-7, PCM-83 and 72046A) each have poorly defined Rayner-age populations at *c.* 920 Ma, with a large number of ana-lyses falling along a chord to a smaller concordant population at *c.* 530 Ma (Fig. 9c, d and h). Samples from Taylor Platform, Brocklehurst Ridge, Mount Meredith and the McKaskle Hills (samples 77090, 77012B, 77079 and 77223) have dominantly Cambrian-age popula-tions, with minor inheritance and/or discordance sug-gesting that the samples also experienced a Rayner-age event (Fig. 9e–g and i). The syn- and post-deformational pegmatite veins from Depot Peak (samples DP-1 and DP-11) are both Cambrian in age (Fig. 9a and b).

Interpreting monazite ages and linking them to the *P–T* evolution or development of a tectonic fabric can be difficult (e.g. Foster & Parrish, 2003; Vance *et al.*, 2003; Morrissey *et al.*, 2011; Gasser *et al.*, 2012; Cubley *et al.*, 2013; Gervais & Hynes, 2013). Monazite can be unreactive in the absence of fluids or melts and its clos-ure temperature can exceed 900°C (Cherniak *et al.*, 2004; Cherniak, 2010). Natural studies on high-tempera-ture and ultrahigh-temperature granulite-facies rocks seem to lend support to the preservation of growth ages or inheritance even at very high temperatures (e.g. Kelsey *et al.*, 2003*a*, 2007; Schmitz & Bowring, 2003; Goncalves *et al.*, 2004; Sajeev *et al.*, 2010; Clark *et al.*, 2011; Cutts *et al.*, 2013; Walsh *et al.*, 2015). Temperatures reached in the nPCMs–EAIS region dur-ing the Cambrian are not interpreted to exceed mona-zite closure temperatures (Fig. 10). Instead, natural and experimental studies have suggested that monazite is far more reactive in the presence of fluid or melt (e.g. Rapp & Watson, 1986; Kelsey *et al.*, 2008*a*; Harlov *et al.*, 2011; Williams *et al.*, 2011; Högdahl *et al.*, 2012; Kelly *et al.*, 2012; Stepanov *et al.*, 2012; Rubatto *et al.*, 2013; Yakymchuk & Brown, 2014). The preservation of mona-zite during later melting or fluid flow events depends on factors such as the composition of the fluid and mona-zite grain size, with larger grains more likely to be left residual (Rapp & Watson, 1986; Harlov *et al.*, 2011; Williams *et al.*, 2011). There are minor volumes of peg-matite emplaced during the Cambrian throughout the nPCM–EAIS region, suggesting that melt was present within at least some of the metamorphic assemblages (e.g. this study; Manton *et al.*, 1992; Carson *et al.*, 2000; Boger *et al.*, 2002; Ziemann *et al.*, 2005), and the re-placement of biotite by cordierite in some samples is also interpreted to suggest that minor amounts of melt-ing occurred. The rocks with residual chemical compos-itions that preserve localized domains of mineral reaction microstructures (such as samples DP-7, 72046A and PCM-83) contain very little biotite and abundant monazite that is commonly coarse-grained. These samples also contain large numbers of Rayner-

age or partially reset Rayner-age monazite grains. The older ages generally come from grains hosted in coarse-grained M$_1$ minerals (Fig. 9), or from the cores of large monazite grains, whereas younger or discordant analyses come from the cordierite-bearing reaction microstructures.

Whereas our preferred interpretation is that the Cambrian-age monazite reflects high-grade Cambrian metamorphism, it is possible that the younger monazite ages are due to coupled dissolution–reprecipitation as a result of a low-temperature fluid flow event that did not affect the major mineral assemblages in the rock (e.g. Harlov *et al.*, 2011; Williams *et al.*, 2011; Kelly *et al.*, 2012). However, all the samples in this study lack the typical evidence for low-temperature (subsolidus) hy-drous retrogression, such as abundant mica and piniti-zation of cordierite, and preserve largely anhydrous rock compositions and mineralogy consistent with granulite-facies metamorphism and melt loss. Taken to-gether, these suggest that the high-temperature mineral assemblages were not subject to a later, lower-tem-perature fluid flow event that reset the monazite ages. Therefore, the evidence points to the high-temperature formation of new monazite and new mineral assem-blages. This suggests that the cordierite–spinel-bearing assemblages are Cambrian in age and grew as a result of the breakdown of garnet–sillimanite–biotite-bearing assemblages at granulite-facies temperatures. The presence of biotite as a reactant is supported by its tex-turally relict nature within the M$_2$ assemblages, and the abundance of secondary ilmenite in some samples. The interpreted *P–T* conditions of the formation of the M$_2$ assemblages, and the lack of retrogression of the cor-dierite, suggest instead that melt produced during bio-tite breakdown was the likely fluid that aided the resetting of monazite. A second alternative is that the younger monazite ages are the result of monazite reset-ting caused by prolonged exposure to moderate (< 600°C) temperatures, perhaps owing to a long resi-dence time in the mid-crust following the Rayner Orogeny. The discordant age arrays in some samples could be interpreted to reflect diffusional resetting. However, elsewhere in the nPCM, granulite-facies meta-pelites do not show evidence for Cambrian-aged reset-ting of monazite (Morrissey *et al.*, 2015) as would be the case if the Cambrian ages in the samples in this study were the result of diffusional Pb-loss. We therefore in-terpret the age discordia in some samples to reflect mixing of different age micro-domains within the laser ablation pit.

Further evidence for high temperatures during the Cambrian is provided by variable resetting of Sm–Nd systems in garnet from leucogneiss, charnockite and mafic granulite in the eastern nPCM (Hensen *et al.*, 1997). Garnets up to 2–3 mm in diameter yield isochron ages of 630–555 Ma. These are older than the 550–500 Ma ages in the Rayner Complex attributed to Cambrian tectonism (e.g. Boger *et al.*, 2002; Liu *et al.*, 2007*b*, 2009*b*; Phillips *et al.*, 2009), suggesting partial to

almost complete resetting of the Rayner-age Sm–Nd system in garnet. The fastest REE diffusivities suggest that a 2 mm diameter garnet would need to be heated to at least 750°C for 10 Myr, or 850°C for 1 Myr to reset the age (Tirone *et al.*, 2005; Baxter & Scherer, 2013). If the slower REE diffusivities of Carlson (2012) are used, the time scale required to reset the garnets is up to 10 times longer for similar temperatures (Carlson, 2012; Baxter & Scherer, 2013). Therefore, the presence of significantly reset Sm–Nd systematics in garnet suggests that the terrane reached granulite-facies conditions during the Cambrian.

Greenschist-facies mylonites have previously been interpreted to record the *P–T* conditions of Cambrian-age reworking in the nPCM. These greenschist-facies mylonites have not been directly dated, but post-date 550–500 Ma pegmatites and predate the closure of the Rb–Sr system in biotite at *c.* 475 Ma (Boger *et al.*, 2002). Similar, but undated, mylonite zones occur in the Reinbolt Hills (Nichols & Berry, 1991; Nichols, 1995). Therefore, if our interpretation of high temperatures during the Cambrian is correct, the mylonites would have formed during post-peak temperature cooling between *c.* 530 and *c.* 475 Ma.

Metamorphic conditions
Modelled metamorphic conditions
Samples 77090, 77102B and 77079 are located west of the Lambert Glacier in the nPCM and contain dominantly Cambrian monazite and no reaction microstructures; therefore the mineral assemblages are interpreted to dominantly or entirely record one metamorphic event. In these cases, it is likely that the samples experienced the Rayner Orogeny, but were completely recrystallized during the Cambrian. The mineral assemblages in samples 77090, 77102B and 77079 occur over a wide range of conditions, but overlap at temperatures of 790–830°C and 5·5–6·3 kbar (Fig. 10c–e and h).

Sample 77223 is located east of the Lambert Glacier in the EAIS and contains dominantly Cambrian monazite, but has mineral reaction microstructures. The M_2 assemblage for this sample is interpreted to have formed at conditions of 850–880°C and 6·1–7·3 kbar, at slightly higher *T* and *P* conditions than those inferred for the dominantly Cambrian-age samples west of the Lambert Glacier. Samples DP-7, PCM-83 and 72046A are from both east and west of the Lambert Glacier and contain essentially identical mineral assemblages and bimodal monazite populations. The presence of older monazite in garnet and sillimanite porphyroblasts suggests that they may be relics of Rayner-age metamorphism (Fig. 9). The presence of younger monazite in the cordierite–spinel–ilmenite reaction microstructures suggests that the reaction microstructures are likely to be Cambrian in age. The cordierite–spinel–ilmenite reaction microstructures present in these rocks are volumetrically minor, suggesting that only a small amount of

the rock was reactive during Cambrian reworking. The modelled pseudosections suggest that temperatures required to form the cordierite–spinel-bearing assemblages were in the range 820–900°C, with pressures of 5·4–6·4 kbar (Fig. 10a–f and h). These are higher temperatures than those of the non-spinel-bearing samples, and indicate that the spinel stability field is probably extended to lower temperatures and higher pressures owing to the presence of Zn and Cr (e.g. Nichols *et al.*, 1992; Tajćmanová *et al.*, 2009).

Controls on recording of Cambrian metamorphism in nPCM
Despite the interpretation of high temperatures in the nPCM during the Cambrian, and the apparent general similarities in mineral assemblages and chemical compositions in rocks throughout the region, some areas in the nPCM appear to have been metamorphically responsive, whereas others were not (Morrissey *et al.*, 2015). There are numerous examples of previously metamorphosed terranes that record little evidence of later high-temperature events (e.g. Tenczer *et al.*, 2006; Wang *et al.*, 2008; Korhonen *et al.*, 2012; Drüppel *et al.*, 2013). Dehydration during previous high-grade metamorphism not only hinders resetting of geochronometers such as monazite and zircon, it also hinders the formation of new mineral assemblages unless the rocks experience significant strain (e.g. Tenczer *et al.*, 2006; Phillips *et al.*, 2007a; Sajeev *et al.*, 2010; Harlov *et al.*, 2011; Williams *et al.*, 2011). Previous geochronology from the nPCM shows very little evidence for zircon growth during the Cambrian (e.g. Kinny *et al.*, 1997; Boger *et al.*, 2000; Carson *et al.*, 2000). However, there are few geochronology studies from the nPCM and most of these studies have focused on samples of granite and charnockite, which are unlikely to have reactive chemical compositions. There have been no zircon studies from rocks such as metapelites that may have more reactive compositions.

Studies of polymetamorphic terranes suggest that if melting is limited, it is possible to reach granulite–UHT conditions without significant new zircon growth, even where other chronometers such as monazite or xenotime may be reactive (e.g. McFarlane *et al.*, 2006; Wang *et al.*, 2008; Högdahl *et al.*, 2012; Drüppel *et al.*, 2013; Rubatto *et al.*, 2013). In Prydz Bay, several samples from both the Larsemann Hills and the Rauer Group show very little evidence for zircon growth at *c.* 500 Ma, despite the attainment of granulite–UHT conditions (Table 2; e.g. Kinny *et al.*, 1993; Harley, 1998; Grew *et al.*, 2012). Similarly, in the EAIS region, U–Pb zircon ages from high-grade rocks and charnockites show that some outcrops are dominated by Cambrian zircon, whereas adjacent outcrops show little evidence for it (Wang *et al.*, 2008; Liu *et al.*, 2009b). In the Mawson Escarpment, some samples contain Cambrian monazite but no Cambrian zircon (Corvino *et al.*, 2008, 2011; Phillips *et al.*, 2009). The record of Cambrian reworking

in these regions has been suggested to relate to rock fertility and the availability of free fluid (Phillips *et al.*, 2007*a*, 2009; Liu *et al.*, 2009*b*). Conceivably, the patchy nature of the Cambrian reworking in the nPCM reflects a control exerted by the retrograde stage of the Rayner Orogeny. Many granulite terranes contain domains of hydrous retrogression associated with melt crystallization or down-temperature deformation, and there is no logical reason why the nPCM should not also have contained areas of hydrous retrograde mineral growth. Hydrous domains may be sharply bounded by essentially anhydrous, residual granulite chemical compositions (for example, shear zones) or be recorded by diffuse patchy retrogression at the grain scale enclosing relict granulite minerals. During a subsequent thermal event, these retrogressed domains will be reactive and effectively undergo a renewed cycle of prograde metamorphism, whereas the original, anhydrous granulites will remain largely unreactive. Rocks that were extensively retrogressed will completely recrystallize leaving no evidence for the former event, whereas rocks that contained volumetrically minor grain-scale retrogression may develop composite mineral assemblages that comprise newly grown prograde minerals and minerals inherited from the earlier granulite assemblage. In either case, the result will be the terrane exhibiting uniformly granulite-grade rocks, which may be distinguished only by geochronology. Therefore we suggest that the patchy record of Cambrian metamorphism in the nPCM reflects rock reactivity caused by patterns of retrogression associated with the earlier Rayner Orogeny.

Cambrian P–T paths

It is difficult to infer *P–T* evolutions in polymetamorphic terranes (e.g. Hand *et al.*, 1992; Vernon, 1996; Kelsey *et al.*, 2003*b*). Samples 77090, 77102B and 77079 have no reaction microstructures that suggest a likely prograde or retrograde evolution, making it difficult to infer a Cambrian-age *P–T* path. Sample 77223 (from the McKaskle Hills) contains dominantly Cambrian monazite, and it also contains two separate mineral assemblages: an apparent higher pressure garnet + quartz + plagioclase + rutile + sillimanite assemblage, and an apparent lower pressure cordierite + quartz + plagioclase + biotite assemblage (Fig. 10g). However, sample 77223 contains evidence for older monazite, which has been variably reset (Fig. 9i). These older analyses come from monazite hosted within garnet, suggesting that at least part of the mineral assemblage may be older. Samples DP-7, PCM-83 and 72046A contain volumetrically minor reaction microstructures and do not provide obvious information on the Cambrian *P–T* path. The interpreted M_1 garnet–sillimanite–biotite-bearing assemblage could have formed the cordierite–spinel assemblage by either prograde heating during the Cambrian or decompression. However, given the temporal separation between the Rayner Orogeny and the

Cambrian reworking, it is seemingly inevitable that the Cambrian event involved reheating rather than simply decompression.

Preconditioning to reach high temperatures during the Cambrian

Metamorphic conditions during Cambrian reworking in the Rayner Complex involved high apparent thermal gradients of ~115–150°C kbar^{-1} and granulite-facies conditions (Fig. 10h). Attainment of these conditions may have been facilitated by pre-conditioning of the crust that occurred as a result of melt loss and dehydration (e.g. Vielzeuf *et al.*, 1990; Brown & Korhonen, 2009) during the high-temperature *c.* 1000–900 Ma Rayner Orogeny. The Rayner Orogeny is interpreted to have reached temperatures of 850–900°C in the nPCM and MacRoberston Land and temperatures of 870–990°C in Kemp Land (Boger & White, 2003; Halpin *et al.*, 2007*a*, 2007*b*; Morrissey *et al.*, 2015), and involved significant melt loss. Voluminous granitic and charnockitic magmatism occurred between *c.* 1150 and 900 Ma (Halpin *et al.*, 2012). Charnockitic rocks along the Mawson Coast are interpreted to cross-cut the high-grade fabrics in the basement gneisses, suggesting that they intruded after peak metamorphism (Halpin *et al.*, 2007*a*). Modelling of the effect of melt loss shows that it has the capacity to significantly elevate the solidus of the residual rock (e.g. White & Powell, 2002; Korhonen *et al.*, 2010, 2013*a*). The geochemistry of the high-temperature granitic and charnockitic rocks that form most of the outcrop in the Rayner Complex shows that they have low H_2O contents, and would therefore have elevated solidi (e.g. Munksgaard *et al.*, 1992; Kinny *et al.*, 1997; Zhao *et al.*, 1997). Thus, by the end of the Rayner Orogeny, the majority of the Rayner Complex was composed of rocks with 'infertile', mature compositions that would have inhibited significant melting in subsequent events. The infertile nature of the rocks post-Rayner Orogeny means that thermal buffering associated with partial melting would have played a much less significant role during subsequent events, compared with metamorphism of a hydrous terrane (Stüwe, 1995; Thompson & Connolly, 1995; Brown & Korhonen, 2009). As a result, the rocks could have attained higher temperatures (e.g. UHT) much more easily in subsequent events if an appropriate heat source existed (Vielzeuf *et al.*, 1990; Stüwe, 1995; Brown & Korhonen, 2009; Clark *et al.*, 2011; Morrissey *et al.*, 2014; Walsh *et al.*, 2015).

The heat source for Cambrian metamorphism in the nPCM–EAIS region is not well defined. Mikhalsky & Kamenev (2013) suggested that the Cambrian event was mostly thermal, involving emplacement of charnockite as a result of mafic underplating. The tectonic setting of the Rayner Complex during the Cambrian is uncertain, with some workers interpreting it to be intracratonic (e.g. Phillips *et al.*, 2007*b*, 2009; Wilson *et al.*, 2007; Kelsey *et al.*, 2008*b*; Mikhal'sky, 2008), whereas others have interpreted it to be the result of continent–

continent collision (Fitzsimons, 1996; Boger et al., 2001, 2008; Liu et al., 2007a, 2013). If the continent–continent collision model is accepted, the nPCM–EAIS region may have been located in a back-arc extensional setting, which would have provided a thermal driver. Such a setting would logically be associated with comparatively high heat flows, although the geometry and existence of such a system is not well resolved.
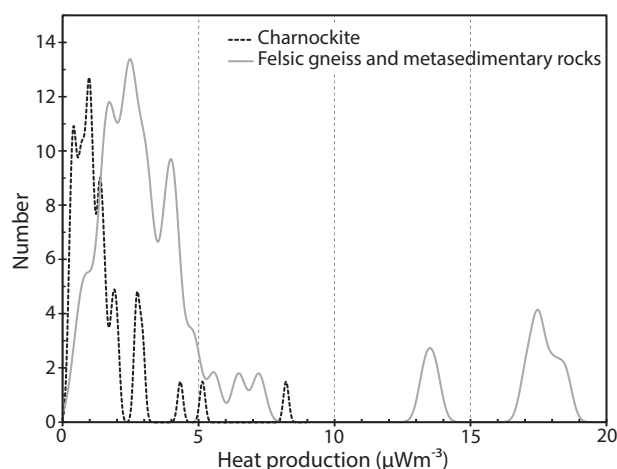
Although a back-arc setting may have provided a thermal driver, it also worth noting that charnockites and pelitic granulites in the formerly contiguous Eastern Ghats terrane in India have internal crustal heat production values of about $3\,\mu W\,m^{-3}$, which is high when compared globally with other Archean and Proterozoic granulites (Kumar et al., 2007). It has been suggested that the heat production from these rocks may have resulted in elevated crustal temperatures at 550 Ma in the Eastern Ghats system, and is therefore a possible cause for the metamorphism recorded during the Cambrian (Kumar et al., 2007). Proterozoic rocks in the Rayner Complex have average crustal heat production values of $\sim2\,\mu W\,m^{-3}$ (Carson & Pittard, 2012). Published geochemical data for the nPCM (e.g. Manton et al., 1992; Munksgaard et al., 1992; Kinny et al., 1997; Stephenson & Cook, 1997; Zhao et al., 1997; Mikhalsky et al., 2001b) suggest that the majority of the felsic gneisses and metasediments have heat production values of ~2–$5\,\mu W\,m^{-3}$, similar to the rocks in the Eastern Ghats Province (Fig. 11); these are high by global standards. The proportion of metasedimentary rocks within the nPCM is not known. However, regional geophysical interpretations (Golynsky et al., 2006; McLean et al., 2009) suggest that significant amounts of the nPCM, extending to Depot Peak, comprise metasedimentary lithologies. If this is the case, the heat production from the

Fig. 11. Heat production rates at 550 Ma determined from geochemistry of charnockite and felsic gneiss and associated metapelitic lithologies. Data from this study, Manton et al. (1992), Munksgaard et al. (1992), Kinny et al. (1997), Stephenson & Cook (1997), Young et al. (1997) and Zhao et al. (1997). Regional geophysical interpretations suggest that $\sim30\%$ of the nPCM region may comprise felsic and metasedimentary lithologies (Golynsky et al., 2006).

metasediments and felsic gneisses (Fig. 11) may have played a significant role in heating the terrane during the Cambrian, particularly given the anhydrous nature of the rocks. Burial of heat-producing rocks may be a thermal source for high-grade metamorphism (e.g. Sandiford & Hand, 1998; McLaren et al., 2005; Clark et al., 2011; Anderson et al., 2013; Morrissey et al., 2014). The lack of a clearly defined Cambrian P–T evolution in the Rayner Complex means that burial of high heat-producing rocks as a mechanism for the metamorphism is speculative. Nonetheless, the compositions of the Rayner Complex charnockites and metasedimentary rocks are thermally energetic for rocks that have experienced deep crustal metamorphism.

Links with the Eastern Ghats

There is general agreement that paleogeographical reconstructions within Gondwana support a contiguous Rayner–Eastern Ghats terrane (e.g. Mezger & Cosca, 1999; Fitzsimons, 2000; Boger, 2011), and it therefore seems that the now separate regions were once part of a large, high-grade province. The two regions share a similar Neoproterozoic history, with high-temperature metamorphism and extensive charnockitic magmatism between c. 1150 and 900 Ma (e.g. Mezger & Cosca, 1999; Carson et al., 2000; Bose et al., 2011; Gupta, 2012; Halpin et al., 2012; Korhonen et al., 2013b). Therefore, given the evidence for Cambrian-age reworking in parts of the Rayner Complex, it is also possible that the Eastern Ghats experienced a similar high-T overprint during the Cambrian.

Cambrian-age tectonism is thought to have modified the internal structure of the Eastern Ghats Province (Dobmeier & Raith, 2003; Simmat & Raith, 2008). Cambrian reworking involved north- to NW-directed deformation focused along the boundary between the Eastern Ghats Province and the older cratons to the west (Simmat & Raith, 2008; Gupta, 2012). Electron microprobe analysis (EPMA) monazite ages of 530–470 Ma from sheared granulites and the growth of new monazite rims have been associated with hydration during this event (Mezger & Cosca, 1999; Simmat & Raith, 2008; Gupta, 2012), as has new growth of zircon in aplite veins (Mezger & Cosca, 1999; Simmat & Raith, 2008). Undeformed pegmatite dykes at c. 515–500 Ma have also been observed in the central migmatite domain (Simmat & Raith, 2008). Low-T chronometers such as titanite and isotopic systems such as Ar–Ar, Sm–Nd and Rb–Sr have been variably reset to c. 500 Ma (Shaw et al., 1997; Mezger & Cosca, 1999; Crowe et al., 2001; Dobmeier et al., 2006). The thermal regime associated with the Cambrian overprint in the Eastern Ghats has been interpreted to have been mid-amphibolite facies (Mezger & Cosca, 1999; Crowe et al., 2001). However, some samples from high-grade granulites in the central Eastern Ghats show bimodal distributions in monazite age data, which are similar to those observed in the samples from this study that contain localized

mineral reaction microstructures (Simmat & Raith, 2008; Korhonen *et al.*, 2013*b*). Therefore, it seems plausible that the Eastern Ghats may have experienced similar Cambrian-age reworking to the Rayner Complex.

CONCLUSIONS

In situ monazite U–Pb geochronology combined with calculated phase diagrams for samples from throughout the nPCM–EAIS area of the Rayner Complex suggest that parts of the Rayner–Eastern Ghats terrane experienced high-temperature metamorphism between 540 and 500 Ma. Temperatures were in the range 800–850°C at pressures of 5·5–6·5 kbar. This study extends the footprint of Cambrian reworking into the nPCM. This approach shows the importance of careful interpretation of mineral assemblages and *P–T* paths when identifying polymetamorphic terranes. Multiple high-grade events may produce a terrane that appears to preserve granulite-facies assemblages formed at similar conditions, when these assemblages may be recording temporally different events. Secondary events may be recorded only in spatially restricted locations, where there is an availability of free fluid that allows resetting of geochronometers and the formation of new mineral assemblages. These terranes may be preconditioned to reach high temperatures by previous high-grade metamorphism, which dehydrates the terrane and leaves behind rocks with elevated solidi that are unable to thermally buffer temperatures by melting. High crustal heat production in the Rayner–Eastern Ghats terranes may have further facilitated the attainment of high temperatures.

ACKNOWLEDGEMENTS

FUNDING

SUPPLEMENTARY DATA

Supplementary data for this paper are available at *Journal of Petrology* online.

REFERENCES

Anderson, J. R., Kelsey, D. E., Hand, M. & Collins, W. J. (2013). Conductively driven, high-thermal gradient metamorphism in the Anmatjira Range, Arunta region, central Australia. *Journal of Metamorphic Geology* **31**, 1003–1026.

Baxter, E. F. & Scherer, E. E. (2013). Garnet geochronology: timekeeper of tectonometamorphic processes. *Elements* **9**, 433–438.

Beliatsky, B. V., Laiba, A. A. & Mikhalsky, E. V. (1994). U–Pb zircon age of the metavolcanic rocks of Fisher Massif (Prince Charles Mountains, East Antarctica). *Antarctic Science* **6**, 355–358.

Boger, S. D. (2011). Antarctica—Before and after Gondwana. *Gondwana Research* **19**, 335–371.

Boger, S. D. & White, R. W. (2003). The metamorphic evolution of metapelitic granulites from Radok Lake, northern Prince Charles Mountains, east Antarctica; evidence for an anticlockwise *P–T* path. *Journal of Metamorphic Geology* **21**, 285–298.

Boger, S. D. & Wilson, C. J. L. (2005). Early Cambrian crustal shortening and a clockwise *P–T–t* path from the southern Prince Charles Mountains, East Antarctica: implications for the formation of Gondwana. *Journal of Metamorphic Geology* **23**, 603–623.

Boger, S. D., Carson, C. J., Wilson, C. J. L. & Fanning, C. M. (2000). Neoproterozoic deformation in the Radok Lake region of the northern Prince Charles Mountains, east Antarctica; evidence for a single protracted orogenic event. *Precambrian Research* **104**, 1–24.

Boger, S. D., Wilson, C. J. L. & Fanning, C. M. (2001). Early Paleozoic tectonism within the East Antarctic craton: The final suture between east and west Gondwana? *Geology* **29**, 463–466.

Boger, S. D., Carson, C. J., Fanning, C. M., Hergt, J. M., Wilson, C. J. L. & Woodhead, J. D. (2002). Pan-African intraplate deformation in the northern Prince Charles Mountains, east Antarctica. *Earth and Planetary Science Letters* **195**, 195–210.

Boger, S. D., Maas, R. & Fanning, C. M. (2008). Isotopic and geochemical constraints on the age and origin of granitoids from the central Mawson Escarpment, southern Prince Charles Mountains, East Antarctica. *Contributions to Mineralogy and Petrology* **155**, 379–400.

Boger, S. D., White, R. W. & Schulte, B. (2012). The importance of iron speciation (Fe^{+2}/Fe^{+3}) in determining mineral assemblages: an example from the high-grade aluminous metapelites of southeastern Madagascar. *Journal of Metamorphic Geology* **30**, 997–1018.

Bose, S., Das, K. & Fukuoka, M. (2005). Fluorine content of biotite in granulite-grade metapelitic assemblages and its implications for the Eastern Ghats granulites. *European Journal of Mineralogy* **17**, 665–674.

Bose, S., Dunkley, D. J., Dasgupta, S., Das, K. & Arima, M. (2011). India–Antarctica–Australia–Laurentia connection in the Paleoproterozoic–Mesoproterozoic revisited: Evidence from new zircon U–Pb and monazite chemical age data from the Eastern Ghats Belt, India. *Geological Society of America Bulletin* **123**, 2031–2049.

Brown, M. (2010). Melting of the continental crust during orogenesis: the thermal, rheological, and compositional consequences of melt transport from lower to upper continental crust. *Canadian Journal of Earth Sciences* **47**, 655–694.

Brown, M. & Korhonen, F. J. (2009). Some remarks on melting and extreme metamorphism of crustal rocks. In: Gupta, A. K. & Dasgupta, S. (eds) *Physics and Chemistry of the Earth's Interior*. Springer, pp. 67–87.

Carlson, W. D. (2012). Rates and mechanism of Y, REE, and Cr diffusion in garnet. *American Mineralogist* **97**, 1598–1618.

Carson, C. J. & Pittard, M. (2012). *A reconnaissance crustal heat production assessment of the Australian Antarctic Territory (AAT)*. Geoscience Australia.

Carson, C. J., Dirks, P. G. H. M., Hand, M., Sims, J. P. & Wilson, C. J. L. (1995). Compressional and extensional tectonics in low–medium pressure granulites from the Larsemann Hills, East Antarctica. *Geological Magazine* **132**, 151–170.

Carson, C. J., Fanning, C. M. & Wilson, C. J. L. (1996). Timing of the Progress Granite, Larsemann Hills: Additional evidence for early Palaeozoic orogenesis within the east Antarctic Shield and implications for Gondwana assembly. *Australian Journal of Earth Sciences* **43**, 539–553.

Carson, C. J., Powell, R., Wilson, C. J. L. & Dirks, P. H. G. M. (1997). Partial melting during tectonic exhumation of a granulite terrane: an example from the Larsemann Hills, East Antarctica. *Journal of Metamorphic Geology* **15**, 105–126.

Carson, C. J., Boger, S. D., Fanning, C. M., Wilson, C. J. L. & Thost, D. E. (2000). SHRIMP U–Pb geochronology from Mount Kirkby, northern Prince Charles Mountains, East Antarctica. *Antarctic Science* **12**, 429–442.

Cesare, B., Satish-Kumar, M., Cruciani, G., Pocker, S. & Nodari, L. (2008). Mineral chemistry of Ti-rich biotite from pegmatite and metapelitic granulites of the Kerala Khondalite Belt (southeast India): Petrology and further insight into titanium substitutions. *American Mineralogist* **93**, 327–338.

Cherniak, D. J. (2010). Diffusion in accessory minerals: zircon, titanite, apatite, monazite and xenotime. In: Zhang, Y. & Cherniak, D. J. (eds) *Diffusion in Minerals and Melts. Mineralogical Society of America and Geochemical Society, Reviews in Mineralogy and Geochemistry* **72**, 827–869.

Cherniak, D. J., Watson, E. B., Grove, M. & Harrison, T. M. (2004). Pb diffusion in monazite: a combined RBS/SIMS study. *Geochimica et Cosmochimica Acta* **68**, 829–840.

Clark, C., Fitzsimons, I. C. W., Healy, D. & Harley, S. L. (2011). How does the continental crust get really hot? *Elements* **7**, 235–240.

Clarke, G. L. (1988). Structural constraints on the Proterozoic reworking of Archaean crust in the Rayner Complex, MacRobertson and Kemp Land coast, East Antarctica. *Precambrian Research* **40–41**, 137–156.

Coggon, R. & Holland, T. J. B. (2002). Mixing properties of phengitic micas and revised garnet–phengite thermobarometers. *Journal of Metamorphic Geology* **20**, 683–696.

Corvino, A. F., Boger, S. D., Henjes-Kunst, F., Wilson, C. J. L. & Fitzsimons, I. C. W. (2008). Superimposed tectonic events at 2450 Ma, 2100 Ma, 900 Ma and 500 Ma in the North Mawson Escarpment, Antarctic Prince Charles Mountains. *Precambrian Research* **167**, 281–302.

Corvino, A. F., Wilson, C. J. L. & Boger, S. D. (2011). The structural and tectonic evolution of a Rodinian continental fragment in the Mawson Escarpment, Prince Charles Mountains, Antarctica. *Precambrian Research* **184**, 70–92.

Crowe, W. A., Cosca, M. A. & Harris, L. B. (2001). $^{40}Ar/^{39}Ar$ geochronology and Neoproterozoic tectonics along the northern margin of the Eastern Ghats Belt in north Orissa, India. *Precambrian Research* **108**, 237–266.

Cubley, J. F., Pattison, D. R. M., Tinkham, D. K. & Fanning, C. M. (2013). U–Pb geochronological constraints on the timing of episodic regional metamorphism and rapid high-*T* exhumation of the Grand Forks complex, British Columbia. *Lithos* **156–159**, 241–267.

Cutts, K. A., Kelsey, D. E. & Hand, M. (2013). Evidence for late Paleoproterozoic (*ca* 1690–1665 Ma) high- to ultrahigh-temperature metamorphism in southern Australia: Implications for Proterozoic supercontinent models. *Gondwana Research* **23**, 617–640.

Deer, W. A., Howie, R. A. & Zussman, J. (1992). *An Introduction to the Rock-forming Minerals*, 2nd edn. Longman.

Diener, J. F. A. & Powell, R. (2010). Influence of ferric iron on the stability of mineral assemblages. *Journal of Metamorphic Geology* **28**, 599–613.

Diener, J. F. A., White, R. W. & Powell, R. (2008). Granulite facies metamorphism and subsolidus fluid-absent reworking, Strangways Range, Arunta Block, central Australia. *Journal of Metamorphic Geology* **26**, 603–622.

Dirks, P. H. G. M. & Hand, M. (1995). Clarifying temperature–pressure paths via structures in granulite from the Bolingen Islands, Antarctica. *Australian Journal of Earth Sciences* **42**, 157–172.

Dirks, P. H. G. M. & Wilson, C. J. L. (1995). Crustal evolution of the East Antarctic mobile belt in Prydz Bay: continental collision at 500 Ma? *Precambrian Research* **75**, 189–207.

Dobmeier, C. J. & Raith, M. M. (2003). Crustal architecture and evolution of the Eastern Ghats Belt and adjacent regions of India. In: Yoshida, M., Windley, B. F. & Dasgupta, S. (eds) *Proterozoic East Gondwana: Supercontinent Assembly and Breakup. Geological Society, London, Special Publications* **206**, 145–168.

Dobmeier, C., Lütke, S., Hammerschmidt, K. & Mezger, K. (2006). Emplacement and deformation of the Vinukonda meta-granite (Eastern Ghats, India)—Implications for the geological evolution of peninsular India and for Rodinia reconstructions. *Precambrian Research* **146**, 165–178.

Droop, G. T. R. (1987). A general equation for estimating Fe^{3+} concentrations in ferromagnesian silicates and oxides from microprobe analyses, using stoichiometric criteria. *Mineralogical Magazine* **51**, 431–435.

Drüppel, K., Elsäßer, L., Brandt, S. & Gerdes, A. (2013). Sveconorwegian mid-crustal ultrahigh-temperature metamorphism in Rogaland, Norway: U–Pb LA-ICP-MS geochronology and pseudosections of sapphirine granulites and associated paragneisses. *Journal of Petrology* **54**, 305–350.

Dutch, R. A., Hand, M. & Clark, C. (2005). Cambrian reworking of the southern Australian Proterozoic Curnamona Province: constraints from regional shear-zone systems. *Journal of the Geological Society, London* **162**, 763–775.

Fitzsimons, I. C. W. (1996). Metapelitic migmatites from Brattstrand Bluffs, East Antarctica—metamorphism, melting and exhumation of the mid crust. *Journal of Petrology* **37**, 395–414.

Fitzsimons, I. C. W. (2000). A review of tectonic events in the East Antarctic Shield and their implications for Gondwana and earlier supercontinents. *Journal of African Earth Sciences* **31**, 3–23.

Fitzsimons, I. C. W. & Harley, S. L. (1991). Geological relationships in high-grade gneiss of the Brattstrand Bluffs coastline, Prydz Bay, East Antarctica. *Australian Journal of Earth Sciences* **38**, 497–519.

Fitzsimons, I. C. W. & Harley, S. L. (1992). Mineral reaction textures in high-grade gneisses: evidence for contrasting pressure–temperature paths in the Proterozoic Complex of East Antarctica. In: Yoshida, M., Kaminuma, K. & Shiraishi, K. (eds) *Recent Progress in Antarctic Earth Science*. Terra Scientific Publishing, pp. 103–111.

Fitzsimons, I. C. W. & Thost, D. E. (1992). Geological relationships in high-grade basement gneiss of the northern Prince Charles Mountains, East Antarctica. *Australian Journal of Earth Sciences* **39**, 173–193.

Fitzsimons, I. C. W., Kinny, P. D. & Harley, S. L. (1997). Two stages of zircon and monazite growth in anatectic leucogneiss: SHRIMP constraints on the duration and intensity of Pan-African metamorphism in Prydz Bay, East Antarctica. *Terra Nova* **9**, 47–51.

Foster, G. & Parrish, R. R. (2003). Metamorphic monazite and the generation of *P–T–t* paths. In: Vance, D., Müller, W. &

Villa, I. M. (eds) *Geochronology: Linking the Isotopic Record with Petrology and Textures. Geological Society, London, Special Publications* **220**, 25–47.

Fyfe, W. S. (1973). The granulite facies, partial melting and the Archaean crust. *Philosophical Transactions of the Royal Society of London, Series A* **273**, 457–461.

Gasser, D., Bruand, E., Rubatto, D. & Stüwe, K. (2012). The behaviour of monazite from greenschist facies phyllites to anatectic gneisses: An example from the Chugach Metamorphic Complex, southern Alaska. *Lithos* **134–135**, 108–122.

Gervais, F. & Hynes, A. (2013). Linking metamorphic textures to U–Pb monazite *in-situ* geochronology to determine the age and nature of aluminosilicate-forming reactions in the northern Monashee Mountains, British Columbia. *Lithos* **160–161**, 250–267.

Golynsky, A., Masolov, V., Volnukhin, V. & Golynsky, D. (2006). Crustal provinces of the Prince Charles Mountains region and surrounding areas in the light of aeromagnetic data. In: Fütterer, D., Damaske, D., Kleinschmidt, G., Miller, H. & Tessensohn, F. (eds) *Antarctica*. Springer, pp. 83–94.

Goncalves, P., Nicollet, C. & Montel, J.-M. (2004). Petrology and *in situ* U–Th–Pb monazite geochronology of ultrahigh-temperature metamorphism from the Andriamena mafic unit, north–central Madagascar. Significance of a petrographical P–T path in a polymetamorphic context. *Journal of Petrology* **45**, 1923–1957.

Grew, E. S., Carson, C. J., Christy, A. G., Maas, R., Yaxley, G. M., Boger, S. D. & Fanning, C. M. (2012). New constraints from U–Pb, Lu–Hf and Sm–Nd isotopic data on the timing of sedimentation and felsic magmatism in the Larsemann Hills, Prydz Bay, East Antarctica. *Precambrian Research* **206–207**, 87–108.

Griffin, W. L., Belousova, E. A., Shee, S. R., Pearson, N. J. & O'Reilly, S. Y. (2004). Archean crustal evolution in the northern Yilgarn Craton: U–Pb and Hf-isotope evidence from detrital zircons. *Precambrian Research* **131**, 231–282.

Gupta, S. (2012). Strain localization, granulite formation and geodynamic setting of 'hot orogens': a case study from the Eastern Ghats Province, India. *Geological Journal* **47**, 334–351.

Halpin, J. A., Clarke, G. L., White, R. W. & Kelsey, D. E. (2007*a*). Contrasting *P–T–t* paths for Neoproterozoic metamorphism in MacRobertson and Kemp Lands, east Antarctica. *Journal of Metamorphic Geology* **25**, 683–701.

Halpin, J. A., White, R. W., Clarke, G. L. & Kelsey, D. E. (2007*b*). The Proterozoic *P–T–t* evolution of the Kemp Land coast, East Antarctica; constraints from Si-saturated and Si-undersaturated metapelites. *Journal of Petrology* **48**, 1321–1349.

Halpin, J. A., Daczko, N. R., Milan, L. A. & Clarke, G. L. (2012). Decoding near-concordant U–Pb zircon ages spanning several hundred million years: recrystallisation, metamictisation or diffusion? *Contributions to Mineralogy and Petrology* **163**, 67–85.

Halpin, J. A., Daczko, N. R., Clarke, G. L. & Murray, K. R. (2013). Basin analysis in polymetamorphic terranes: An example from east Antarctica. *Precambrian Research* **231**, 78–97.

Hand, M., Dirks, P., Powell, R. & Buick, I. S. (1992). How well established is isobaric cooling in Proterozoic orogenic belts? An example from the Arunta Inlier, central Australia. *Geology* **20**, 649–652.

Hand, M., Scrimgeour, I., Powell, R., Stüwe, K. & Wilson, C. J. L. (1994*a*). Metapelitic granulites from Jetty Peninsula, east Antarctica: formation during a single event or by polymetamorphism? *Journal of Metamorphic Geology* **12**, 557–573.

Hand, M., Scrimgeour, I., Stuwe, K., Arne, D. & Wilson, C. J. L. (1994*b*). Geological observations in high-grade mid-Proterozoic rocks from Else Platform, northern Prince Charles Mountains region, east Antarctica. *Australian Journal of Earth Sciences* **41**, 311–329.

Harley, S. L. (1998). Ultrahigh temperature granulite metamorphism (1050°C, 12 kbar) and decompression in garnet (Mg70)–orthopyroxene–sillimanite gneisses from the Rauer Group, East Antarctica. *Journal of Metamorphic Geology* **16**, 541–562.

Harlov, D. E., Wirth, R. & Hetherington, C. J. (2011). Fluid-mediated partial alteration in monazite: the role of coupled dissolution–reprecipitation in element redistribution and mass transfer. *Contributions to Mineralogy and Petrology* **162**, 329–348.

Hensen, B. J. & Zhou, B. (1995*a*). A Pan-African granulite facies metamorphic episode in Prydz Bay, Antarctica: Evidence from Sm–Nd garnet dating. *Australian Journal of Earth Sciences* **42**, 249–258.

Hensen, B. J. & Zhou, B. (1995*b*). Retention of isotopic memory in garnets partially broken down during an overprinting granulite-facies metamorphism: Implications for the Sm–Nd closure temperature. *Geology* **23**, 225–228.

Hensen, B. J., Zhou, B. & Thost, D. E. (1997). Recognition of multiple high grade metamorphic events with garnet Sm–Nd chronology in the northern Prince Charles Mountains, Antarctica. In: Ricci, C. A. (ed.) *The Antarctic Region: Geological Evolution and Processes*. Terra Antartica, pp. 97–104.

Högdahl, K., Majka, J., Sjöström, H., Nilsson, K., Claesson, S. & Konečný, P. (2012). Reactive monazite and robust zircon growth in diatexites and leucogranites from a hot, slowly cooled orogen: implications for the Palaeoproterozoic tectonic evolution of the central Fennoscandian Shield, Sweden. *Contributions to Mineralogy and Petrology* **163**, 167–188.

Holland, T. J. B. & Powell, R. (1998). An internally consistent thermodynamic dataset for phases of petrological interest. *Journal of Metamorphic Geology* **16**, 309–343.

Holland, T. J. B. & Powell, R. (2003). Activity–composition relations for phases in petrological calculations: an asymmetric multicomponent formulation. *Contributions to Mineralogy and Petrography* **145**, 492–501.

Johnson, T. E. & White, R. W. (2011). Phase equilibrium constraints on conditions of granulite-facies metamorphism at Scourie, NW Scotland. *Journal of the Geological Society, London* **168**, 147–158.

Kamenev, E. N. (1972). Geological structure of Enderby Land. In: Adie, R. J. (ed.) *Antarctic Geology and Geophysics*. International Union of Geological Sciences (IUGS), pp. 579–583.

Kelly, N. M. & Harley, S. L. (2004). Orthopyroxene–corundum in Mg–Al-rich granulites from the Oygarden Islands, east Antarctica. *Journal of Petrology* **45**, 1481–1512.

Kelly, N. M., Clarke, G. L. & Fanning, C. M. (2002). A two-stage evolution of the Neoproterozoic Rayner Structural Episode: new U–Pb sensitive high resolution ion microprobe constraints from the Oygarden Group, Kemp Land, East Antarctica. *Precambrian Research* **116**, 307–330.

Kelly, N. M., Harley, S. L. & Möller, A. (2012). Complexity in the behavior and recrystallization of monazite during high-*T* metamorphism and fluid infiltration. *Chemical Geology* **322–323**, 192–208.

Kelsey, D. E. & Hand, M. (2015). On ultrahigh temperature crustal metamorphism: phase equilibria, trace element thermometry, bulk composition, heat sources, timescales and tectonic settings. *Geoscience Frontiers* **6**, 311–356.

Kelsey, D. E., Powell, R., Wilson, C. J. L. & Steel, D. A. (2003*a*). (Th + U)–Pb monazite ages from Al–Mg-rich metapelites, Rauer Group, east Antarctica. *Contributions to Mineralogy and Petrography* **146**, 326–340.

Kelsey, D. E., White, R. W. & Powell, R. (2003*b*). Orthopyroxene–sillimanite–quartz assemblages: distribution, petrology, quantitative *P–T–X* constraints and *P–T* paths. *Journal of Metamorphic Geology* **21**, 439–453.

Kelsey, D. E., White, R. W., Powell, R., Wilson, C. J. L. & Quinn, C. D. (2003*c*). New constraints on metamorphism in the Rauer Group, Prydz Bay, east Antarctica. *Journal of Metamorphic Geology* **21**, 739–759.

Kelsey, D. E., Hand, M., Clark, C. & Wilson, C. J. L. (2007). On the application of *in situ* monazite chemical geochronology to constraining *P–T–t* histories in high-temperature (>850°C) polymetamorphic granulites from Prydz Bay, East Antarctica. *Journal of the Geological Society, London* **164**, 667–683.

Kelsey, D. E., Clark, C. & Hand, M. (2008*a*). Thermobarometric modelling of zircon and monazite growth in melt-bearing systems: examples using model metapelitic and metapsammitic granulites. *Journal of Metamorphic Geology* **26**, 199–212.

Kelsey, D. E., Wade, B. P., Collins, A. S., Hand, M., Sealing, C. R. & Netting, A. (2008*b*). Discovery of a Neoproterozoic basin in the Prydz Belt in East Antarctica and its implications for Gondwana assembly and ultrahigh temperature metamorphism. *Precambrian Research* **161**, 355–388.

Kinny, P. D., Black, L. P. & Sheraton, J. W. (1993). Zircon ages and the distribution of Archaean and Proterozoic rocks in the Rauer Islands. *Antarctic Science* **5**, 193–206.

Kinny, P. D., Black, L. P. & Sheraton, J. W. (1997). Zircon U–Pb ages and geochemistry of igneous and metamorphic rocks in the northern Prince Charles Mountains, Antarctica. *AGSO Journal of Australian Geology and Geophysics* **16**, 637–654.

Korhonen, F. J., Saito, S., Brown, M. & Siddoway, C. S. (2010). Modeling multiple melt loss events in the evolution of an active continental margin. *Lithos* **116**, 230–248.

Korhonen, F. J., Brown, M., Grove, M., Siddoway, C. S., Baxter, E. F. & Inglis, J. D. (2012). Separating metamorphic events in the Fosdick migmatite–granite complex, West Antarctica. *Journal of Metamorphic Geology* **30**, 165–192.

Korhonen, F. J., Brown, M., Clark, C. & Bhattacharya, S. (2013*a*). Osumilite–melt interactions in ultrahigh temperature granulites: phase equilibria modelling and implications for the *P–T–t* evolution of the Eastern Ghats Province, India. *Journal of Metamorphic Geology* **31**, 881–907.

Korhonen, F. J., Clark, C., Brown, M., Bhattacharya, S. & Taylor, R. (2013*b*). How long-lived is ultrahigh temperature (UHT) metamorphism? Constraints from zircon and monazite geochronology in the Eastern Ghats orogenic belt, India. *Precambrian Research* **234**, 322–350.

Kumar, P. S., Menon, R. & Reddy, G. K. (2007). The role of radiogenic heat production in the thermal evolution of a Proterozoic granulite-facies orogenic belt: Eastern Ghats, Indian Shield. *Earth and Planetary Science Letters* **254**, 39–54.

Liu, X., Jahn, B.-m., Zhao, Y., Li, M., Li, H. & Liu, X. (2006). Late Pan-African granitoids from the Grove Mountains, East Antarctica: Age, origin and tectonic implications. *Precambrian Research* **145**, 131–154.

Liu, X., Jahn, B.-M., Zhao, Y., Zhao, G. & Liu, X. (2007*a*). Geochemistry and geochronology of high-grade rocks from the Grove Mountains, East Antarctica: Evidence for an Early Neoproterozoic basement metamorphosed during a single Late Neoproterozoic/Cambrian tectonic cycle. *Precambrian Research* **158**, 93–118.

Liu, X., Zhao, Y., Zhao, G., Jian, P. & Xu, G. (2007*b*). Petrology and geochronology of granulites from the McKaskle Hills, Eastern Amery Ice Shelf, Antarctica, and implications for the evolution of the Prydz Belt. *Journal of Petrology* **48**, 1443–1470.

Liu, X., Hu, J., Zhao, Y., Lou, Y., Wei, C. & Liu, X. (2009*a*). Late Neoproterozoic/Cambrian high-pressure mafic granulites from the Grove Mountains, East Antarctica: *P–T–t* path, collisional orogeny and implications for assembly of East Gondwana. *Precambrian Research* **174**, 181–199.

Liu, X., Zhao, Y., Song, B., Liu, J. & Cui, J. (2009*b*). SHRIMP U–Pb zircon geochronology of high-grade rocks and charnockites from the eastern Amery Ice Shelf and southwestern Prydz Bay, East Antarctica: Constraints on Late Mesoproterozoic to Cambrian tectonothermal events related to supercontinent assembly. *Gondwana Research* **16**, 342–361.

Liu, X., Zhao, Y. & Hu, J. (2013). The *c.* 1000–900 Ma and *c.* 550–500 Ma tectonothermal events in the Prince Charles Mountains–Prydz Bay region, East Antarctica, and their relations to supercontinent evolution. In: Harley, S. L., Fitzsimons, I. C. W. & Zhao, Y. (eds) *Antarctica and Supercontinent Evolution. Geological Society, London, Special Publications* **383**, 95–112.

Liu, X., Jahn, B.-m., Zhao, Y., Liu, J. & Ren, L. (2014). Geochemistry and geochronology of Mesoproterozoic basement rocks from the Eastern Amery Ice Shelf and southwestern Prydz Bay, East Antarctica: Implications for a long-lived magmatic accretion in a continental arc. *American Journal of Science* **314**, 508–547.

Manton, W. I., Grew, E. S., Hofmann, J. & Sheraton, J. W. (1992). Granitic rocks of the Jetty Peninsula, Amery Ice Shelf area, East Antarctica. In: Yoshida, Y., Kaminuma, K. & Shiraishi, K. (eds) *Recent Progress in Antarctic Earth Science*. Terra Scientific Publishing, pp. 179–189.

McFarlane, C. R. M., Connelly, J. N. & Carlson, W. D. (2006). Contrasting response of monazite and zircon to a high-*T* thermal overprint. *Lithos* **88**, 135–149.

McLaren, S., Sandiford, M. & Powell, R. (2005). Contrasting styles of Proterozoic crustal evolution: A hot-plate tectonic model for Australian terranes. *Geology* **33**, 673–676.

McLean, M. A., Wilson, C. J. L., Boger, S. D., Betts, P. G., Rawling, T. J. & Damaske, D. (2009). Basement interpretations from airborne magnetic and gravity data over the Lambert Rift region of East Antarctica. *Journal of Geophysical Research: Solid Earth* **114**, B06101.

Meert, J. G. (2003). A synopsis of events related to the assembly of eastern Gondwana. *Tectonophysics* **362**, 1–40.

Mezger, K. & Cosca, M. A. (1999). The thermal history of the Eastern Ghats Belt (India) as revealed by U–Pb and ^{40}Ar/^{39}Ar dating of metamorphic and magmatic minerals: implications for the SWEAT correlation. *Precambrian Research* **94**, 251–271.

Mikhal'sky, E. V. (2008). Main stages and geodynamic regimes of the Earth's crust formation in East Antarctica in the Proterozoic and Early Paleozoic. *Geotectonics* **42**, 413–429.

Mikhalsky, E. V. & Kamenev, I. A. (2013). Recurrent transitional group charnockites in the east Amery Ice Shelf coast (East Antarctica): Petrogenesis and implications on tectonic evolution. *Lithos* **175–176**, 230–243.

Mikhalsky, E. V., Sheraton, J. W., Laiba, A. A. & Beliatsky, B. V. (1996). Geochemistry and origin of Mesoproterozoic metavolcanic rocks from Fisher Massif, Prince Charles Mountains, East Antarctica. *Antarctic Science* **8**, 85–104.

Mikhalsky, E. V., Sheraton, J. W. & Beliatsky, B. V. (2001*a*). Preliminary U–Pb dating of Grove Mountains rocks: implications for the Proterozoic to Early Palaeozoic tectonic evolution of the

Lambert Glacier–Prydz Bay area (East Antarctica). *Terra Antartica* **8**, 3–10.

Mikhalsky, E. V., Sheraton, J. W., Laiba, A. A., Tingey, R. J., Thost, D. E., Kamenev, I. A. & Fedorov, L. V. (eds) (2001*b*). *Geology of the Prince Charles Mountains, Antarctica. AGSO Geoscience Australia Bulletin* **247**, 209 pp.

Mikhalsky, E. V., Beliatsky, B. V., Sheraton, J. W. & Roland, N. W. (2006*a*). Two distinct Precambrian terranes in the Southern Prince Charles Mountains, East Antarctica: SHRIMP dating and geochemical constraints. *Gondwana Research* **9**, 291–309.

Mikhalsky, E., Laiba, A. & Beliatsky, B. (2006*b*). Tectonic subdivision of the Prince Charles Mountains: a review of geologic and isotopic data. In: Fütterer, D., Damaske, D., Kleinschmidt, G., Miller, H. & Tessensohn, F. (eds) *Antarctica*. Springer, pp. 69–81.

Morrissey, L., Payne, J. L., Kelsey, D. E. & Hand, M. (2011). Grenvillian-aged reworking in the North Australian Craton, central Australia: Constraints from geochronology and modelled phase equilibria. *Precambrian Research* **191**, 141–165.

Morrissey, L. J., Hand, M., Wade, B. P. & Szpunar, M. (2013). Early Mesoproterozoic metamorphism in the Barossa Complex, South Australia: links with the eastern margin of Proterozoic Australia. *Australian Journal of Earth Sciences* **60**, 769–795.

Morrissey, L. J., Hand, M., Raimondo, T. & Kelsey, D. E. (2014). Long-lived high-temperature, low-pressure granulite facies metamorphism in the Arunta Region, central Australia. *Journal of Metamorphic Geology* **32**, 25–47.

Morrissey, L. J., Hand, M. & Kelsey, D. E. (2015). Multi-stage metamorphism in the Rayner–Eastern Ghats Terrane: *P–T–t* constraints from the northern Prince Charles Mountains, east Antarctica. *Precambrian Research* **267**, 137–163.

Munksgaard, N. C., Thost, D. E. & Hensen, B. J. (1992). Geochemistry of Proterozoic granulites from northern Prince Charles Mountains, East Antarctica. *Antarctic Science* **4**, 59–69.

Nichols, G., Berry, R. & Green, D. (1992). Internally consistent gahnitic spinel–cordierite–garnet equilibria in the FMASHZn system: geothermobarometry and applications. *Contributions to Mineralogy and Petrology* **111**, 362–377.

Nichols, G. T. (1995). The role of mylonites in the uplift of an oblique lower crustal section, East Antarctica. *Journal of Metamorphic Geology* **13**, 223–238.

Nichols, G. T. & Berry, R. F. (1991). A decompressional *P–T* path, Reinbolt Hills, East Antarctica. *Journal of Metamorphic Geology* **9**, 257–266.

Payne, J. L., Hand, M., Barovich, K. M. & Wade, B. P. (2008). Temporal constraints on the timing of high-grade metamorphism in the northern Gawler Craton: implications for assembly of the Australian Proterozoic. *Australian Journal of Earth Sciences* **55**, 623–640.

Phillips, G., Wilson, C. J. L., Campbell, I. H. & Allen, C. M. (2006). U–Th–Pb detrital zircon geochronology from the southern Prince Charles Mountains, East Antarctica—Defining the Archaean to Neoproterozoic Ruker Province. *Precambrian Research* **148**, 292–306.

Phillips, G., White, R. W. & Wilson, C. J. L. (2007*a*). On the roles of deformation and fluid during rejuvenation of a polymetamorphic terrane: inferences on the geodynamic evolution of the Ruker Province, East Antarctica. *Journal of Metamorphic Geology* **25**, 855–871.

Phillips, G., Wilson, C. J. L., Phillips, D. & Szczepanski, S. K. (2007*b*). Thermochronological (^{40}Ar/^{39}Ar) evidence of Early Palaeozoic basin inversion within the southern Prince Charles Mountains, East Antarctica: implications for East Gondwana. *Journal of the Geological Society, London* **164**, 771–784.

Phillips, G., Kelsey, D. E., Corvino, A. F. & Dutch, R. A. (2009). Continental reworking during overprinting orogenic events, southern Prince Charles Mountains, East Antarctica. *Journal of Petrology* **50**, 2017–2041.

Powell, R. & Downes, J. (1990). Garnet porphyroblast-bearing leucosomes in metapelites: mechanisms, phase diagrams, and an example from Broken Hill, Australia. In: Ashworth, J. R. & Brown, M. (eds) *High-temperature Metamorphism and Crustal Anatexis*. Springer Netherlands, pp. 105–123.

Powell, R. & Holland, T. (1988). An internally consistent thermodynamic dataset with uncertainties and correlations: 3. Application methods, worked examples and a computer program. *Journal of Metamorphic Geology* **6**, 173–204.

Rapp, R. & Watson, E. B. (1986). Monazite solubility and dissolution kinetics: implications for the thorium and light rare earth chemistry of felsic magmas. *Contributions to Mineralogy and Petrology* **94**, 304–316.

Rigby, M. J. & Droop, G. T. R. (2011). Fluid-absent melting versus CO_2 streaming during the formation of pelitic granulites: A review of insights from the cordierite fluid monitor. In: van Reenen, D. D., Kramers, J. D., McCourt, S. & Perchuck, L. L. (eds) *Origin and Evolution of Precambrian High-Grade Gneiss Terranes, with Special Emphasis on the Limpopo Complex of Southern Africa: Geological Society of America, Memoirs* **207**, 39–60.

Rosenberg, C. L. & Handy, M. R. (2005). Experimental deformation of partially melted granite revisited: implications for the continental crust. *Journal of Metamorphic Geology* **23**, 19–28.

Rubatto, D., Chakraborty, S. & Dasgupta, S. (2013). Timescales of crustal melting in the Higher Himalayan Crystallines (Sikkim, Eastern Himalaya) inferred from trace element-constrained monazite and zircon chronology. *Contributions to Mineralogy and Petrology* **165**, 349–372.

Sajeev, K., Williams, I. S. & Osanai, Y. (2010). Sensitive high-resolution ion microprobe U–Pb dating of prograde and retrograde ultrahigh-temperature metamorphism as exemplified by Sri Lankan granulites. *Geology* **38**, 971–974.

Sandiford, M. & Hand, M. (1998). Australian Proterozoic high-temperature, low-pressure metamorphism in the conductive limit. In: Treloar, P. J. & O'Brien, P. J. (eds) *What Drives Metamorphism and Metamorphic Reactions? Geological Society, London, Special Publications* **138**, 109–120.

Schmitz, M. D. & Bowring, S. A. (2003). Ultrahigh-temperature metamorphism in the lower crust during Neoarchean Ventersdorp rifting and magmatism, Kaapvaal Craton, southern Africa. *Geological Society of America Bulletin* **115**, 533–548.

Scrimgeour, I. & Hand, M. (1997). A metamorphic perspective on the Pan African overprint in the Amery area of MacRobertson Land, East Antarctica. *Antarctic Science* **9**, 313–335.

Shaw, R. K., Arima, M., Kagami, H., Fanning, C. M., Shiraishi, K. & Motoyoshi, Y. (1997). Proterozoic events in the Eastern Ghats Granulite Belt, India: Evidence from Rb–Sr, Sm–Nd systematics, and SHRIMP dating. *Journal of Geology* **105**, 645–656.

Simmat, R. & Raith, M. M. (2008). U–Th–Pb monazite geochronometry of the Eastern Ghats Belt, India: Timing and spatial disposition of poly-metamorphism. *Precambrian Research* **162**, 16–39.

Stacey, J. S. & Kramers, J. D. (1975). Approximation of terrestrial lead isotope evolution by a two-stage model. *Earth and Planetary Science Letters* **26**, 207–221.

Stepanov, A. S., Hermann, J., Rubatto, D. & Rapp, R. P. (2012). Experimental study of monazite/melt partitioning with implications for the REE, Th and U geochemistry of crustal rocks. *Chemical Geology* **300–301**, 200–220.

Stephenson, N. C. N. & Cook, N. (1997). Metamorphic evolution of calcsilicate granulites near Battye Glacier, northern Prince

Charles Mountains, East Antarctica. *Journal of Metamorphic Geology* **15**, 361–378.

Stüwe, K. (1995). Thermal buffering effects at the solidus. Implications for the equilibration of partially melted metamorphic rocks. *Tectonophysics* **248**, 39–51.

Stüwe, K. & Hand, M. (1992). Geology and structure of Depot Peak, MacRobertson Land. More evidence for the continuous extent of the 1000 Ma event of East Antarctica. *Australian Journal of Earth Sciences* **39**, 211–222.

Tajčmanová, L., Konopásek, J. & Košler, J. (2009). Distribution of zinc and its role in the stabilization of spinel in high-grade felsic rocks of the Moldanubian domain (Bohemian Massif). *European Journal of Mineralogy* **21**, 407–418.

Tenczer, V., Powell, R. & Stüwe, K. (2006). Evolution of H_2O content in a polymetamorphic terrane: the Plattengneiss Shear Zone (Koralpe, Austria). *Journal of Metamorphic Geology* **24**, 281–295.

Thompson, A. B. & Connolly, J. A. D. (1995). Melting of the continental crust: Some thermal and petrological constraints on anatexis in continental collision zones and other tectonic settings. *Journal of Geophysical Research: Solid Earth* **100**, 15565–15579.

Thost, D. E. & Hensen, B. J. (1992). Gneisses of the Porthos and Athos Ranges, northern Prince Charles Mountains, East Antarctica: Constraints on the prograde and retrograde *P–T* path. In: Yoshida, Y., Kaminuma, K. & Shiraishi, K. (eds) *Recent Progress in Antarctic Earth Science*. Terra Scientific Publishing, pp. 93–102.

Tingey, R. J. (1991). The regional geology of Archaean and Proterozoic rocks in Antarctica. In: Tingey, R. J. (ed.) *The Geology of Antarctica*. Clarendon Press.

Tirone, M., Ganguly, J., Dohmen, R., Langenhorst, F., Hervig, R. & Becker, H.-W. (2005). Rare earth diffusion kinetics in garnet: Experimental studies and applications. *Geochimica et Cosmochimica Acta* **69**, 2385–2398.

Tong, L. & Wilson, C. J. L. (2006). Tectonothermal evolution of the ultrahigh temperature metapelites in the Rauer Group, east Antarctica. *Precambrian Research* **149**, 1–20.

Vance, D., Müller, W. & Villa, I. M. (2003). Geochronology: linking the isotopic record with petrology and textures—an introduction. In: Vance, D., Müller, W. & Villa, I. M. (eds) *Geochronology: Linking the Isotopic Record with Petrology and Textures*. Geological Society, London, Special Publications **220**, 1–24.

Vernon, R. H. (1996). Problems with inferring *P–T–t* paths in low-*P* granulite facies rocks. *Journal of Metamorphic Geology* **14**, 143–153.

Vielzeuf, D., Clemens, J. D., Pin, C. & Moinet, E. (1990). Granites, granulites, and crustal differentiation. In: Vielzeuf, D. & Vidal, P. (eds) *Granulites and Crustal Evolution*. Springer Netherlands, pp. 59–85.

Walsh, A., Kelsey, D. E., Kirkland, C., Hand, M., Smithies, R. H., Clark, C. & Howard, H. (2015). *P–T–t* evolution of a large, long-lived, ultrahigh-temperature Grenvillian belt in central Australia. *Gondwana Research* **24**, 969–983.

Wang, Y., Liu, D., Chung, S.-L., Tong, L. & Ren, L. (2008). SHRIMP zircon age constraints from the Larsemann Hills region, Prydz Bay, for a late Mesoproterozoic to early Neoproterozoic tectono-thermal event in East Antarctica. *American Journal of Science* **308**, 573–617.

White, R. W. & Powell, R. (2002). Melt loss and the preservation of granulite facies mineral assemblages. *Journal of Metamorphic Geology* **20**, 621–632.

White, R. W. & Powell, R. (2011). On the interpretation of retrograde reaction textures in granulite facies rocks. *Journal of Metamorphic Geology* **29**, 131–149.

White, R. W., Powell, R., Holland, T. J. B. & Worley, B. A. (2000). The effect of TiO_2 and Fe_2O_3 on metapelitic assemblages at greenschist and amphibolite facies conditions: mineral equilibria calculations in the system $K_2O–FeO–MgO–Al_2O_3–SiO_2–H_2O–TiO_2–Fe_2O_3$. *Journal of Metamorphic Geology* **18**, 497–511.

White, R. W., Powell, R. & Clarke, G. L. (2002). The interpretation of reaction textures in Fe-rich metapelitic granulites of the Musgrave Block, central Australia: constraints from mineral equilibria calculations in the system $K_2O–FeO–MgO–Al_2O_3–SiO_2–H_2O–TiO_2–Fe_2O_3$. *Journal of Metamorphic Geology* **20**, 41–55.

White, R. W., Powell, R. & Holland, T. J. B. (2007). Progress relating to calculation of partial melting equilibria for metapelites. *Journal of Metamorphic Geology* **25**, 511–527.

Williams, M. L., Jercinovic, M. J., Harlov, D. E., Budzyn, B. & Hetherington, C. J. (2011). Resetting monazite ages during fluid-related alteration. *Chemical Geology* **283**, 218–225.

Wilson, C. J. L., Quinn, C. D., Tong, L. & Phillips, D. (2007). Early Palaeozoic intracratonic shears and post-tectonic cooling in the Rauer Group, Prydz Bay, East Antarctica constrained by $^{40}Ar/^{39}Ar$ thermochronology. *Antarctic Science* **19**, 339–353.

Yakymchuk, C. & Brown, M. (2014). Behaviour of zircon and monazite during crustal melting. *Journal of the Geological Society, London* **171**, 465–479.

Yakymchuk, C., Brown, M., Ivanic, T. J. & Korhonen, F. J. (2013). Leucosome distribution in migmatitic paragneisses and orthogneisses: A record of self-organized melt migration and entrapment in a heterogeneous partially-molten crust. *Tectonophysics* **603**, 136–154.

Yakymchuk, C., Brown, M., Clark, C., Korhonen, F. J., Piccoli, P. M., Siddoway, C. S., Taylor, R. J. M. & Vervoort, J. D. (2015). Decoding polyphase migmatites using geochronology and phase equilibria modelling. *Journal of Metamorphic Geology* **33**, 203–230.

Young, D. N., Zhao, J.-x., Ellis, D. J. & McCulloch, M. T. (1997). Geochemical and Sr–Nd isotopic mapping of source provinces for the Mawson charnockites, east Antarctica: implications for Proterozoic tectonics and Gondwana reconstruction. *Precambrian Research* **86**, 1–19.

Zhao, J.-x., Ellis, D. J., Kilpatrick, J. A. & McCulloch, M. T. (1997). Geochemical and Sr–Nd isotopic study of charnockites and related rocks in the northern Prince Charles Mountains, East Antarctica: implications for charnockite petrogenesis and Proterozoic crustal evolution. *Precambrian Research* **81**, 37–66.

Zhao, Y., Liu, X. H., Liu, X. C. & Song, B. (2003). Pan-African events in Prydz Bay, East Antarctica, and their implications for East Gondwana tectonics. In: Yoshida, M., Windley, B. F. & Dasgupta, S. (eds) *Proterozoic East Gondwana: Supercontinent Assembly and Breakup. Geological Society, London, Special Publications* **206**, 231–245.

Zhou, B. & Hensen, B. J. (1995). Inherited Sm/Nd isotope components preserved in monazite inclusions within garnets in leucogneiss from East Antarctica and implications for closure temperature studies. *Chemical Geology* **121**, 317–326.

Ziemann, M. A., Forster, H.-J., Harlov, D. E. & Frei, R. (2005). Origin of fluorapatite–monazite assemblages in a metamorphosed, sillimanite-bearing pegmatoid, Reinbolt Hills, East Antarctica. *European Journal of Mineralogy* **17**, 567–579.